# A Contribution to Characterizing and Calibrating the Pointing Control System of the SOFIA Telescope

A thesis accepted by the Faculty of Aerospace Engineering and Geodesy of the Universität Stuttgart in partial fulfillment of the requirements for the degree of Doctor of Engineering Sciences (Dr.-Ing.)

by

Franziska Harms

born in Stuttgart

Committee chair:        Prof. Dr. rer. nat. Hans-Peter Röser
Committee member:    Prof. Dr.-Ing. Jörg Wagner
Date of defence:         28.05.2009

Institute of Space Systems
Universität Stuttgart
2009

*For the astronomers of the SOFIA project…*

# Preface

Apart from the two space agencies DLR and NASA that made the development of the SOFIA project at all possible, this thesis could not have been written without the help and inspiration of many people.

# Table of contents

# Nomenclature

**Acronyms**

| | |
|---|---|
| ACCRF | Accelerometer Reference Frame |
| AOI | Area of Interest |
| ARW | Angular Random Walk |
| ABRF | Aircraft Bulkhead Reference Frame |
| ASRF | Aircraft System Reference Frame |
| ATCU | Attitude Control Unit |
| AV | Allan Variance |
| BF | Body Reference Frame |
| BS | Bulkhead Station |
| BL | Buttline |
| CCD | Charge-Coupled Device |
| CD | Coarse Drive |
| CDT | Central Daylight Time |
| CFRP | Carbon Fiber Re-enforced Plastic |
| DCC | Diagnostic and Configuration Computer |
| DCM | Direction Cosine Matrix |
| DEC | Declination |
| DLR | Deutsches Zentrum für Luft- und Raumfahrt |
| EGSE | Electronic Ground Support Equipment |
| EL | Elevation |
| ERF | Equatorial Reference Frame |
| FBC | Flexible Body Compensation |
| FCM | Focus and Centering Mechanism |
| FD | Fine Drive |
| FEM | Finite Element Method |
| FFT | Finite Fourier Transform |
| FFI | Fine Field Imager |
| FFIMFRF | Fine Field Imager Mounting Flange Reference Frame |
| FFIRF | Fine Field Imager Reference Frame |
| FOG | Fiber Optic Gyroscope |
| FPI | Focal Plane Imager |
| FPIMFRF | Focal Plane Imager Mounting Flange Reference Frame |
| FPIRF | Focal Plane Imager Reference Frame |
| FWHM | Full Width at Half Maximum |
| GYRF | Gyroscope Reference Frame |

| | |
|---|---|
| HIPO | High-Speed Imaging Photometer |
| HRF | Horizontal Reference Frame |
| ICRF | Inner Cradle Reference Frame |
| IMF | Instrument Mounting Flange |
| IQC | Image Quality Correction |
| IRAF | Image Reduction and Analysis Facility |
| IRAS | Infrared Astronomical Satellite |
| IRF | Inertial Reference Frame |
| ISO | Infrared Space Observatory |
| KAO | Kuiper Airborne Observatory |
| LST | Local Sidereal Time |
| LOS | Line-of-Sight |
| MTBS | Move-to-Boresight |
| NASA | National Aeronautics and Space Administration |
| OCRF | Outer Cradle Reference Frame |
| PSD | Power Spectral Density |
| PSF | Point Spread Function |
| Q | Quantization |
| RA | Right Ascension |
| RDA | Rotation Drive Assembly |
| RF | Reference Frame |
| RIA | Rotation Isolation Assembly |
| RIS | Rotation Isolation System |
| RMS | Root-Mean-Square |
| ROF | Rotation of Field |
| RP | Return Pump |
| RRW | Rate Random Walk |
| RSS | Root Sum Square |
| SF | Scale Factor |
| SI | Science Instrument |
| SIMFRF | Science Instrument Mounting Flange Reference Frame |
| SIRF | Science Instrument Reference Frame |
| SOFIA | Stratospheric Observatory for Infrared Astronomy |
| SMARF | Secondary Mirror Reference Frame |
| SMM | Secondary Mirror Mechanism |
| STA | Station |
| SUA | Suspension Assembly |
| TA | Telescope Assembly |
| TARF | Telescope Assembly Reference Frame |
| TASCU | Telescope Assembly Servo Control Unit |
| TC | Test Case |

| | |
|---|---|
| TCM | Tilt and Chopping Mechanism |
| TRC | Tracker Controller |
| UTC | Coordinated Universal Time |
| VIS | Vibration Isolation System |
| WFI | Wide Field Imager |
| WFIMFRF | Wide Field Imager Mounting Flange Reference Frame |
| WFIRF | Wide Field Imager Reference Frame |
| WL | Waterline |
| XEL | Cross-Elevation |

**Roman symbols**

| | |
|---|---|
| $a$ | Real inertial acceleration |
| $acc$ | Acceleration |
| $A$ | Area |
| $\mathbf{A}$ | Transformation matrix |
| $Alt$ | Altitude |
| $Az$ | Azimuth |
| $B$ | Bias instability coefficient, Background |
| $c_0$ | Vacuum velocity of light |
| $d$ | Angular distance |
| $drift$ | Centroid drift |
| $D$ | Diameter |
| $E_{,ph}$ | Photon Energy |
| $el$ | Elevation |
| $f$ | Frequency, focal length, specific force |
| $\mathbf{g}$ | Gravitational acceleration vector |
| $\mathbf{g_{1,2}}$ | Rotation axis vector |
| $h$ | Planck's constant, Heading |
| $I$ | Intensity |
| $j$ | rational number |
| $k$ | Cluster number |
| $K$ | Number of clusters, |
| | Rate random walk coefficient |
| | Autocorrelation function |
| $lat$ | Latitude |
| $L$ | Path length |
| $LST$ | Local sidereal time |
| $m$ | Number of samples per cluster |
| $M$ | Marginal distribution |

*Nomenclature*

| | |
|---|---|
| *n* | Number of samples |
| *N* | Coil turns, |
| | Angular Random Walk coefficient |
| *q* | Quantity of Interest |
| *r* | Radius |
| *R* | Misalignment angle, |
| | Rate ramp coefficient |
| *S* | Image scale, |
| | Power Spectral Density |
| $\mathbf{s_b}$ | Pointing vector at maneuver begin |
| $\mathbf{s_e}$ | Pointing vector at maneuver end |
| *SF* | Scale factor |
| *t* | Time |
| $t_s$ | Sample time |
| *T* | Temperature, |
| | Total test time |
| *u, v, w* | Cartesian coordinates of a vector |
| **u, v, w** | Rotation axis vectors |
| $v_t$ | Tangential velocity |
| *X* | Row pixel value |
| *Y* | Column pixel value |

**Greek symbols**

| | |
|---|---|
| $\alpha$ | Angle |
| $\beta$ | Angle |
| $\gamma$ | Angle |
| $\lambda$ | Wavelength |
| $\kappa$ | Parameter |
| $\theta$ | Angle |
| $\phi$ | Phase angle |
| $\varphi$ | Angle |
| $\pi$ | Pi (=3.141592..) |
| $\sigma$ | Standard deviation, root Allan Variance |
| $\tau$ | Time delay, cluster time, correlation lag |
| $\omega$ | Angular frequency |
| $\Omega$ | Rotation rate |
| $\Omega_i$ | Rotation rate at sample i |
| $\Omega_k$ | Averaged rotation rate at cluster k |

# Abstract

SOFIA, the Stratospheric Observatory for Infrared Astronomy, is an airborne observatory that will study the universe in the infrared spectrum. A Boeing 747-SP aircraft will carry a 2.5 m telescope designed to make sensitive infrared measurements of a wide range of astronomical objects. It will fly at and above 12 km, where the telescope collects radiation in the wavelength range from 0.3 micrometers to 1.6 millimeters of the electromagnetic spectrum. During flight, a door will be opened to allow clear optical observations from the cavity environment where the telescope is mounted.

The telescope pointing control is achieved during science observations by an array of sensors including three imagers, gyroscopes and accelerometers. In addition, throughout alignment and calibration of the telescope assembly, the High-speed Imaging Photometer for Occultation (HIPO) is used as a reference instrument. A theoretical concept has been developed to compensate the perturbations in the airborne environment and to correct them within the attitude control loop. A set of Cartesian reference frames is established to describe and manipulate the orientations of the various subsystems, sensor and pointing orientations.

The dissertation proposes the alignment strategy for these reference frames. By means of sky observations, reduced to make fundamental measurements of control performance, the calibration parameters for the transformation matrices between the reference frames are determined. The alignment maneuvers are described in order to measure the misalignment between the gyroscopes, the imagers and the focal plane. The alignment strategy incorporates the compensation concept for pointing errors due to static structural deformation and combines it with the alignment measurements.

To avoid a false calibration due to misinterpretation of the measured data, sensor errors and external perturbations that are present in the sensor signals are studied in detail. This refers mainly to the three gyroscopes which are the primary feedback sensors for the telescope pointing control loop. A set of data reduction techniques is presented that is used for the analysis of the sensor performance and alignment measurements. This includes the data reduction for the gyroscopes and for astrometric measurements with the imagers and HIPO.

An extensive test series of gyroscope measurements is presented. They characterize the sensor performance after the three gyroscopes are integrated into the telescope system. Various system effects caused by other TA subsystems, aircraft systems or ground support equipment are analyzed and typified.

During the first on sky tests of the SOFIA telescope in 2004, a variety of alignment measurements, structural flexure measurements and pointing measurements were performed. In particular, the gyroscope misalignment was measured and compensated. Measurements over the entire operational elevation range provide additional alignment and sensor performance information. The results are presented and discussed within this work.

Due to the fact that all of the optical components will be demounted for coating and cleaning from time to time, the alignment between the imagers and other sensors and the reference instrument is changing. Thus, a semi-autonomous method for the calibration is pursued and recommendations are established based on the proposed calibration concept and the measurement results.

# Zusammenfassung

SOFIA, das Stratosphären Observatorium für Infrarot Astronomie, ist ein Flugzeugobservatorium, mit dem das Weltall im Infrarot- und Submillimeter-Wellenlängenbereich erforscht werden soll. Ein Teleskopsystem ist in den hinteren Teil einer Boeing 747SP eingebaut, welches ausgelegt ist, um Messdaten mit einer besonders hohen räumlichen und spektralen Auflösung von einer Vielzahl von astronomischen Objekten aufzunehmen. SOFIA wird seine Messungen bei einer Flughöhe zwischen 12 und 14 km durchführen. Da man eine störungsfreie Beobachtung wünscht, ist oberhalb des Teleskopspiegels eine Öffnung in die Außenhaut des Flugzeugs geschnitten, deren Abdeckung bei Erreichen der Beobachtungsflughöhe aufgefahren wird. Das Teleskop ist nach dem Öffnen den Umgebungsbedingungen ausgesetzt: der relativ niedrigen Temperatur (ca. -60° C), dem niedrigen Druck (ca. 0.2 bar) und der mechanischen Belastung durch Wind und Strömungsturbulenzen, die durch die Außenhautöffnung des Flugzeuges bei Geschwindigkeiten von etwa 1000 km/h entstehen.
Die Ausrichtung des SOFIA Teleskops wird während der wissenschaftlichen Beobachtungen mit drei Kameras, drei Glasfaserkreiseln und sechs Beschleunigungsmessern überprüft und geregelt. Während der Teleskopcharakterisierung und -kalibrierung wird diese Überprüfung auch mit dem Referenzinstrument „High-speed Imaging Photometer for Occultations" (HIPO) durchgeführt, welches am Instrumentenflansch montiert ist und die Referenz an der Brennebene des Teleskops darstellt. Ein theoretisches Konzept wurde aufgestellt, um Strukturverformungen und Sensorfehler zu kompensieren und die daraus resultierenden Ausrichtungsfehler zu korrigieren. Das Konzept basiert auf einer Reihe von Koordinatensystemen, die die Lage und Orientierung des Teleskops und der einzelnen Sensorsysteme beschreiben. Die Ausrichtfehler werden ausgeglichen, indem entsprechende Korrekturmatrizen angewendet werden.

Die Dissertation befasst sich mit der Umsetzung dieses zunächst theoretischen Konzeptes in die Praxis. Es wurde eine Strategie entwickelt, um mit Hilfe von Sternbeobachtungen, welche mit den technischen Sensordaten korreliert werden, die Transformationsmatrizen zwischen den aufgestellten Koordinatensystemen zu bestimmen. Die Kalibrierung erfolgt schrittweise: Zuerst wird das virtuelle Teleskopkoordinatensystem anhand des Referenzinstruments HIPO an der Brennebene des Teleskops definiert. HIPO wurde so ausgelegt, dass die projizierte Mitte und die Orientierung des Instrumentenflansches auf den Instrumentendetektor genau vermessen werden können und somit bekannt sind. Dann werden die Kalibrierungsmessungen durchgeführt, welche die Beziehungen zwischen diesem mit HIPO definiertem Teleskopkoordinatensystem und den Sensorkoordinatensystemen bestimmen. Schließlich wird auch das Korrekturkonzept für Ausrichtfehler berücksichtigt, die aufgrund von Durchbiegungen der Teleskopstruktur auftreten. Die entwickelte Strategie kombiniert dieses mit den Kalibrierungsmessungen. Die genaue Kalibrierung dieser Sensorreferenzsystems ist für einen effizienten Beobachtungsbetrieb bedeutend, da die Sensoren die Ausrichtung und auch die Bewegungen des Teleskops identifizieren und über die Bewegungsregelung beeinflussen.

Die Sensorsignale, die ausgewertet werden, um die Kalibrierungsparameter zu bestimmen, sind mit Störungen behaftet. Um Fehlinterpretationen der Messdaten zu vermeiden wurden

die Sensorsignale detailliert untersucht. Dies betrifft insbesondere die drei Gyroskope, die die Hauptsensoren für die Lagerückführung im Regelkreis darstellen. Im Rahmen dieser Arbeit wurde eine Reihe von Gyroskop-Messungen durchgeführt, welche deren Eigenschaften beurteilen. Dies schließt auch den Einfluss von anderen Teleskopsubsystemen und den Flugzeugsystemen ein, die während der Messung aktiv waren. Die Rauschprozesse und Subsystemeinflüsse, die in den Gyroskopdaten vorhanden sind, wurden mittels Leistungsspektraldichte und der Allan Varianz analysiert und identifiziert. Die Ergebnisse wurden mit den theoretisch erwarteten Rauschcharakteristiken und mit den Kalibrierungsdaten des Herstellers verglichen. Die Ergebnisse zeigen, dass die in das Teleskopsystem integrierten Gyroskope die Spezifikation erfüllen. Die beiden Rauschprozesse, die für den Beobachtungsbetrieb ausschlaggebend sind, wurden quantitativ beurteilt: der *Angular Random Walk* und die *Bias-Stabilität*. Die äußeren Einflüsse auf die Sensorsignale wurden über mehrere Langzeittests beurteilt, indem das Teleskopsystem schrittweise aktiviert wurde. Es konnten eine Reihe von Frequenzen identifiziert werden, die von den Bodenanlagen und anderen Teleskopsystemen stammen. Die Auswirkung der Vibrationsisolierung auf die gemessenen Gyroskopsignale konnte zudem nachvollzogen werden.

Während der ersten Sternbeobachtungen mit dem Teleskop in 2004 wurde eine Vielzahl von Kalibrierungsmessungen durchgeführt, welche die Messung der Ausrichtungsfehler aufgrund von Einbauungenauigkeiten und Strukturdeformation einschließen. Die Resultate der Messungen werden in dieser Arbeit präsentiert und diskutiert. Die Messungen wurden mit einem unbeschichteten Primärspiegel durchgeführt, und somit konnten relativ helle Sterne, wie z.B. der Polarstern, mit langen Belichtungszeiten für die Kalibrierungsmessungen benutzt werden. Die Beobachtungsbedingungen hingegen waren mit der hohen Umgebungstemperatur und Luftfeuchtigkeit nicht optimal. Die in dieser Arbeit beschriebene Prozedur, um die Gyroskopachsen in Bezug auf die Teleskopbrennebene zu kalibrieren, wurde iterativ durchgeführt und Fehlausrichtungen wurden korrigiert.
Elevationsabhängige Messungen wurden durchgeführt, und Sterne wurden an verschiedenen Elevationen gleichzeitig in den Kameras und im Referenzinstrument HIPO beobachtet. Die differentiellen Bildbewegungen in den Kameras konnten so in Bezug auf die Brennebene des Teleskops bestimmt werden. Diese Messungen, die sich über den gesamten operationellen Elevationsbereich des Teleskops erstreckten, wurden auch für eine Überprüfung der absoluten Ausrichtgenauigkeit benutzt. Anhand katalogisierter Sternpositionen konnten Sternabstände theoretisch ermittelt werden. Diese Werte wurden dann mit den am Teleskop verfahrenen und durch die Gyroskope und Kameras gemessenen Winkeln verglichen unter Berücksichtigung von atmosphärischer Refraktion. Das Ergebnis zeigt, dass die Abweichung dieser Werte mit zunehmendem Sternenabstand linear ansteigt. Dies kann auf einen internen Gyroskop-kalibrierungsfehler hinweisen, dessen Ermittlung über den Rahmen der Arbeit hinausgeht..

Durch den regelmäßigen Ausbau der optischen Komponenten des Teleskops zu deren Reinigung und Beschichtung ändert sich die Ausrichtung zwischen dem Referenzinstrument an der Teleskopbrennebene und den Teleskopsensoren. Daher wird eine semi-autonome Methode für die Kalibrierungsmessungen angestrebt und Empfehlungen werden gegeben, die auf der vorgeschlagenen Kalibrierungsstrategie und den Messergebnissen basieren.
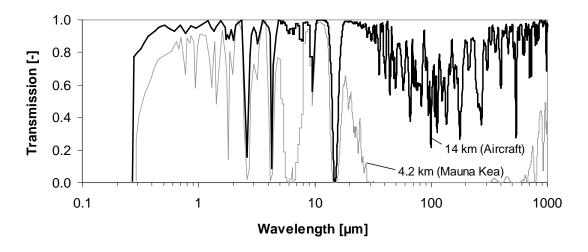
# 1   Introduction

Experimental research in astronomy is performed primarily by observing radiation from celestial objects of interest. The scientific objectives for these observations determine the type of observatory which is needed to carry out the desired investigations. An observatory includes typically the telescope system which collects the radiation and forms an image at the focal plane, and the instrument which analyzes and records the image. The two main classes of astronomical instrumentation are cameras which measure the shape and brightness of a source, and spectrometers which disperse the light of a source and measure its intensity as a function of wavelength.

The scientific objectives can be related to five basic requirement categories for an observatory [Bely 2003]:

- The **sensitivity** indicates the minimum brightness of the source that can be detected above the background noise. The sensitivity is related to the amount of collected radiation which is proportional to the surface area of the mirror. The larger the surface area to collect the light, the higher the sensitivity of the telescope. However, backgound noise limits the sensitivity significantly, and the observing location and environmental conditions play an important role for the observatory's sensitivity.
- The **angular resolution** describes the ability to distinguish between close objects, respectively between features of one object. The theoretical angular resolution is proportional to the mirror size and limited by diffraction. In practice, atmospheric fluctuations limit the anglar resolution of a telescope on ground and in the air. The resulting angular resolution of the telescope is hence seeing limited. The diffraction limit can only be achieved under very good observing conditions or by space telescopes.
- The **wavelength coverage** describes the wavelength region in which the source is observed.
- The **spectral resolution** describes the ability to distinguish between two wavelengths of the spectrum. This depends only on the type of science instrument used to generate the spectrum.
- The **temporal resolution** specifies the read-out rate of the recorded image data and depends only on the instrument detector and read-out software.

The spectral and temporal resolution solely depends on the design of the deployed instruments. Sensitivity, angular resolution and wavelength coverage depend on the design of the telescope and of the instruments, but are in practice limited by the environmental conditions of the observatory depending on whether it is ground based, airborne or space based. The sensitivity is lowered by atmospheric extinction, when observing through the atmosphere, and by any background noise between the detector and the source of interest which includes natural sources in the sky, atmospheric emission and thermal emission from the telescope itself. The angular resolution is lowered by atmospheric turbulence, by air density fluctuations above the mirror and telescope housing and by disturbances that cause vibrations on the optical elements of the telescope. The wavelength coverage is affected by the atmospheric extinction as only certain wavelength regions are transmitted through the atmosphere. Figure 1.1 compares the atmospheric transmission for a ground based observatory at Mauna Kea, Hawaii, and an airborne observatory at an altitude of 14 km. Particularly for observations in the far infrared (40 µm – 300 µm) and sub-millimeter region (300 µm – 1 mm), the water vapor of the Earth's atmosphere blocks radiation for ground observatories and the advantage of being at aircraft altitudes is evident.



**Figure 1.1.** Atmospheric transmission on Mauna Kea, Hawaii, and at an altitude of 14 km [Erickson 2005].

Full wavelength coverage and low background noise are reached with space based telescopes, but with higher cost and constraints regarding telescope size and lifetime. In addition, the design of the telescope and instruments is defined several years before launch and improvements due to new technology developments are not possible. Once the space based telescope is launched, repairs and instrument enhancements are difficult. Apart from the basic science requirements, the observatory location plays an important role when specific areas of the sky are aimed at. Short time events that occur sporadically at any place on the sky can only be observed with an mobile airborne observatory.

## 1.1 The Stratospheric Observatory for Infrared Astronomy (SOFIA)

Infrared and sub-millimeter astronomy enables astronomers to observe areas and objects in the sky which cannot be detected in the visible wavelength range. These are cold objects which radiate maximum energy in the infrared, and areas which are embedded in or covered by dense regions of gas and dust where visible light cannot pass through. Due to the expansion of the universe, distant objects emit light that is redshifted and can only be detected in the infrared. Additionally, numerous spectral features of solid particles and molecular, atomic and ionized gas are characterized at infrared and sub-millimeter wavelengths [Titz 1998]. Studying objects in the infrared which can be detected also in the visible wavelength range add information about the object. Figure 1.2 shows the horsehead nebula in the visible (400 nm – 700 nm), the near infrared (700 nm – 3 µm) and the mid-infrared (3 µm – 30 µm) and reveals the structural diversity of objects when observed at different wavelengths.



**Figure 1.2.** Visible (left), near infrared (center) and mid-infrared (right) observations of horsehead nebula, source: NASA/JPL-Caltech.

Infrared and sub-millimeter astronomy was successfully performed with ground based observatories such as the observatories of Mauna Kea in Hawaii, with space based observatories such as IRAS (Infrared Astronomical Satellite), ISO (Infrared Space Observatory), the Spitzer Space Observatory, and with the two predecessors of SOFIA, the airborne observatories Lear Jet and KAO (Kuiper Airborne Observatory). SOFIA will extend this scientific legacy. Scientific objectives include the study of interstellar medium, star formation, disk and planet formation, origin and evolution of biogenic material and gas and grain chemistry [Erickson 2005]. In addition, SOFIA will be a major factor in the development of observational techniques, of new instrumentations and in the education of young scientists and teachers in the discipline of infrared astronomy through extensive education and public outreach program.

### 1.1.1    The observatory

SOFIA, the Stratospheric Observatory for Infrared Astronomy, is an airborne observatory that will study the universe in the infrared spectrum. This joint US-German project is part of NASA's Origins Program. A Boeing 747-SP aircraft carries a 2.5 m telescope and flies at and above a height of 12 km where the telescope collects radiation in the wavelength range from 300 nm to 1.6 mm. During flight, a door will be opened to allow clear optical observations from the cavity environment where the telescope is mounted.

The telescope assembly has been integrated completely into the modified aircraft. In 2004, the first telescope integration and on sky performance tests took place on ground. The first test flight after the modification was successfully performed in 2007. The flight testing of the modified aircraft is ongoing and the first science flights are expected in 2009. Once full operation capability is reached, approximately 160 observing flights will be scheduled per year with more than 6 hours observing time per flight at an altitude above 12 km.

SOFIA's sensitivity and angular resolution are shown in Figure 1.3 and are compared to other infrared observatories [Erickson 2005]. The sensitivity is described as flux density as a function of wavelength in milliJanskys (1 Jansky = $10^{-26}$Wm$^{-2}$Hz$^{-1}$) for a signal-to-noise ratio of one in one hour integration time. For example, at a wavelength of 10 µm, SOFIA can detect a source with a flux density of 1 mJy with a signal-to-noise of one when integrating for one hour. The SOFIA telescope will operate at higher temperatures than space based telescopes leading to a higher thermal background and thus, a lower sensitivity. Due to SOFIA's larger mirror it is more sensitive than the KAO, which operated at same temperatures.
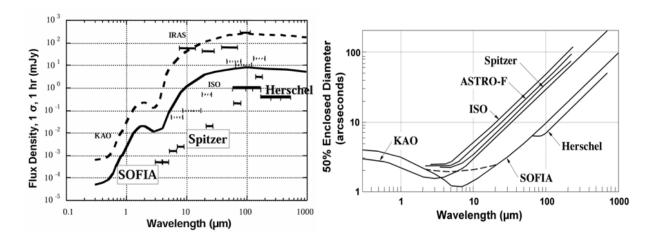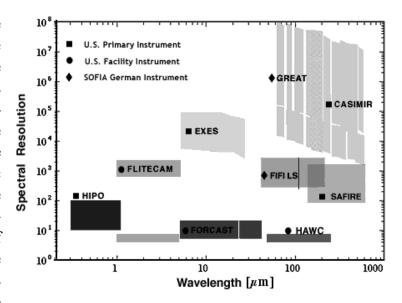


**Figure 1.3.**    Sensitivity (left) and angular resolution (right) of infrared telescopes [Erickson 2005].

The angular resolution is described as the angular diameter which encloses 50% of the energy of an imaged point source. The dashed line represents SOFIA's minimal requirements and the solid line is intended to be achieved. The angular resolution is diffraction limited for longer wavelengths (>30 µm) and seeing limited for shorter wavelengths. Here, seeing comprises the density fluctuations in the cavity, the shear layer turbulence and the vibrations of the optical elements [Dunham 2002].

To the present time, the science instruments developed for the SOFIA telescope include nine imagers and spectrographs [Casey 2004]. One science instrument is mounted on the telescope during each flight, except for one combination where two specific instruments are co-mounted. The spectral resolution of the instruments as a function of wavelength is shown in Figure 1.4. The resolving power is expressed as the ratio of two separable wavelengths apart and their mean wavelength ($\Delta\lambda/\lambda$).



**Figure 1.4.** Spectral resolution of SOFIA's first generation instruments [Becklin 2007]

### 1.1.2 The Telescope Assembly (TA)

**Telescope optics**

The SOFIA telescope is a Cassegrain telescope with a Nasmyth focus [Krabbe 2002]. The optics consists of a 2.7 m parabolic primary mirror (effective aperture: 2.5 m), a hyperbolic secondary (35 cm) and a flat dichroic tertiary mirror, which reflects the infrared light through the Nasmyth tube into the focus behind the Science Instrument (SI) flange. The visible light passes through the dichroic to an additional tertiary mirror which reflects the light into a guiding camera, the Focal Plane Imager (FPI). The optical path is illustrated in Figure 1.5.

The primary mirror is made out of a light weighted Zerodur structure with an almost zero thermal expansion coefficient, weighs about 880 kg and is aluminum coated. The secondary mirror is made from Silicon-Carbide, is aluminum coated and is actively driven along five degrees-of-freedom for alignment, focusing and chopping [Zago 1998]. The dichroic tertiary mirror is gold coated and the non-dichroic tertiary mirror is aluminum coated. To enable the SOFIA telescope to fit within the approximately 8 m diameter fuselage and keep it structurally stiff, the 2.7 m primary is highly curved at a f-number of 1.2 (ratio of focal length to aperture). When this is combined with the convex secondary, the system has an effective focal length of about 49 m, and thus a f-number of 19.8.

**Telescope structure**

The optical elements are carried by a metering structure which is made of Carbon Fiber Reenforced Plastic (CFRP). The metering structure is connected to one side of the CFRP Nasmyth tube by a stiff star frame interface. On the other side of the tube, the instrument flange is attached which provides the mounting for the science instruments and serves also as

the carrying structure for the FPI, the pressure window assembly and the balancing plate [Erhard 2000]. The telescope assembly – integrated into the aircraft bulkhead – is illustrated in Figure 1.6.
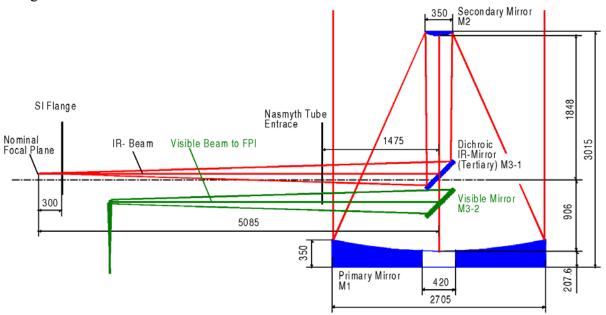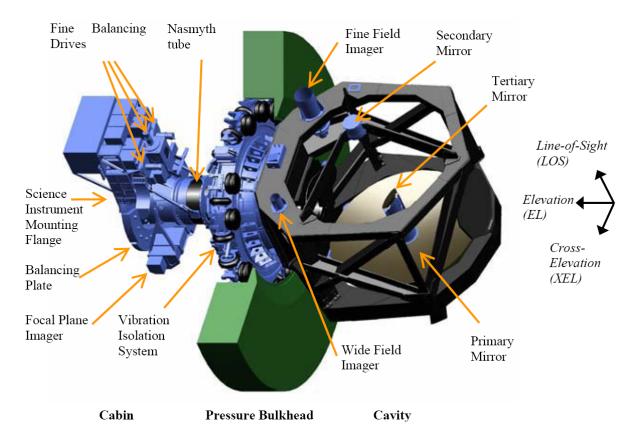


**Figure 1.5.**   Optical path of the SOFIA telescope [Krabbe 1999].



**Figure 1.6.**   3D drawing of the telescope assembly integrated into the aircraft bulkhead which separates the pressurized aircraft cabin and the open port telescope cavity, source: DLR.

The major visible TA components and the three main telescope rotation axes, Elevation (EL), cross-Elevation (XEL) and Line-Of-Sight (LOS) are indicated.

The pressure window assembly, consisting of a pressure plate and a gate valve within the instrument flange, maintains the pressure barrier within the Nasmyth tube between the pressurized aircraft cabin and the open port telescope cavity. The gate valve will be opened to enable science observations. The pressure barrier then lies either within the sealed science instrument or at an optical window mounted in front of the gate valve.

In order to keep the center of gravity of the TA in the center of rotation – the middle of a spherical bearing within the bulkhead - the coarse weights are mounted on the balancing plate counteracting the weight of the primary mirror and the metering structure. Different coarse weight configurations are possible depending on the weight of the science instrument. Four fine balancing drives are available, two for the EL-, one for XEL- and one for LOS-axis, which allow controlled and automated fine balancing.

**Telescope suspension**
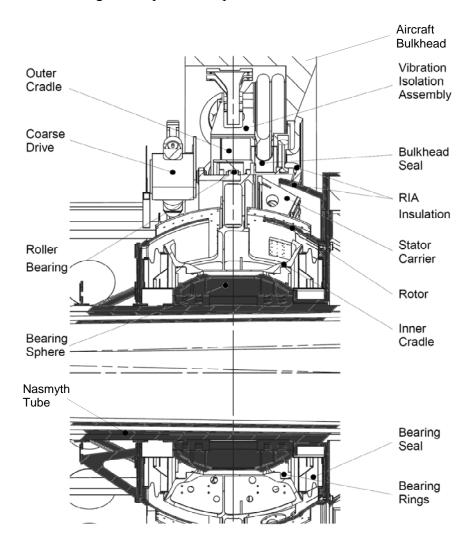
The telescope Suspension Assembly (SUA) fulfills following main requirements. It provides the connection between the TA and the aircraft, it acts as pressure and thermal boundary between cabin and cavity, and it isolates the TA from aircraft vibrations and positions the TA within the required pointing accuracy and stability [Weis 2000]. The cross section of the SUA is shown in Figure 1.7. The rotating parts of the telescope are shaded in grey.

The TA structure is supported on the aircraft bulkhead with the Vibration Isolation System (VIS) which is the only physical connection of the telescope with the aircraft. The VIS consists of 12 air springs in axial direction, 12 air springs in tangential direction and 3 viscous dampers. The air pressure in the springs is controlled to position the telescope within the bulkhead depending on the differential pressure between the cabin and the cavity [Sust 2002a]. To provide large angle, coarse elevation positioning of the telescope, a conventional one-axis roller bearing is located between the attachment brackets of the VIS, the so-called Outer Cradle, and the inner telescope structure, termed the Inner Cradle. During regular operations, the adjustable elevation angle of the Coarse Drive (CD) ranges from 16.5° to 68.5°. However, during maintenance operations this drive is capable of positioning the telescope through zenith to either horizontal orientation.

The main telescope structure with the Nasmyth tube, the metering structure and the instrument flange is supported within the SUA by a 1.2 m spherical hydrostatic oil bearing with brushless 3-axis spherical torque motors as drives. The low-friction bearing isolates the telescope rotationally from the aircraft. The torque motors, the Fine Drive (FD), handle fine positioning and stabilization of the TA in three degrees of freedom simultaneously. The rotation about the three axes is limited to about ±3 degrees per axis.

The inner cradle carries the stator part of the bearing: two bearing rings and the stator yokes of the torque motor consisting of 12 double-sided coil segments. The rotor part of the bearing is the bearing sphere which is attached to the Nasmyth tube. The rotor yokes of the torque drive are permanent magnets and are located in between the stator yokes. Torques are pro-

duced when current is channeled through the coil windings creating a magnetic field that interacts with the field from the permanent magnets. The commutation, which is the current control, is supported by three spherical sensors measuring the position of the coil windings relative to the permanent magnets. Furthermore, the spherical sensor measurements deliver the attitude of the rotating telescope with respect to the inner cradle.
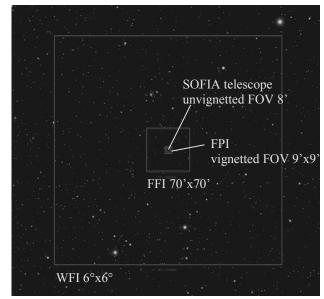


**Figure 1.7.** Cross section drawing of telescope suspension assembly [Weis 2000]. Rotating parts of the telescope are shaded in grey.

**Telescope pointing control sensors**

The pointing control of the telescope during science observations is achieved by an array of sensors. The telescope is stabilized inertially using three fiber-optic gyroscopes as feedback sensors within a closed attitude control loop. The gyroscopes are installed at the Nasmyth tube on the side of the pressurized cabin close to the bearing. Additionally, there are three accelerometers installed in the gyroscope box, as well as another set of three accelerometers on the flange assembly. These acceleration measurements are used to compensate for the pointing errors due to the flexibility of the telescope structure [Wandner 2000].

For long term positioning of the telescope on the sky, the pointing control system uses additional information from the FPI, which is mounted rigidly to the flange assembly [Bittner 2002]. The light beam coming from the visible light tertiary mirror is directed through folding mirrors and collimating optics and then imaged on a standard CCD detector. The FPI has an unvignetted field of view of 8 arcmin and is required to perform with stars as faint as a visible magnitude of 16 with maximum integration times of approximately 4 seconds. Centroid position information from the imaged stars is input into the attitude control loop to define a reference on the sky and to correct for pointing errors introduced by bias and random walk of the gyroscopes and other long term effects. Furthermore, two cameras are mounted on the head ring of the metering structure in the cavity. These include the Fine Field Imager (FFI) with a 70 arcmin field of view and the Wide Field Imager (WFI) with a 6 degree field of view. These cameras have separate optics and do not use the light beam coming through the main telescope optics. The three imagers as mounted on the TA are indicated in Figure 1.6. The FFI is used for precision tracking if no star is available in the FPI, and provides - along with the WFI - the knowledge of absolute pointing on the sky via star field identification. Their fields of view projected on the sky are shown



**Figure 1.8.** Unvignetted field of view of the SOFIA telescope and the fields of view of the three imagers projected on the sky close to the star constellation Lyra.

together with the unvignetted field of view of the SOFIA telescope in Figure 1.8.

## 1.2 Astronomical observations in an airborne environment

Taking full advantage of SOFIA's flexibility in scheduling astronomical observations requires complex observation planning. After selecting which astronomical objects will be observed, an observing plan is established depending on a) the objects' position on the sky, b) the exposure time, c) the instrument and its operation mode, and d) additional observing requirements, such as water vapor constraints and calibration requirements. A regular flight lasts about 8 hours and includes between 2 and 20 observation sources. A flight is split up into observation legs which is the time where the observation takes place and dead legs which allow the repositioning of the aircraft for the next object.

The number of observed objects and their observation time during a flight is optimized by flight planning. It considers astronomical requirements, the telescope motion range and air-

craft constraints [Frank 2003]. Astronomical requirements include the position of the object with regard to the Sun and the Moon, and the amount of water vapor in the line of sight to the object. Water vapor can be minimized by observing at higher elevation angles, higher altitudes and higher latitudes. The telescope motion range is limited between 16.5° and 68.5° in elevation and about ±3° in cross-elevation. However, the door drive system operates only in the elevation range between 20° and 60° and vignetting occurs, when observing outside this range. The elevation limit affects the visibility of an object from a certain aircraft location. The cross-elevation limit impacts the flight path because the aircraft has to turn constantly to maintain inertial telescope pointing. The aircraft constraints include takeoff and landing location, the fuel consumption, the possible altitude profile which is limited by the aircraft weight, wind models and restricted airspace.

Observing in an airborne environment makes not only observation planning difficult. The telescope itself is exposed to harsh perturbations while demanding requirements on the image quality and the telescope pointing must be fulfilled [Kärcher 2000a]. The incoming light propagates through a turbulent shear layer over the telescope cavity and through the inhomogeneous air density field inside the cavity limiting the image quality [Dunham 2002]. The optical elements of the telescope and its supporting structure are excited by the air fluctuations in the cavity and by the aircraft vibrations limiting the pointing stability. The science instruments and parts of the telescope are located inside the aircraft cabin, whereas the optical elements and their supporting structure are located in the open port cavity. Thus, pressure and temperature differences between the cavity and the cabin cause deformations of the telescope structure and disturb also the pointing.

## 1.3   Thesis objectives and outline

The dissertation is concerned with the telescope pointing control system of SOFIA and in particular with its pointing control sensors. These include the three imagers, the gyroscopes, the accelerometers and during alignment and calibration measurement also the reference instrument that is mounted on the focal plane. The interrelations between these sensors will be disturbed by deformations of the telescope structure, induced by gravity, pressure fluctuations, temperature differences, aircraft vibrations and aero-acoustic excitations. Already small deformation can cause pointing errors and lead to a misrepresentation of the telescope pointing on the sky.

The dissertation will contribute to an understanding of these effects. A theoretical concept has been developed to compensate the perturbations and to correct them within the attitude control loop. It is based on the introduction of a set of Cartesian reference frames. The thesis will develop the realization of this concept in practice. By means of sky observations, reduced to make fundamental measurements of control performance, correlated with engineering sensor data acquisition, the calibration parameters for the transformation matrices between the reference frames will be determined.

To avoid a false calibration due to misinterpretation of the measurement data, sensor errors and external perturbations present in the sensor signals need to be studied in detail. This refers mainly to the three gyroscopes which are the primary feedback sensors for the telescope pointing control loop.

Regular maintenance of components, including optics removal for coating, will cause loss of knowledge of the alignment relationships between the telescope attitude sensors and the controlled line of sight of the combined telescope and science instrument. Thus, a semi-autonomous method for the calibration is pursued and recommendations will be established based on the proposed calibration concept and the measurement results.

Briefly, the thesis objectives can be summarized with:

- Present and outline the theoretical concept of SOFIA's pointing control system.
- Develop a strategy and measurement techniques to calibrate the telescope reference frame relations.
- Characterize sensor, system effects and environmental influence on measurements and alignment maneuvers.
- Derive recommendations for automating the calibration measurement process and data reduction.

The dissertation contributes to an understanding of the relation between the telescope pointing at the focal plane and the telescope pointing identified by its sensors. The alignment of the science instrument optical axis and its detector orientation with respect to the telescope main optics and sensors is not covered within this work.

The characterization and alignment measurements are performed using the optical systems of the three imagers, the optical elements of the telescope and the reference instrument mounted on the instrument flange. The star images used for these measurements are detected in the visual wavelength range. In the following, the term "optical" is used in the context of technical systems where light interacts with matter, such as lenses and mirrors. The term "visual" relates to the wavelength range of light from 390 – 780 nm.

The alignment algorithms and methods within this work are intended for measurements in the visual wavelength range. As the wavelength is small in comparison to the size of the optical elements of the telescope, the imagers and the reference instrument, the propagation of the light waves can be treated with the techniques of Geometrical Optics. Hereby, the light waves can be idealized mathematically as rays for which exact geometrical laws are valid. The rays are the orthogonal trajectories of the wavefronts and their intensity profile is assumed to be flat. A more precise treatment of the propagation of light waves is that of Physical Optics where the dominant property of light is its wave nature [Hecht 2002]. Geometrical Optics is the conceptual limit of Physical Optics for wavelengths $\lambda \rightarrow 0$. Physical Optics account for effects such as diffraction and interference. As mentioned in section 1.1.1, the SOFIA telescope is diffraction limited for longer wavelengths ($\lambda > 30\ \mu m$). In the case of diffraction-

limited optics, the light waves near the focus have a beam waist due to the diffraction effects. Then, the propagation of light can be treated with Gaussian Beam Optics. This work is concerned with basic diffraction effects only in regard to image formation of a point source for understanding image stability requirements and centroid algorithms. Otherwise, the propagation of light is treated with Geometrical Optics.

The objectives of the dissertation are structured in the following way:

As presented, the first chapter introduces the SOFIA project, describes the set up of the telescope assembly in detail and outlines the challenges when observing with a telescope in an airborne environment. The scope of the thesis is put into context.

Chapter 2 discusses the telescope pointing control system. The basic pointing terminology and the pointing control system's tasks and requirements for SOFIA are described. The architecture of the pointing control system is discussed - in particular how disturbances are compensated. Therefore, a reference frame concept is introduced and the sensors that identify the pointing are described in detail. The thesis work gives emphasis on the fiber optic gyroscopes which are the sensors that build the core inertial reference for the telescope pointing control.

Chapter 3 outlines the alignment strategy for the telescope internal reference frames that are based on measurements with the pointing control sensors and a reference instrument at the focal plane. The algorithms are derived which determine the matrices compensating for the measured misalignments. The implementation of the alignment matrices that are provided within the pointing control system are described. A combination of the flexure compensation with the alignment measurements is proposed. The chapter concludes with accuracy estimation of the alignment measurements.

Chapter 4 describes the various data reduction techniques for analyzing the inertial sensor signals. The techniques of analyzing gyroscope rate signals and their random noise are emphasized. Furthermore, the data reduction techniques include the centroiding algorithms for the image analysis, as well as atmospheric effects that have to be considered when comparing measurements over the entire elevation range.

In chapter 5, the performance of the gyroscopes is characterized by means of measurement data. The presented data reduction techniques are applied. Calibration data from the manufacturer before TA system integration are discussed as well as the measurement data after TA system integration. The results characterize the noise processes present in the gyroscope data along with various system effects caused by other TA subsystems, aircraft systems or ground support equipment.

In chapter 6, the analysis results of several calibration measurements are presented that were performed during the first on sky observations in 2004. The results include alignment maneuvers, flexure measurements and pointing measurements. Together with the acquired knowledge of sensor and system performance in chapter 5, recommendations are established in regard to automate these measurements.

Chapter 7 concludes with a summary of the thesis.

# 2    The pointing control system

This chapter introduces SOFIA's pointing control system and builds the foundation for the present work. The goal of the pointing control is to provide high precision inertial pointing for the science instruments mounted on the telescope. Pointing errors due to telescope structural deformations and sensor errors are to be compensated and are ideally not noticeable for the observer at the science instrument detector. The first part explains the pointing terminology and definitions and describes the requirements and the pointing budget. The second part presents the pointing control architecture and describes the various compensation methods for the expected pointing errors. The pointing control sensors are described in detail with a special emphasis on the gyroscopes due to the fact that they are the main feedback sensors in the control loop.

## 2.1   Definitions and pointing terminology

The terminology within SOFIA's pointing control is defined as follows, after [NASA SPO 2000].

**Telescope pointing** is defined as the act of causing the telescope assembly to be aimed or directed in a particular direction effecting the telescope optics to gather light within its field of view in that direction as observed at the TA focal plane.

**Blind pointing** is defined as the automated process of initially aiming the telescope closely to the target of interest prior to target identification and acquisition by commanding celestial coordinates given in right ascension and declination. Blind pointing is performed without the means of optical devices. The relation between the celestial coordinates and the instantaneous telescope attitude is estimated using the aircraft position and attitude and the telescope orientation with respect to the aircraft bulkhead.

The **Boresight location** refers to the intersection of a system's optical axis with its focal plane. For SOFIA, there are three different types of boresights:

- The **TA boresight** corresponds to the intersection of the main TA optical axis with the TA focal plane.
- The **SI boresight** corresponds to the intersection of the SI optical axis with the SI focal plane.

- The **imager boresight** corresponds to the imager optical axis with the imager focal plane. Within the pointing control system of SOFIA, the TA boresight is defined at the focal plane and expressed with respect to the imager reference frames. The SI boresight is expressed with respect to the main telescope reference frame.

**Tracking** is defined as the automated feedback controlled process by which the telescope is pointed at a location in the sky by the tracker to a celestial body. Tracking commences the moment the tracker error signals are used to close the TA tracking feedback loop. The tracker sensor is always one of the three TA imagers and error signals are generated only two-dimensional.

- **On-axis tracking** is that tracking mode where the designated TA imager and the experimenter's detector both derive information from the same celestial source. The line-of-sight to the source can be - but is not necessarily - controlled to be in alignment with the telescope main optical axis. Figure 2.1 (upper row) illustrates on-axis tracking. The science object is shown as imaged at the focal plane on the left side and in the imager FOV on the right side. The science object is located at the TA boresight. During tracking, the tracking star is held on the designated tracking position in the imager FOV.

- **Offset tracking** is that tracking mode where the tracker sensor and the experimenter's detector derive information from separate sources. In this mode, suitable bias coordinates are impressed on the tracked target(s) to position another object (the desired science object) on the TA boresight. Figure 2.1 (lower row) illustrates off-axis tracking. The science object is located at the SI reference, but might not be visible in the imager. Therefore, another source is used for offset tracking to keep the location of the science object at its position. During tracking, the tracking star is held on the designated tracking position in the imager FOV.
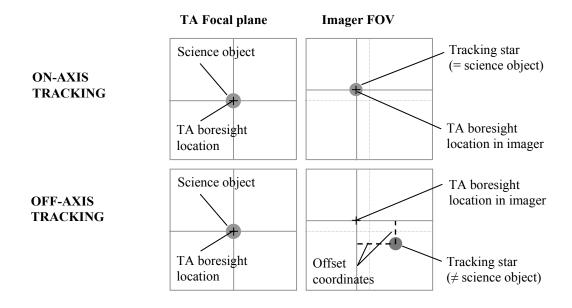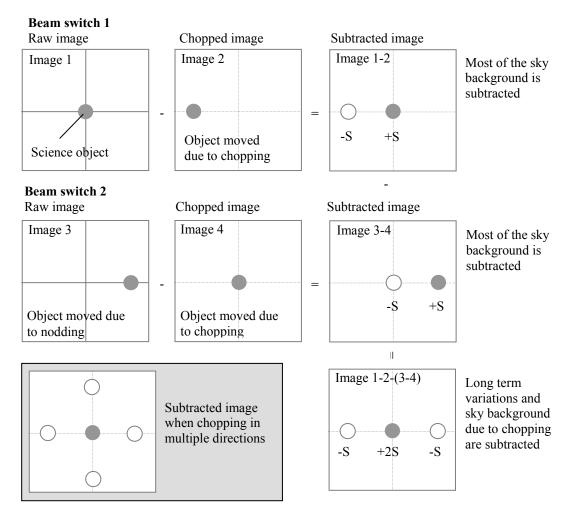


**Figure 2.1.** Definition of on-axis and off-axis tracking.

Apart from pointing the telescope in an absolute orientation to the sky, relative to the previous orientation and in predefined paths, infrared observations require special command patterns. If faint infrared sources are observed, background noise must be subtracted in order to extract the faint signal. The background noise is in general referred to the sky background and includes the detector noise, the thermal background of the telescope, stray light and the atmospheric background. There are different techniques to subtract the sky background depending on the observed wavelength range. For observations in the near infrared, the object can be placed at different positions on the detector by the telescope (dithering) and the field around the source can be used to subtract the sky background. For longer wavelengths, the background fluctuates with a smaller time scale. Then, the object and empty sky is placed on the detector repeatably and quickly by the secondary mirror (chopping). To eliminate asymmetrical effects, the sky background can be subtracted by chopping in multiple directions from the source, see the grey box in Figure 2.2 for an example: The telescope is moved between two beams during chopping to eliminate residual background variations introduced by chopping on a longer time scale (nodding) [Bely 2003].



**Figure 2.2.** Typical observation scheme for observing in the mid infared to sub-millimeter wavelength range.

Figure 2.2 shows furthermore a typical observation scheme for the mid infrared to sub-millimeter wavelength range with chopping and nodding motions. A science object is place on the imaging array (image 1) and the object is moved by a secondary mirror motion (image 2). The chopped image 2 is subtracted from the raw image 1. Usually, the chopping is performed usually at frequencies between 3-7 Hz yielding images where most of the sky background is removed. Then, the telescope is moved to a different position and chopping is performed again. Switching between these two positions is performed at a slower time scale and removes long-term variations and residual background introduced by chopping from the data. Subtracting the image data from nod position 1 and 2 yields an image that has a positive signal of the source with twice the intensity than the negative signal at the chopped positions (shown in the lower right corner).

## 2.2 Requirements

The operational requirements for the pointing control system are expressed in terms of pointing accuracy and pointing stability. After manufacturing the telescope system, the decision was made to combine the pointing stability requirement with the image quality requirements to an overall image size requirement.

**Pointing accuracy** is defined as the fidelity with which the pointing control system after acquiring a suitable target (or set of targets), initially positions the science object relative to the TA boresight at the onset of observation.

As illustrated in Figure 2.3, pointing accuracy (under both on-axis tracking and offset tracking) will be quantified by establishing the average value of the set of measured angular displacements between the TA boresight location and 10 "instantaneous" science object location samples taken immediately following a 5-second settling time upon initiation of track.



**Pointing stability**
Radial RMS value of image deviation from centroid of over a period from 5 ms to an hour

**Initial object location**
Average of initial 10 science object locations

**Pointing accuracy**
Angular displacement of initial object location to the TA boresight location

TA boresight location
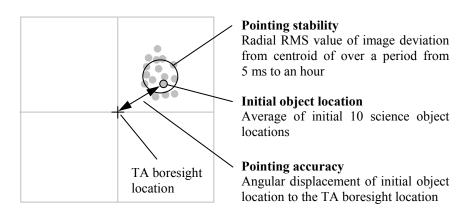
**Figure 2.3.** Definition of pointing accuracy and pointing stability, after [NASA SPO 2000].

**Pointing stability** is defined as the measure of relative motion of a science object of interest in the TA focal plane, over the observation period of time during which TA attitude is controlled. Specifically, under both on-axis and offset tracking operations, it is defined as the image deviation from the centroid of the image imprint in the focal plane, measured as the RMS value of the deviation over any period from 5 milliseconds up to an hour of continuous pointing at the same object. This is also illustrated in Figure 2.3.

The **Image quality** requirement is expressed in terms of the diameter of a circle enclosing 80% of the energy from a stellar image at a wavelength of 0.633 μm at the infrared focus.
Both, the pointing stability and image quality contribute to the size of an image. The various error sources and limitations that influence the pointing accuracy and image size are listed in Table 2.1. These errors and limitations for the SOFIA telescope are broken down in detail in the image quality budget [Erdmann 2002] and the pointing stability budget [Kaercher 2000b]. The pointing stability budget is further broken down into contributions caused by the aircraft environment and contributions within the servo subsystem. The pointing stability budget is shown in Appendix A.

**Table 2.1.**    Error sources and limitations affecting the image size under tracking

| Pointing accuracy | Image size | |
|---|---|---|
| | Pointing stability | Image quality |
| Misalignment of focal plane and imagers<br>- due to mounting inaccuracies, including non-orthogonality<br>- due to gravity<br>- due to slow temperature and pressure variations in flight<br><br>Scale factor error of gyros<br><br>Centroid errors | Vibrations of telescope structure (under 70 Hz)<br>- induced by aircraft vibrations<br>- induced by aero-acoustic vibrations<br><br>Random drift of gyroscopes and its estimation process<br><br>Centroid errors and contributions from tracking subsystem | Diffraction<br><br>Imperfections of manufactured optical elements<br><br>Optical aberrations<br>- due to gravity<br>- due to slow temperature and pressure variations in flight<br><br>Shear layer seeing, atmospheric seeing (for ground observations)<br><br>Vibrations of telescope structure (above 70 Hz) |

The size of an image is characterized by its point spread function (PSF). The PSF is the distribution of light intensity in the image of a point source and is wavelength dependent. For a perfect telescope with a circular aperture, the PSF is described with an Airy function [Hecht 2002]. The PSF can be approximated by a two-dimensional Gaussian intensity distribution with a mean value at zero and the standard deviation $\sigma$ for both independent variables.

Assuming the Gaussian distribution, the relation between the pointing stability requirement which is expressed as the radial RMS value of the centroid motion $r_{RMS}$ and the image quality requirement which is expressed as the diameter $D(80\%)$ that encloses 80% of the energy in the image can be described with [Erickson 2000]:

Diameter of 80% encircled energy:   $D(80\%) = 2.54 r_{RMS}$ (2.1)

The angular resolution of the SOFIA telescope (Figure 1.3) is described with the diameter $D(50\%)$ that encloses 50% of the energy in the image. For a Gaussian distribution it is roughly equal to the Full Width at Half Maximum (FWHM) [Erickson 2000] and is given by:

Diameter of 50% encircled energy:   $D(50\%) \approx FWHM = 1.67 r_{RMS}$ (2.2)

The standard deviation of the Gaussian distribution is related to the radial RMS by $r_{RMS} = \sigma\sqrt{2}$. Figure 2.4 shows the Gaussian PSF for $\sigma = 1$ for both independent variables and the three described definitions of image size.
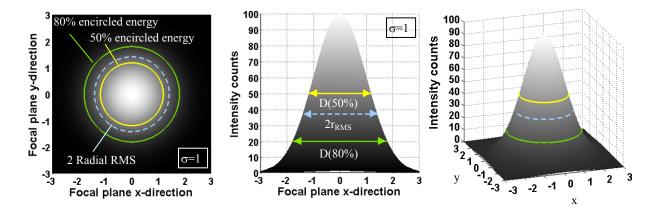


**Figure 2.4.**   Definitions of image size requirements.

The operational requirement values for pointing accuracy, pointing stability and image quality are listed in Table 2.2. The requirement values for the image quality and pointing stability expressed are combined to the image size requirement as root sum square.

**Table 2.2.**   Key operational requirements for the pointing control system [NASA SPO 2000].

| **Pointing accuracy** | On-axis tracking with | |
|---|---|---|
| | WFI | 6 arcsec for visible source brighter than $m_v$=13 |
| | FFI | 3 arcsec for visible source brighter than $m_v$=13 |
| | FPI | 0.5 arcsec for visible source brighter than $m_v$=16 |
| | Offset tracking with all imagers | On axis tracking value plus 0.06 arcsec per 1 arcmin offset |

| **Pointing stability** | On-axis tracking for a period of one hour with | |
|---|---|---|
| | WFI | 3 arcsec for visible source brighter than $m_v$=13 |
| | FFI | 0.8 arcsec for visible source brighter than $m_v$=13 |
| | FPI | 0.2 arcsec for visible sources brighter than $m_v$=16 |
| | Offset tracking with all imagers | On axis tracking value plus 0.06 arcsec per 1 arcmin offset |
| **Image quality** | 1.5 arcsec diameter of circle enclosing 80% energy at a wavelength of 0.663 μm | |
| **Image size** | Diameter of circle enclosing 80% energy at a wavelength of 0.663 μm | |
| (Combined requirement of pointing stability and image size) | Initial operations | *5.3 arcsec* |
| | First science plus 3 years | 1.5 arcsec |

## 2.3  Pointing control architecture

A theoretical concept has been developed to compensate for the perturbations in the airborne environment (section 1.2), and to correct them within the attitude control loop [Wandner 2000]: A set of Cartesian reference frames is established to describe and manipulate the orientations of the various subsystem, sensor and pointing orientations. The principal idea of the concept is to develop a control system embedded to the telescope that will provide external users and other systems with a simplified command and data interface to command, relative to an inertial frame, the orientation of the telescope boresight (referenced to the center of the focal plane where the science instruments are mounted). A virtual TA Reference Frame (TARF) is introduced reflecting the telescope pointing as seen at the focal plane. It is described with respect to inertial space and is fixed to the telescope. A number of corrections and calibrations, internal to the telescope control are implemented such that to external systems the telescope behavior may be assumed to be perfectly aligned and rigid. TARF is composed of three axes: the elevation axis (EL) u, defined as the symmetric axis along the Nasmyth tube, the cross-elevation axis (XEL) v, perpendicular to the u- and w-axis, and the line-of-sight axis (LOS) w, perpendicular to the primary mirror. TARF's origin can be shifted to any point on the TA, as small translations do not play a role for astronomical observations.

In the case of inertial stabilization, an Inertially fixed Reference Frame (IRF) is defined during start up to be identical to the initial orientation of TARF (Figure 2.5). To external systems the telescope is controlled by orienting TARF with respect to IRF.

To establish IRF and propagate TARF, a set of three precision fiber optic gyroscopes are used providing angular rate information as feedback sensors. The sensing axes of these gyroscopes, after alignment correction, build up the Gyroscope Reference Frame (GYRF). However, due to flexures, GYRF does not maintain a fixed relative orientation with respect to TARF as a function of elevation and under various accelerations. To account for this, the relationship

between TARF and GYRF is dynamically calculated to create and continually correct IRF. Through the relation TARF with respect to IRF, the inertial stabilization is maintained and the commanded and fed back attitude is described within the attitude control loop.
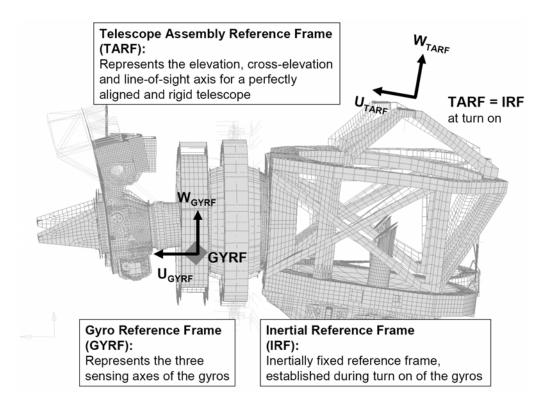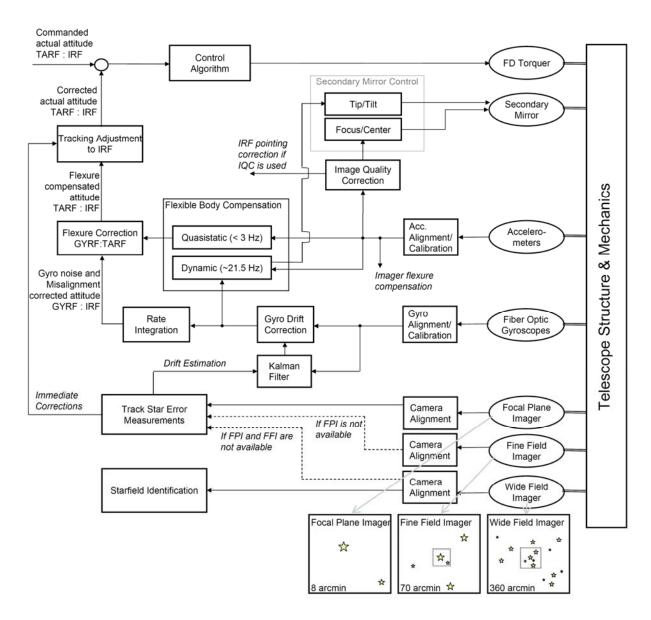


**Figure 2.5.** Basic telescope reference frames used for pointing control, FEM image: U. Lampater.

At the beginning of each mission or flight, a set of astrometric stars are used to identify how IRF is oriented with respect to the sky and the scientists are provided with the information where the telescope is pointing in an absolute sense. Pointing errors due to flexure, vibrations and sensor errors are compensated internally within the control loop.

A schematic representation of the attitude control loop in inertial stabilization is shown in Figure 2.6. The basic telescope servo control loop uses the gyroscopes as sensors and the FD torquers as actuators.

The required pointing corrections for compensating the flexures of the structure are estimated with the measurements of the gyroscopes and accelerometers. The so called Flexible Body Compensation (FBC) is split into two parts: The quasi-static part concerning gravity correction and frequencies below 3 Hz is handled by the FD. The dynamic portion compensates higher frequency errors, including the first resonance mode which lies at about 21.5 Hz. Such errors are beyond the bandwidth of the FD and are corrected with the active secondary mirror.

**Figure 2.6.**    Schematic representation of pointing control loop in inertial stabilization mode.

Furthermore, GYRF has to be adjusted due to the sensor errors of the gyroscopes. Although the fiber optic gyroscopes have very low noise and a high performance, the integrated rate noise will result in pointing errors i.e. a drift of IRF on the sky. A tracking loop is available evaluating star centroids in the FPI and providing the servo control loop with pointing corrections with integration times from 0.1 to approximately 4 seconds. The pointing correction can be performed either immediately correcting IRF itself, or feeding the FPI information into a Kalman filter estimating the drift corrected gyroscope rates in advance.

At varying elevations, telescope flexures move the optics slightly out of collimation from the nominal alignment. The effect is small and it is intended to adjust the secondary mirror in tilt and translation to provide Image Quality Correction (IQC) adjustments if needed. If IQC adjustments are applied, they will be performed by actuating the focus and centering mechanism of the secondary mirror. Such motions results in a pointing change and will be corrected by

changing the IRF appropriately. Tip, tilt and centering motions of the secondary mirror yield pointing changes at the focal plane but not in the two head ring imagers (FFI and WFI). Hence, the relation between the imager reference frames and TARF are also updated accordingly.

## 2.4 Sensor description

### 2.4.1 Fiber Optic Gyroscopes (FOG)

The FOGs measure rotation rates with respect to inertial space. The fundamental principle is based on the Sagnac effect, which produces a phase difference proportional to the rotation rate of an optical circular ring interferometer (Figure 2.7). The light from a single optical source is divided by a beam splitter into two waves traveling around a closed optical fiber coil in opposite directions. For a system at rest, both waves have to travel the same path length and return in phase, see Figure 2.7 (a) [Lefevre 1993]. When the system is rotating with an angular velocity $\Omega$ about an axis orthogonal to the plane containing the light path $L$, the beam splitter through which the waves are entering and exiting the coil has moved. E.g., the wave traveling clockwise has now a longer path from entry to exit and the wave traveling counterclockwise has a shorter path see Figure 2.7 (b) and (c). Hence, an observer at rest in the inertial frame notices a path length difference $\Delta L$ between the two waves, center and right side.
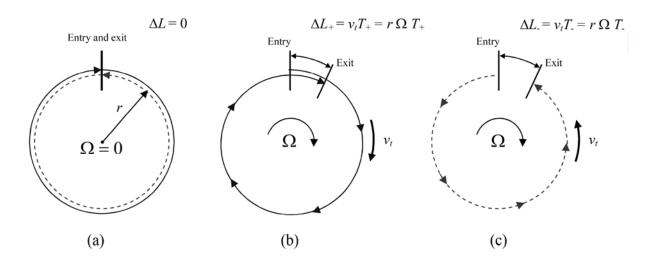


**Figure 2.7.**   Principle of the Sagnac Effect in a ring interferometer.
  (a) The system is at rest and the two counter-propagating waves have the same path length $L$.
  (b) The system is rotating. The wave in direction of rotation has a $\Delta L_+$ longer path that at rest.
  (c) The system is rotating. The counter-propagating wave has a $\Delta L_-$ shorter path that at rest.

In a simplified model, the ring is perfectly circular, the rotation takes places perpendicular to the plane of the light path and the velocity of light is the vacuum velocity of light $c_0$. For a rotating system, the path length $L_+$ for the beam in direction of rotation increases to:

$$L_+ = L + \Delta L_+ = L + v_t T_+ = \frac{L}{1 - \frac{v_t}{c_0}}$$

(2.3)

Here, $v_t = r\,\Omega$ is the tangential velocity of the ring with radius $r$ and $T_+ = L_+/c_0$ is the traveling time of the wave for one circle. On the other hand, the path length $L_-$ of the counter-propagating wave decreases to:

$$L_- = L - \Delta L_- = L - v_t T_- = \frac{L}{1 + \frac{v_t}{c_0}}$$

(2.4)

Assuming that the tangential velocity $v_t$ is small compared to the velocity of light ($v_t/c_0 \ll 1$), the overall path length difference $\Delta L$ becomes:

$$\Delta L = L_+ - L_- = \frac{2Lv_t}{c_0}$$

(2.5)

Which yields to the well know proportional relation between the path length difference, the area $A$ enclosed by the optical path and the angular velocity $\Omega$ with which the ring is rotated:

$$\Delta L = \frac{4A}{c_0}\Omega$$

(2.6)

Actually, the Sagnac effect is a purely relativistic effect. Nevertheless, the simplified model delivers correct results assuming that the signal velocity is identical to the velocity of light. The complete derivation is given in [Rodloff 1999]. It is shown, that the path length difference between the counter-propagating waves does not depend on the signal velocity and hence the refractive index of the medium. It does not depend either on translational velocities or the position of the observer which makes the Sagnac effect so important for inertial navigation.

Measured in an interferometer, the path length difference $\Delta L$ yields the phase difference $\Delta\phi$:

$$\Delta\phi = \omega\frac{\Delta L}{c_0} = \frac{2\pi DL}{\lambda c_0}\Omega$$

(2.7)

where $\omega$ is the angular frequency, $\lambda$ is the optical wavelength, $D$ is the diameter of the fiber coil, $L = N\pi D$ is now the length of the fiber coiled over $N$ turns.

The interference pattern leads depending on the phase difference to a co-sinusoidal response function of the FOG with intensity *I*:

$$I = I_0\left(1 + \cos\Delta\phi\right) \tag{2.8}$$

Thus, the unambiguous range of phase measurement is $\Delta\phi = \pm\pi$ which corresponds to an unambiguous dynamic operating range of $\pm\Omega_{max}$ for the rotation rate with:

$$\Omega_{max} = \frac{\lambda c_0}{2DL} \tag{2.9}$$

Assuming that a phase difference of a micro-radian is a good order of magnitude of sensitivity, the minimal rate $\Omega_{min}$ being detected can be estimated to [Lefevre 1993]:

$$\Omega_{min} = \frac{\lambda c_0}{2\pi\ DL}\ 10^{-6} \tag{2.10}$$

The co-sinusoidal response function, equation (2.8), has a gradient of zero at the zero point leading to a low sensitivity at small rotation rates. To enhance sensitivity a phase bias can be introduced between the two waves by incorporating a phase modulator. The ideal phase bias of $\pi/2$ produces a sinusoidal response function which has its greatest sensitivity at small rotation rates. In practice, the bias phase is chosen between $\pi/2$ and $3\pi/4$ for a better signal-to-noise ratio.
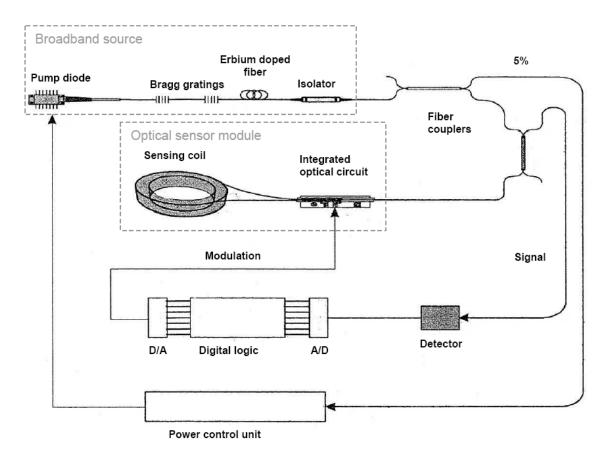
**SOFIA FOG design**
The three gyroscopes used within the SOFIA pointing control system are interferometric FOGs produced by the company IXSEA (former Photonetics) [Moik 2000, Wandner 1999]. For optimal operation conditions the so called FOG180 gyroscopes are operated in closed loop. Using the rotation induced phase differences $\Delta\phi$ as an error signal, an additional phase difference is generated by a phase modulator that adjusts the measured phase difference to zero. The value of the additional feedback is used as a measurement of angular rate. It has a linear response with good stability and the system can be operated about the point of greatest sensitivity [Titterton 2004].
The FOG180 (Figure 2.8) consists of an optical sensor module and an opto-electronic module. The optical sensor module comprises the quadrupolar fiber optic coil with temperature sensors and a multi-function integrated optical circuit, which includes the polarizer for single-spatial-mode filtering and polarization filtering, the beam splitter (Y junction) and the phase modulators for phase biasing and closed loop operation.
The opto-electronic module consists of the broadband source (for power and wavelength stabilization, this includes a pump diode, Bragg gratings, an Erbium doped fiber and an isolator), the 3dB fiber couplers, the detector, the all-digital closed loop signal processing unit and the closed loop power control unit.

A detailed description of such an optimum configuration FOG can be found in [Lefevre 1993] and of the broadband source in [Seidel 2004].



**Figure 2.8.** Block diagram of the FOG180 architecture [Wandner 1999]

One advantage of the FOG is that its sensitivity can be adjusted by changing the coil geometry without a complete redesign of the device. As shown in equation (2.7), the sensitivity of a FOG depends on the area enclosed by the coil and the wavelength of the source.

As well, the FOG180 design is based on a former model with lower sensitivity ($L = 1000$ m, $D = 100$ mm) and its design parameters were established, see Table 2.3, to meet the specified requirements which are described in section 2.2.

**Table 2.3.** Design parameters for FOG180 [Moik 2000]

| | | |
|---|---|---|
| Length of optical fiber | $L$ | 3400 m |
| Mean diameter of coil | $D$ | 150 mm |
| Broad spectrum source wavelength | $\lambda$ | 1560 nm |

Using equation (2.7), (2.9) and (2.10) these design parameters yield in theory the basic performance characteristics being listed in Table 2.4.
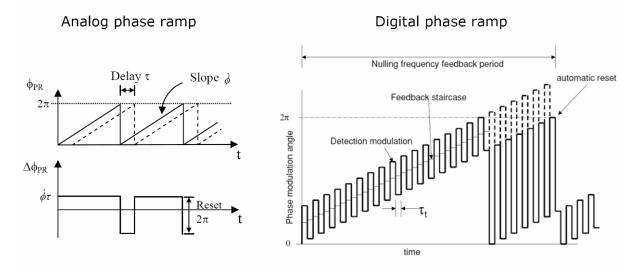
**Table 2.4.**    Theoretical performance characteristics of the FOG180 derived from the design parameters

| | | |
|---|---|---|
| Sensitivity | $\Delta\phi / \Omega$ | 6.8681 s |
| Minimal detectable rate | $\Omega_{min} = \Omega_{\Delta\phi = 1\ \mu rad}$ | 0.03 arc sec/s |
| Dynamic range | $\Omega_{max} = \Omega_{\Delta\phi = \pm\pi}$ | $\pm 26.3\ °/s$ |
| Bandwidth | | 10 kHz |

The bandwidth of the FOG is determined by the minimum response time of the FOG, which is the transit time of the light through the fiber coil. In theory, this yields very high frequencies (with a coil length of $L = 3400$ m about 100 kHz) but in practice, digital signal processing techniques have to be applied that reduce the bandwidth.

**FOG closed loop operation**

For closed loop operation, a phase shift is generated to set the rotation induced phase difference $\Delta\phi$ to zero. The technique used for this is serrodyne modulation where the phase difference $\Delta\phi_{PR}$ is introduced by use of a time-linear phase ramp $\phi_{PR}(t) = \dot{\phi}\,t$ [Lefevre 1993]. The phase ramp modulation $\phi_{PR}$ is applied to the two opposite waves and due to a delay $\tau$ between these two waves a feedback phase difference is generated. Because the ramp cannot be infinite, a sawtooth form of the modulation signal is used with a reset at $2\pi$, see Figure 2.9 left side. Each reset corresponds precisely to $2\pi$ in phase difference and to an angular increment of the rotation. The feedback phase difference is during the ramp equal to $\Delta\phi_{PR} = \dot{\phi}\,\tau$ and after the flyback equal to $\Delta\phi_{PR} = \dot{\phi}\,\tau - \phi_{RS}$ where $\phi_{RS}$ is the phase reset value.



**Figure 2.9.**    Analog (left side) and digital (right side) phase ramp modulation angle $\phi_{PR}$ and induced feedback phase difference $\Delta\phi_{PR}$. [Lefevre 1993, Culshaw 2006].

In [Lefevre 1993], it is shown that the angular increment is depending on the wavelength, the index of refraction and the diameter of the coil. The counting of the positive and negative resets provides then an accurate measurement of the angle of rotation. Instead of a continuous ramp, a digital phase ramp is used which produces phase steps with amplitude of the rotation induced phase shift and with a duration of the delay $\tau$. An applied square-wave biasing modulation synchronizes the phase steps with the resets for any value of the step, see Figure 2.9 right side. Counting the number of modulation frequency periods at reset gives the Sagnac phase. The measurement signal of the gyroscopes is then composed of the number of resets and the number of phase steps after the last reset which is captured in an electronic counter. At the gyroscope output sampling rate, the counter is read out and reset.

**Scale factor**

The raw output data of the gyroscopes are the number of counts captured within one sampling period. Each of the counts corresponds to an angular increment which defines the scale factor *SF*. The number of counts multiplied by the scale factor represents the rotated angle over the previous sampling period. Dividing this angle by the sampling period $t_s$ yields the measured rotation rate $\Omega$:

$$\Omega = \frac{SF \cdot counts}{t_S}$$

(2.11)

The FOG180 scale factor is measured for each gyroscope to approximately 0.00077 arc sec and the gyroscopes are read out with a sampling rate of 400 Hz, respectively a sampling time $t_s = 2.5$ ms. Note that the gyroscopes output is actually the averaged rate over the previous sampling period rather that the instantaneous rate at the sampling instant.

The fiber coil expands with temperature and thereby changes the effective area of the coil altering the scale factor. Measuring the temperature with the internal temperature sensors, the resulting error can be compensated by modeling the scale factor *SF* as a function of temperature with a third order polynomial. The scale factor and temperature coefficients for each of the three gyroscopes are measured and modelled by the manufacturer and can be found in [Faussot 1999, Ly 2003a, Ly 2003b].

**Rate bias**

In practice, when there is no input rate, the output signal of the gyroscopes is not zero. This zero offset is the absolute rate bias of the gyroscopes. It is usually small for FOGs. The absolute rate bias is temperature dependent and can be compensated using the internal temperature sensors. Similar to the scale factor error model, a third order temperature dependent bias model is implemented. The bias and the temperature coefficients are measured and modelled by the manufacturer: Their initial calibration and can be found in [Faussot 1999, Ly 2003a, Ly 2003b]. After some hardware modifications, the bias calibration was repeated. The new calibration coefficients can be found in [Sergeant 2008a-c].

**Random noise sources**

Additionally to the systematic gyroscope errors as scale factor, rate bias and misalignments, see below, the gyroscopes have a random noise error due to different sources. The total noise error is described by the variance of the output rate and is composed by the sum of the variances of the individual noise terms:

$$\sigma^2_{total\ random\ noise} = \sigma^2_{Quantization} + \sigma^2_{Angular\ Random\ Walk} + \sigma^2_{Bias\ instability} + \sigma^2_{Rate\ Random\ Walk} + ... \qquad (2.12)$$

The following gives a short description of the different noise sources. The data analysis techniques and the simulation of the noise processes are described more detailed in section 4.2. The random noise characterization of the three SOFIA gyroscopes follows primarily in section 5.1 and, in addition, under various TA operational modes in section 5.2.

*Quantization Noise*

The readout electronics of the gyroscopes are in terms of counts which correspond to an angular increment, see equation (2.11). Hence, the output signal is discrete and quantized by nature and the quantization represents the minimum resolution level of the sensor [Ng, 1996]. The quantization interval of the measured angle equals an angular increment of about 0.00077 arcsec. Consequently, the quantization interval of the rotation rate becomes 0.31 arcsec/sec for the gyroscope readout rate of 400 Hz. The noise process can be described by white noise with uniform probability density that produces an error in the angular readout, thus it is often referred to angle white noise. It is significant for very short integration times.

*Angle random walk*

The main source of angle random walk (ARW) is spontaneous emission of photons in the light path of the gyroscopes [IEEE 1998]. The noise term is characterized by a white noise spectrum on the gyroscope rate output which has a flat power spectral density (PSD). The rate signal is integrated to yield the measured angle which results in a Wiener process: the integrated white noise becomes a random walk in angle which is typified by a small varying drift with increasing variance as a function of square root of time. It is significant for integration times in the range of seconds.

*Bias instability*

The bias instability is a low-frequency fluctuation that is present in the output signal even if the initial absolute rate bias is removed. The origin is in the electronics and other components sensitive to random flickering. The noise is described by pink noise or 1/f noise where the associated noise PSD decreases with frequency. It is significant for integration times in the range of seconds to minutes.

*Rate random walk*

The origin of the rate random walk (RRW) is uncertain. The noise process is a random walk on the rate, thus the result of integrating acceleration white noise. It is only for large integration times significant. This gyro rate error can be estimated by the tracker. Therefore,

the RRW coefficient is not specified and also not measured by the manufacturer. The values are estimated from the calibration data in section 5.1.

*Rate ramp*
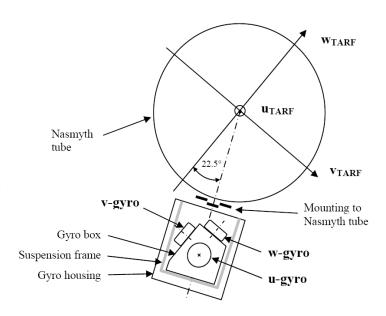
The rate ramp is more a deterministic than a random noise error. It causes a very slow monotonic change in the rate data over a long period of time. The effect of rate ramp on the data is removed by the tracker. As for the RRW, no specification or measurement value is given. The values are estimated from the calibration data in section 5.1.

*Other*

There are other known random noise sources such as sinusoidal noise, which however are considered insignificant by the manufacturer.

**Gyroscope mounting to the telescope structure**

The three gyroscopes are mounted to a precisely machined aluminum box, which is attached by a suspension frame to the gyroscope housing. The gyros are mounted in such a way that their sensing axes correspond to the TARF axes. This is schematically illustrated in Figure 2.10 for a typical operational telescope elevation of 40°.



**Figure 2.10.** Schematic representation of the gyro mounting with respect to the TA, looking aft.

### 2.4.2 Accelerometers

The accelerometers measure the translational accelerations acting along their sensitive axes on the body, on which they are mounted on. The basic working principle is based on measuring the displacement of a proof mass that is connected via springs to an instrument case [Titterton 2004]: If acceleration is acting on the case, the proof mass resists the movement due to its own inertia and is shifted (restricted by the springs) with respect to the instrument case. The measured accelerations include the total acceleration of the body with respect to inertial space and the apparent acceleration caused by Earth's gravitational force $g$. The specific force $f_{measured}$ measured as the output of the accelerometer is composed by:

$$f_{measured} = a - g \qquad (2.13)$$

The real inertial acceleration $a$ is caused by non-gravitational forces.

For the application in SOFIA, the accelerometer outputs are used to correct for the quasi-static bending of the telescope structure and need to include the inertial accelerations and gravitational forces. The six accelerometers within the SOFIA system are Q-Flex accelerometers QA-2000-10 from Honeywell (former: Allied Signal) and are force-feedback pendulous accelerometers. The working principle is shown in Figure 2.11. If a force is acting on the proof mass, the pendulum, it is sensed by the capacitive pickoff. This signal is fed back and an electromagnetic force produced by the forcer coils counteracts the measured accelerations maintaining a centered pendulum position. Three temperature sensors provide information for the scale factor calibration which is temperature dependent. The manufacturer provided the calibration measurement data [Allied Signal 1998].

Typical sensor errors are the measurement bias, caused by null shifts of the pickoff, cross-axis coupling and vibration effects, scale factor errors, caused by temperature effects and random bias, caused by instabilities in the system [Titterton 2004]. The specified performance is shown in Table 2.5 [Allied Signal 1998].
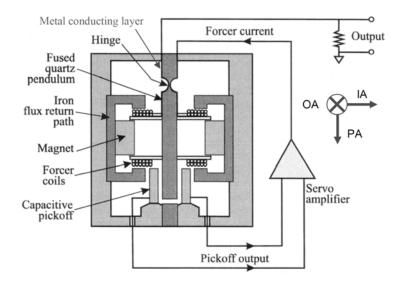


**Figure 2.11.** Working principle of the Q-Flex accelerometer QA-2000 [Lawrence 1999].

**Table 2.5.** Manufacturer specification of the Q-Flex accelerometer QA-2000-10 [Allied Signal 1998].

| | |
|---|---|
| Input range | ± 60 g |
| Bias | 4 mg |
| Bias stability | 550 µg |
| Scale factor stability | 660 ppm |
| Axis misalignment | 105 µrad |
| Resolution/ Threshold | 1 µg |
| Bandwidth | 300 Hz |

**Accelerometer mounting to the telescope structure**

Three accelerometers are mounted on the cube on which the three gyroscopes are attached. These are currently fed forward to compensate for the flexures. For redunancy and a possible extension of the FBC algorithm, three additional accelerometers are mounted on a block on the balancing plate.

### 2.4.3  Imagers

The imagers capture an image of the region of the sky which is covered by their fields of view. The projected fields of the three imagers on the sky are shown in Figure 1.8. The SOFIA imagers operate at visual wavelengths and are equipped with a CCD as detector device. The image is projected through the camera optics on the CCD. The CCD is a light sensitive silicon semiconductor and consists of a capacitor array formed on a silicon substrate. When an exposure starts, the capacitors are charged and then disconnected. Entering photons are absorbed by the silicon crystal and cause a partial discharge of the capacitors by raising electrons from the low-energy valence band state to a high-energy conduction-band state. The number of raised electrons and thus the degree of discharge is proportional to the number of photons that hit each capacitor. When the exposure is finished, the remaining charge is shifted line-by-line to a register and then to an amplifier. Finally, the signals are digitized and stored [Berry 2005]. The energy of a photon needs to be sufficiently energetic to promote the electrons. The photon energy $E_{ph}$ is depending on the wavelength $\lambda$ and determines the red wavelength limit for detection:

$$E_{ph} = \frac{hc}{\lambda} \qquad (2.14)$$

where $h$ is the Planck constant and $c$ the velocity of light.

The intensity distribution of the incoming light during the exposure on the detector array can be reconstructed by the digitized values of the capacitor array. Each capacitor is represented by a pixel (picture element). When the image is binned, several capacitors are represented by one pixel. Mathematically, the digital image corresponds to a two-dimensional matrix. Each pixel has a two-dimensional location defined by the row and column component and it has an intensity value (Figure 2.12).

A raw image has intensity values that are encoded in bytes. Their resolution depends on the number of used bytes. The raw intensity values can be converted from the analog-digital units to the number of photons or other flux units. The number of generated electrons is the product of the quantum
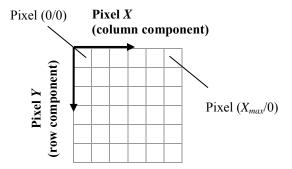


**Figure 2.12.** Construction of a digital image.

efficiency of the CCD and the number of photons.

Photon detection with a CCD is affected by various random noise sources: Read noise, dark current noise, and shot noise in the source and in the sky background. Their variances can be combined and quantified by the signal-to-noise ratio [Howell 2000]. As sensitivity studies are not within the scope of this work the noise characteristics are not described in more detail. However, the overall signal-to-noise ratio directly relates to the uncertainty of star position estimates which are relevant for this work.

Being already introduced in section 1.1.2, the SOFIA telescope has three imagers for target acquisition and tracking. The FPI uses the optics of the main telescope, a folding mirror system to allow for focus adjustments and to reduce the imager dimensions, and a camera lens. The FFI and WFI have separate optics and do not use the main telescope optics (Figure 1.6). The key characteristics of the three imagers are summarized in Table 2.6 [Herdt 1998a]. The detector device is an identical CCD chip model Thomson 7888A for all three imagers. In the near future, an upgrade of the CCD chips is planned to improve the sensitivity of the imagers [Wolf 2008]. The images can be read out with 8 bit/pixel at 5 MHz or with 14 bit/pixel at 2 MHz and pixel binning is available with a 2x2 and a 4x4 option. An integration time between 10 ms and 100 s can be selected. Each of the imager is equipped with a filter wheel with six different filters which are used when tracking on bright targets.

**Table 2.6.** SOFIA imager characteristics [Herdt 1998a].

|  | WFI | FFI | FPI |
|---|---|---|---|
| Optics | Petzval lens | Schmidt-Cassegrain | SOFIA Telescope, folding mirror system and ZEISS camera lens |
| Aperture diameter | 67 mm | 254 mm | 2500 mm |
| Nominal focal length | 135 mm | 710 mm | 5230 mm ± 600 mm |
| Field of view | 6° x 6° | 70 arcmin x 70 arcmin | 8 arcmin x 8 arcmin (Not covered completely by the telescope's FOV) |
| Pixel array | 1024 x 1024 pixel | 1024 x 1024 pixel | 1024 x 1024 pixel |
| Pixel size | 14 μm x 14 μm | 14 μm x 14 μm | 14 μm x 14 μm |
| Image scale as measured by DLR Berlin [Levin 2002] | 20.36 arcsec/pixel | 4.07 arcsec/pixel | 0.55 arcsec/pixel |
| Required sensitivity | 8 mag | 13 mag | 16 mag |
| Derived pointing stability requirement for imagers | 1.8 arcsec | 0.35 arcsec | 0.035 arcsec |

# 3    On sky telescope sensor alignment

This chapter presents the strategy, procedures and algorithms for the pointing control sensor alignment. The sensor alignment is accomplished via alignment matrices that are incorporated into the reference frame concept for the pointing control system that is presented in chapter 2. The compensation methods that correct the pointing errors due to structural deformations are discussed in detail. These pointing errors are also present during the alignment measurements and a combination of compensating the errors during both measurements is proposed. The chapter concludes with the expected alignment accuracies.

## 3.1  Alignment strategy

For ground based telescopes, systematic pointing errors due to misalignment and structural deformations can be compensated by a pointing model [Gillessen 2004]. The required pointing corrections are determined by a set of calibration measurements as a function of the telescope orientation on the sky specified by the coordinates azimuth and altitude (Appendix C.4.2): Multiple measurements across the sky allow generating a vector field. Fitting these discrete measurement points produce the pointing model which represents the reproducable misalignment and flexures of the telescope structure. This method presumes that the drive axes of the telescope are fixed with respect to the Earth and therefore pointing to a certain location on the sky in azimuth and altitude is repeatable.

Space based telescopes are virtually weightless, thus mechanical alignment is free from the perturbations produced by gravity induced flexure. Focal plane alignment and calibration with respect to the pointing sensors is typically performed in-flight to correct for shifts due to launch loads. The science instruments are integrated in the satellite and the detector location is directly calibrated during calibration maneuvers [Bayard 2004]. The gyroscope calibration and alignment is performed with a separate procedure including misalignment, scale factor and bias estimation [Davenport 1988]. Satellite alignment and calibration maneuvers can be executed over a wide range of motion.

For the KAO telescope the gyroscope package was mounted on the primary mirror structure and alignment between the sensors and the focal plane was accomplished manually as the controller was analog. No specific alignment was performed within the control system.
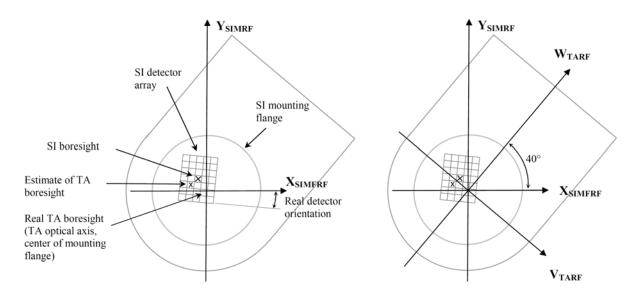
For the SOFIA telescope, the pointing requirements are more stringent and the telescope structure is more flexible demanding for sensor alignment. The alignment measurements are performed on ground and include flexure compensation due to gravity. The alignment concept is independent of an absolute telescope orientation with respect to the sky and the sensors are aligned relative to the focal plane. Only a limited motion range is available for the on sky alignment maneuvers on the ground: Observations can be performed in elevation from 20° to 60° and within the FD motion range of $\pm\,3°$.

The theoretical concept for SOFIA's pointing control system is based on a set of Cartesian reference frames and is described in detail in section 0. The reference frame that reflects the telescope pointing at the focal plane is described by TARF. TARF is mathematically manipulated in such a way that it represents the telescope pointing for a rigid and perfectly aligned telescope. The projected origin of TARF onto the focal plane represents the TA boresight and the reference frame axes represent the rotation axes of the telescope. The calibration and alignment of the pointing control system requires first the definition of TARF with a special test instrument located at the SI mounting flange. This reference instrument is designed such that the projected center of the flange on the detector is known precisely, as well as the orientation of the detector with respect to the SI mounting flange. Then, calibration measurements are made of the relationships between TARF and the reference frames of the sensors which identify the pointing and the telescope motions. The measurements include the three imagers and the gyroscopes. In addition, flexures and other deformations are measured in order to correct TARF and create a virtual, rigid TA.

Accurate alignment of the telescope rotation axes is especially necessary for the LOS axis. If properly aligned, a star imaged at the TA boresight stays exactly at this location during a LOS rotation. Any misalignment of the TA rotation axes with respect to the focal plane causes the star to move. As LOS rotations are frequently performed between observations to enable inertial stabilization, the alignment is vital for efficient observing runs.
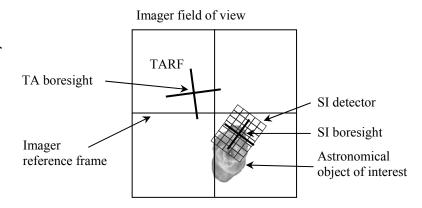
After calibrating TARF within the pointing control system using the reference instrument at the focal plane, the reference instrument is demounted. The calibrated pointing control sensors are now the reference for TARF for any subsequently mounted SIs. Each SI itself has an optical axis, the SI boresight. It is generally at a fixed pixel location on the detector array, but may vary depending on the optical configuration. The SIs are complex imaging systems and it is possible that within their internal imagers, the instruments may have an arbitrary number of boresights. Using laboratory calibration data and design information, the science instrument team provides the SI boresight location and an approximate location of the TA boresight on the detector array, as well as the orientation of the detector with respect to the SI mounting flange. This information provides the first estimate for the relation between TARF and the SI detector array which is represented by the SI Reference Frame (SIRF). Initial pointings on the sky are accomplished to refine the relation between TARF and SIRF using the previously calibrated pointing sensors. Figure 3.1 illustrates the estimated and real

location and orientation of a detector array with repect to the SI mounting flange. The SI Mounting Flange Reference Frame (SIMFRF) has an known offset of 40° with regard to TARF due to the telescope storage elevation at 40°. It was decided to use this orientation to define the nominal SIRF. The reference frames are defined in Appendix C. The orientation of SIMFRF to TARF is shown in Figure 3.1 on the right side.



**Figure 3.1.** Schematic representation of location and orientation of an SI detector array with respect to the science instrument mounting flange (left side). The science instrument teams provide the information with respect to the SI mounting flange reference frame (SIMFRF). The real location and orientation may differ. The orientation of the mounting flange reference frame to the TARF is shown on the right side.

A possible scenario of TARF and SI detector orientation as seen in an imager field of view is shown in Figure 3.2. TARF represents the pointing of the telescope on the sky and does not coincide with the imager reference frame due to misalignments and telescope deformations. As well, the SI detector has an orientation that differs from TARF and the imager reference frames. Once calibrated, the known rela-



**Figure 3.2.** SI detector and boresight, TARF and the astronomical object of interest as projected in the imager field of view, after [Davidson 2003]. The imager boresight is represented by the origin of the imager reference frame

tion between TARF, the imagers and the SI detector enables the target acquisition and tracking for the science observations.

## 3.2 Alignment procedures

During alignment and calibration of the TA, the High-speed Imaging Photometer for Occultations (HIPO) is used as a reference instrument at the focal plane. It is one of the first-light science instruments for SOFIA and is involved in the telescope functional and performance testing and is therefore provided with specific design features [Dunham 2004a]. These include a very robust mechanical design ensuring only minor deflections due to gravity and a lowest resonance frequency at about 110 Hz, well beyond the structural frequencies that the pointing control system can address. HIPO has a removable Shack-Hartmann lenslet array, which provides wavefront error measurement information and makes an effective tool for focusing and aligning. Furthermore, HIPO's optical design includes a precisely located light source. It injects light from an internal LED at a known location relative to the SI mounting flange, through a pinhole at the focal plane into the telescope. A spherical button mirror mounted in the center hole of the secondary mirror reflects and re-images the light back into HIPO. This procedure permits measurements of the location and motion of the active secondary mirror. HIPO also has a pupil imaging mode. Beside its science application, HIPO will be used regularly for alignment and calibration during the operational lifetime of SOFIA. This happens especially after demounting of the optical components for coating and cleaning when the realignment of the telescope optics has to be verified.

However, before alignment and calibration measurements of TARF and the sensor reference frames are performed, coarse mechanical alignments are performed on the telescope's optical assembly which include:
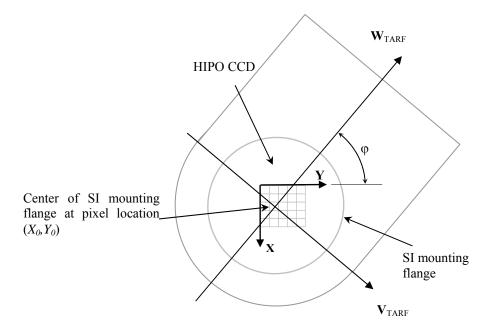
- the collimation of the primary mirror to the secondary mirror,
- the alignment of the mechanical axes of the secondary mirror Focus and Centering Mechanism (FCM) to the primary mirror axis,
- the alignment of the headring imagers (WFI and FFI) optical axes to the primary mirror optical axis,
- the pupil matching of the nominal FPI pupil position to the secondary mirror representing the exit pupil of the telescope.

The optical assembly alignment and verification plan is described in [Erdmann 2001] and [Erhard 2004]. The optical alignment is afterwards measured using the HIPO Shack-Hartmann test capability [Haas 2005]. The optimum decenter and focus position of the secondary mirror is determined for optimum image quality. The position of the FCM is then kept constant over the course of the following sensor alignment measurements.

The alignment and calibration procedures are performed with HIPO using astrometric references on the sky. The alignment sequence is split into three consecutive parts:

The first part of the on sky alignment consists of determining the position of the TA boresight with HIPO relative to the TA imagers. A star is brought into the field of view of HIPO and

centered on the SI flange, i.e. at a calibrated pixel location in the HIPO detector. This pixel location identifies where the projected origin of TARF is located at the SI flange. Figure 3.3 shows the known location and orientation of the HIPO CCD with respect to the SI mounting flange for a typical operational telescope elevation of 40° [Dunham 2004b]. Pixel location $(X_0, Y_0)$ on the HIPO CCD is measured to be the center of the flange with a known accuracy.

By comparing the centroid locations in the other telescope imagers, the origin of TARF is identified within these fields of view and recorded by pixel locations. The relations of the pixel locations on the HIPO CCD and on each of the imager CCDs are defined depending on image scale and the imager boresight positions relative to TARF. As the telescope structure flexes due to gravity, the relative alignment relationships for the imagers and the HIPO reference location also change for different elevation angles. For the FPI, the boresight position is additionally dependent on temperature variations. These dependencies are reflected in the camera alignment matrices with respect to TARF.
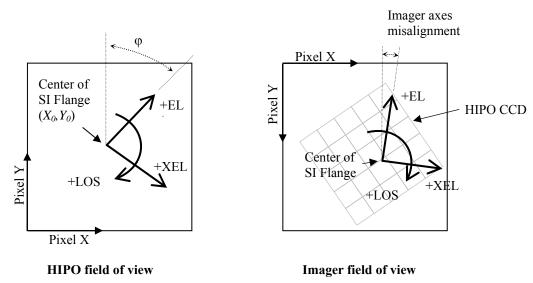


**Figure 3.3.** Defining TARF with HIPO at the SI mounting flange.

The second part consists of making the telescope rotation axes conjugate with the TARF axes. The orientation and position of HIPO on the telescope not only define the origin of TARF at the center of the SI flange but also the orientation of the TARF axes as projected on the focal plane. Laboratory measurements of the alignment of the rows and columns of the HIPO CCD detector – relative to the science instrument flange mount pins – enable HIPO to be used to define the telescope motion axes with a known accuracy. The telescope axes alignment measurements are done by commanding motions about the initially estimated TARF axes, while observing the motions of a bright star in the HIPO images. At initial setup of the TA, TARF is assumed to be conjugate with the gyroscope axes defining GYRF by their sensing axes. As the gyroscopes serve as feedback sensors in the telescope attitude control loop, the in

TARF commanded rotations lead to a rotation about the gyroscope axes. Comparing centroid measurements and recorded gyroscope attitude data during these processes permits the rotational alignment relationship between TARF and GYRF to be quantified. The GYRF to TARF alignment ensures that an executed rotation about one of the TARF axes is reflected properly on the HIPO CCD, i.e. the focal plane. The GYRF axes are assumed to be orthogonal to each other, because the gyroscope box in which the gyroscope are mounted was measured to have non-orthogonality errors in the region of only 20-40 arcsec. On the left side of Figure 3.4, it is shown how the telescope rotations, i.e. the TARF axes, are defined on the HIPO CCD. After the gyroscope alignment, HIPO's field of view moves along the designated axes due to rotations about EL, XEL and LOS in TARF. Image motion takes place in the opposite direction.

The third part consists of determining the axes orientation of the three imagers. TARF's origin in the imager was already defined in the first part and with it the misalignment of the imager boresight (the center of the CCD) to TARF. Here, the misalignment of the EL- and XEL-axes is assessed. If the gyroscope misalignment is already compensated, the commanded telescope rotations are performed about the TARF axes. The image centroid measurements before and after a move are again compared to the target position. Figure 3.4, on the right side, shows the field of view of an imager and the projected TARF axes as defined by the HIPO CCD. Maximizing alignment accuracies, the maneuvers are performed over the whole imager field of view.



**HIPO field of view**                    **Imager field of view**

**Figure 3.4.**  Calibrating TARF with HIPO CCD. Column and Row Axes Orientation of HIPO and an imager CCD and the telescope rotations EL, XEL and LOS on the sky as seen in these CCDs. The pixel reference frames are indicated for HIPO in the left lower corner and the imagers in the left upper corner.

Finally, the influence of the telescope structural deformation due to gravity is determined. The three parts of the alignment sequence are repeated at various elevations over the telescope
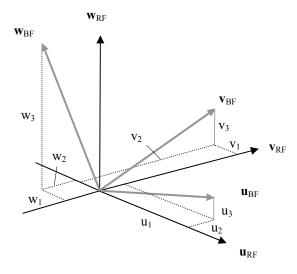
elevation range. In this way, relative flexures between the focal plane, the imagers and the gyroscopes can be assessed.

## 3.3   Alignment algorithms

The set of Cartesian reference frames are aligned by means of transformation matrices which described the body or sensor attitude with respect to a reference frame. Each frame is an orthogonal, right-handed coordinate frame or axis set. The various mathematical representations that can be used to describe such a transformation are described in detail in Appendix B.1. The alignment matrices that are derived in this chapter are based on the Direction Cosine Matrix (DCM). In general, the attitude matrix **A** of the Body reference Frame (BF) with coordinates u, v, w with respect to a Reference Frame (RF) with coordinates 1, 2, 3 is composed with the three unit vectors **u**, **v**, **w** of the BF expressed in the RF:

$$
\mathbf{A}_{BF,RF} = \begin{pmatrix} u_1 & v_1 & w_1 \\ u_2 & v_2 & w_2 \\ u_3 & v_3 & w_3 \end{pmatrix}
\tag{3.1}
$$
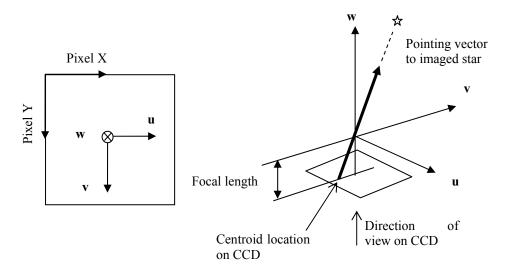
The illustration given in Figure 3.5 shows the definition of the DCM. Its components represent unit vectors $\mathbf{u_{BF}}$, $\mathbf{v_{BF}}$ and $\mathbf{w_{BF}}$ in body axes projected along the reference axes.



**Figure 3.5.**   Defintion of direction cosine matrix describing the orientation of a Body reference Frame (BF) with respect to a Reference Frame (RF).

### 3.3.1   Boresight definitions in HIPO and imager boresight alignment

The centroid location recorded in HIPO and the imagers can be translated into pointing vectors described in the according imager reference frame using perspective projection. The imager reference frames are defined along the column and rows of the imager CCD chip, see Figure 3.6 and Appendix C [Schmolke 2001a]. The imager boresight at the center of the chip at pixel location (511.5/511.5) defines the origin of the reference frame. The axes **u**, **v**, **w** indicate the direction of the telescope axes.



**Figure 3.6.**   Definition of imager coordinate systems [Schmolke 2001a] and simplified perspective projection.

A star that is positioned in the optical axis (or the w-axis) of the imager produces a centroid at the center of the CCD. All other star positions produce centroids that are offset from the CCD center position according to the angular position of the star with respect to the optical axis and the focal length of the optical system.

The relation of the centroid location on the CCD in pixel coordinates and the pointing vector in the imager reference frame XYIRF (XYI stands for WFI, FFI and FPI) are expressed by:

$$u_{XYIRF} = \frac{(X - X_0)}{\sqrt{(X - X_0)^2 + (Y - Y_0)^2 + \frac{1}{S^2}}} \tag{3.2}$$

$$v_{XYIRF} = \frac{(Y - Y_0)}{\sqrt{(X - X_0)^2 + (Y - Y_0)^2 + \frac{1}{S^2}}} \tag{3.3}$$

$$w_{XYIRF} = \sqrt{1 - u_{XYIRF}^2 - v_{XYIRF}^2} \qquad (3.4)$$

where $(X_0/Y_0)$ is the center of the CCD chip in pixel (for 1x1 binning 511.5/511.5) and $S$ is the image scale in [rad/pixel]. The image scale $S$ is the size of a pixel divided by the focal length of the imaging system (WFI: 21.39 arcsec/pixel, FFI 4.07 arcsec/pixel and FPI 0.554 arcsec/pixel). Image distortions are not considered although they can be compensated within the SOFIA tracker system.

HIPO's column ($X$) and row ($Y$) axes forming the pixel coordinate system are parallel to the plane of the SI flange and are rotated by an angle $\varphi$ to the $v_{TARF}$ and $w_{TARF}$ axes, as shown in Figure 3.3. Accounting for the readout electronics of HIPO, the origin of the pixel coordinate system ($X, Y$) of a displayed image is at the lower left corner, pixel numbers run in X direction from 1 to 1152 and in Y direction from 1 to 1030. TARF's origin is desired to coincide with the center of the SI mounting flange, which, as mentioned, is identified to be at pixel location $(X_0, Y_0) = (559/489)$ with an accuracy of ±6 pixels (2 arcsec on the sky). The orientation of the HIPO CCD axes is specified relative to the SI flange by an angle $\varphi = 40.181°$ with an accuracy of ±2.4 arcmin [Dunham 2004b][1]. The relation between the TARF coordinates $u, v, w$ of the respective pointing vector and the HIPO pixel coordinates $X, Y$ of the centroid is described by:

$$u_{TARF} = \frac{(Y_0 - Y)\sin\varphi - (X_0 - X)\cos\varphi}{\sqrt{(X - X_0)^2 + (Y - Y_0)^2 + \frac{1}{S^2}}} \qquad (3.5)$$

$$v_{TARF} = \frac{(Y_0 - Y)\cos\varphi + (X_0 - X)\sin\varphi}{\sqrt{(X - X_0)^2 + (Y - Y_0)^2 + \frac{1}{S^2}}} \qquad (3.6)$$

$$w_{TARF} = \sqrt{1 - u_{TARF}^2 - v_{TARF}^2} \qquad (3.7)$$

where $S = 1.5853\text{e-}006$ is the image scale in [rad/pixel]. The image scale corresponds to 0.327 arcsec/pixel.

---

[1] In 2008, the flange fiducial measurements were repeated: The new HIPO pixel coordinates of the location of the center of the flange are $(X_0, Y_0) = (542.8, 480.2)$ with an accuracy of ±1.5 pixels (about 0.5 arcsec on the sky). The orientation of the HIPO CCD axes is specified relative to the SI flange by the angle $\varphi = 39.81° \pm 0.01°$ [Dunham 2008]. However, for the following descriptions and test evaluations, the values from 2004 are used.

When a star is brought into the field of view of HIPO and centered on TARF's origin as described earlier, the origin of TARF can be identified in the imager field of views and recorded by pixel locations. The calculated pointing vectors in the XYIRF reflect then the w-axis of TARF in their field of views. The misalignment is described by the matrix $\mathbf{A}_{\text{TARF,XYIRF}}$. It is composed of three vectors, representing the axes of TARF as measured in the XYIRF, see equation (3.1).

The composition of the transformation matrix is schematically shown in Figure 3.7. Regarding boresight measurements, only the w-axis of TARF is measured in the XYIRF. Potential misalignments of the u- and v-axes are considered in section 3.3.3. For calculating the u and v components of the matrix, it is assumed that the u-axis has no misalignment component in the v-axis direction ($u_2 = 0$). It would be possible to assume this for the v-axis with no misalignment component in the u-axis ($v_1 = 0$). However, differences are very small and negligible. If it is assumed, that the axes of the XYIRF are orthogonal (inner product of vectors are zero), that all vectors are unit vectors and the XYIRF axes are not more than 90° misaligned, the remaining components of the alignment matrix can be calculated with:

$$u_1 = \sqrt{\frac{w_3^2}{w_1^2 + w_3^2}} \; ; \qquad u_2 = 0; \qquad u_3 = \frac{-u_1 w_1}{w_3} \tag{3.8}$$

$$\mathbf{v} = \mathbf{w} \times \mathbf{u} \tag{3.9}$$
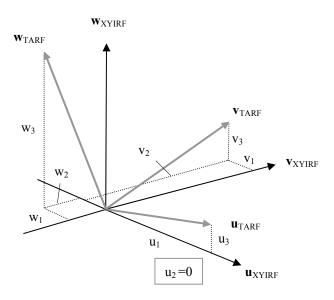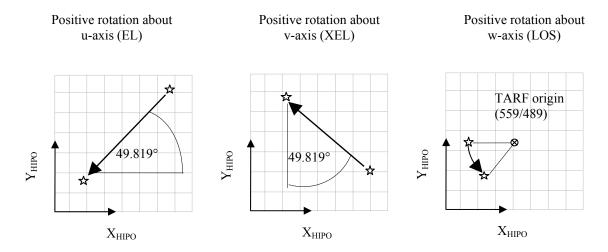


**Figure 3.7.** Derivation of DCM for misalignment of w-axis. It is assumed that u- and v-axes are not misaligned ($u_2 = 0$).

### 3.3.2 Gyroscope axes alignment

As a star centroid movement displayed on the HIPO CCD is directly related to the telescope rotation in TARF, the misalignment between the GYRF and TARF can be assessed by the following method. The telescope is pointing at a star visible in HIPO's field of view. Then, rotations of specific angles are commanded for each TARF axes successively. Figure 3.8 shows exemplarily the centroid motions of an imaged star due to telescope rotations.



**Figure 3.8.** Column and Row Axes Orientation of HIPO CCD and centroid motion due to telescope rotations EL, XEL and LOS.

The actual locations of the starting and end pixel coordinates of the centroid are compared to the values for the perfectly aligned case and their deviations yield the reference frame misalignments that must be corrected. The centroid is placed in the corner of the CCD at start, making rotations as large as possible while keeping the centroid in the field of view.

For the LOS rotations, the centroid is located initially near the location in HIPO that has been measured to be at the center of the SI mounting flange, TARF's origin. Ideally, if the star is located at the center of the flange, its centroid remains at that pixel location during LOS rotations. In Figure 3.9, the centroid motion of an imaged star on the HIPO CCD is shown when a rotation is performed about a misaligned gyroscope LOS-axis. At the beginning of the maneuver, the centroid is located at pixel location B and moves along the trajectory to pixel location E after the move has ended. The pixel location of the projected turning point T on the CCD represents the projected LOS-axis and
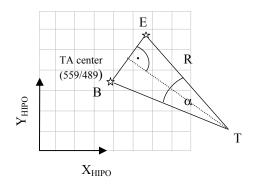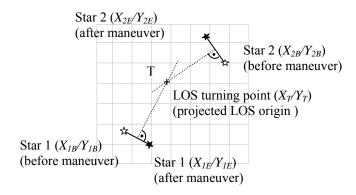


**Figure 3.9.** Centroid positions at begin (B) and at end (E) of a LOS rotation when gyroscopes are misaligned. The true LOS turning point T is derived geometrically and is in this example outside the CCD array.

can be geometrically constructed. If misalignment angles are assumed to be small, the angular distance between the turning point and TARF's origin is calculated by following equation (Figure 3.9):

$$R = \frac{\sqrt{(X_E - X_B)^2 + (Y_E - Y_B)^2}}{2\sin(\alpha/2)} \tag{3.10}$$

Where $R$ is the misalignment angle, $\alpha$ is the commanded rotation angle about the w-axis, and $X$, $Y$ are the pixel locations of the centroids. Calculating the theoretical pixel values of the LOS turning point, although not necessarily on the CCD chip, requires consideration of the centroid location before and after the move and the rotation direction. These dependencies are not derived as a more general method for calculation of the misaligned axes is presented.

If two or more stars are available within the field of view, another method can be applied to calculate the projected turning point. It determines the turning point location by intersecting the connecting lines of two stars before and after an alignment maneuver (Figure 3.10).



**Figure 3.10.** Calculating the turning point T of a LOS rotation using two stars.
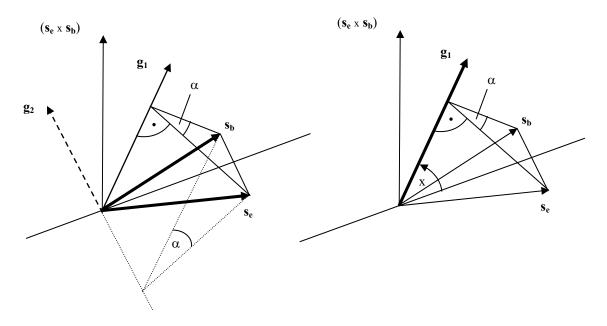
Using the naming convention of the pixel coordinates for the two stars before and after the alignment maneuvers in Figure 3.10, the pixel coordinates of the turning point are given by:

$$X_T = \frac{(Y_{1E} - Y_{1B})(Y_{2E}^2 - Y_{2B}^2 + X_{2E}^2 - X_{2B}^2) - (Y_{2E} - Y_{2B})(Y_{1E}^2 - Y_{1B}^2 + X_{1E}^2 - X_{1B}^2)}{2[(X_{1B} - X_{1E})(Y_{2E} - Y_{2B}) - (X_{2B} - X_{2E})(Y_{1E} - Y_{1B})]} \tag{3.11}$$

$$Y_T = \frac{2(X_{1B} - X_{1E})x_T + (Y_{1E}^2 - Y_{1B}^2 + X_{1E}^2 - X_{1B}^2)}{2(Y_{1E} - Y_{1B})} \tag{3.12}$$

In general, the rotation vector for a rotation of a known angle between two vectors can be determined using pointing vectors. The pointing vector at the beginning of the rotation and at the end of the rotation is calculated in TARF coordinates, equations (3.5)-(3.7). Then, a rotation axis is sought that rotates TARF about the known angle in such a way that the

orientation of the pointing vector at start coincides with the pointing vector at the end after the rotation. In Figure 3.11, left, the situation is sketched with the pointing vector at begin ($\mathbf{s_b}$), at the end ($\mathbf{s_e}$) and the known rotation angle α. If only two vectors are given, all unit vectors lying in the bisection plane (plane composed of bisection and the cross product of the two vectors) are possible rotation axes. In case of a known rotation angle α, there are only two possibilities of a vector orientation left, $\mathbf{g_1}$ and $\mathbf{g_2}$, that can represent the desired rotation axis.



**Figure 3.11.** Derivation of the rotation axis for the known start and end positions of the pointing vector and rotation angle.

On the figure's right side, an angle $x$ is introduced that describes the rotation axis orientation in the bisection plane. For $x = 0$ a rotation of 180° has to be accomplished, whereas for $x = 90°$ the smallest possible rotation is performed. With the two known vectors and the rotation angle α, $x$ is calculated by:

$$x = \arcsin\left(\frac{|\mathbf{s_e} - \mathbf{s_b}|}{|\mathbf{s_e} + \mathbf{s_b}| \cdot \tan(\alpha/2)}\right) \tag{3.13}$$

Consequently, the two rotation axes are composed with:

$$\mathbf{g_1} = \cos x \cdot \frac{(\mathbf{s_e} + \mathbf{s_b})}{|\mathbf{s_e} + \mathbf{s_b}|} + \sin x \cdot \frac{(\mathbf{s_e} \times \mathbf{s_b})}{|\mathbf{s_e} \times \mathbf{s_b}|} \tag{3.14}$$

$$\mathbf{g_2} = -\cos x \cdot \frac{(\mathbf{s_e} + \mathbf{s_b})}{|\mathbf{s_e} + \mathbf{s_b}|} + \sin x \cdot \frac{(\mathbf{s_e} \times \mathbf{s_b})}{|\mathbf{s_e} \times \mathbf{s_b}|} \tag{3.15}$$

Since the LOS axis is always pointing out of the CCD plane and in the same direction as the pointing vectors by principle, the solution is always $\mathbf{g_1}$.

Contrary to the LOS maneuvers, the angle $x$ for EL and XEL rotations is close to 90° and both calculated rotation axes are possible solutions. The correct solution can not be determined from these measurements. The two possible rotation vectors differ in the sign of the out of the plane component (LOS). Assuming that the three rotation axes are orthogonal and the EL and XEL alignment maneuvers are performed after the alignment of the LOS-axis, the two possible rotation axes coincide. The projected EL- and XEL-axes lie in the CCD plane and have no misalignment component out of plane. If measurement errors do not produce two matching rotation axes, the rotation axis is estimated by setting its LOS component to zero and normalizing the result.

Simplified, the misalignment can also be calculated by measuring the angles $\beta_{EL}$ and $\beta_{XEL}$ between the connecting line of starting and ending centroid locations and the defined TARF EL, respectively XEL axis on the CCD. The maneuvers are illustrated in Figure 3.12.
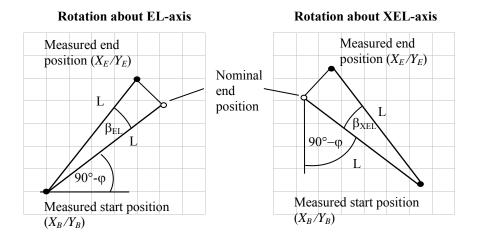


**Figure 3.12.** Derivation of misalignment angle for alignment maneuvers about EL and XEL axes.
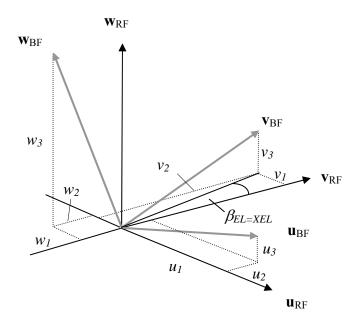
For rotations maneuvers about the EL-axis, the misalignment angle $\beta_{EL}$ is calculated by equation (3.16). Respectively, for maneuvers about the XEL-axis, the misalignment angle $\beta_{XEL}$ is calculated by equation (3.17). If the LOS-axis is properly aligned while the maneuvers are performed, the results for both angles match.

$$\beta_{EL} = \arctan\left(\frac{X_E - X_B}{Y_E - Y_B}\right) - \left(90° - \varphi\right) \tag{3.16}$$

$$\beta_{XEL} = \arctan\left(\frac{Y_E - Y_B}{X_E - X_B}\right) - \left(90° - \varphi\right) \tag{3.17}$$

where $\varphi$ is the angle between the pixel axes and the projected TARF axes, see Figure 3.4.

The misalignment is described by the alignment matrix $\mathbf{A}_{\text{TARF,GYRF}}$. It is composed with the three determined rotation vectors which represent the rotation axes of TARF as seen in the GYRF, see equation (3.1). The matrix for describing only the LOS-axis misalignment can be composed using equations (3.8) and (3.9).



**Figure 3.13.** Derivation of DCM for misalignment of u, v and w-axes.

Simplified, the alignment matrix can be also calculated by the measured misalignment angle $\beta_{EL=XEL}$ and the latest w-axis calculation:

$$v_2 = \sqrt{\frac{1}{(\tan^2 \beta + 1) + \left(\dfrac{w_1 \tan \beta + w_2}{w_3}\right)^2}} \ , \ v_1 = \tan \beta \cdot v_2 \ , \ v_3 = \frac{-v_1 w_1 - v_2 w_2}{w_3} \tag{3.18}$$

$$\mathbf{u} = \mathbf{v} \times \mathbf{w} \tag{3.19}$$

As above, it is assumed that the axes of the GYRF are orthogonal (inner product of vectors are zero), that all vectors are unit vectors and the GYRF axes are not more than 90° misaligned. The aligned gyroscope rates represent the angular velocity about the TARF axes; the measured gyroscope rates represent the GYRF axes. The telescope rotation rate in TARF is yielded by:

$$\omega_{TARF} = A_{TARF,GYRF} \, \omega_{GYRF} \tag{3.20}$$

### 3.3.3   Imager rotation of field alignment

The rotation of field between the imager reference frames and TARF can be measured using the simple EL/XEL rotations above. Assuming that the LOS-axis misalignment angle is small and that the GYRF:TARF misalignment is already compensated, the EL/XEL misalignment of the imager axes can be described by the matrix $\mathbf{A}_{\text{XYIRF,GYRF=TARF}}$. It is composed of three vectors, representing the axes of XYIRF as measured in TARF, see equation (3.1). The matrix components can be calculated using equations (3.14) and (3.15) with the pointing vector solution or equations (3.18) and (3.19) using the solution with the projected pointing vectors.

Another possibility of determining the rotation of field relations between the imagers is using star field recognition software. The images must contain at least five stars depending on the software used to identify the star field and its orientation on the sky. Typically, this is only possible for the FFI and WFI if images of both cameras are recorded at the same time. Comparison of the image orientation to the North position yields the relative orientation of the FFI and WFI.

## 3.4   Implementation of alignment and calibration corrections
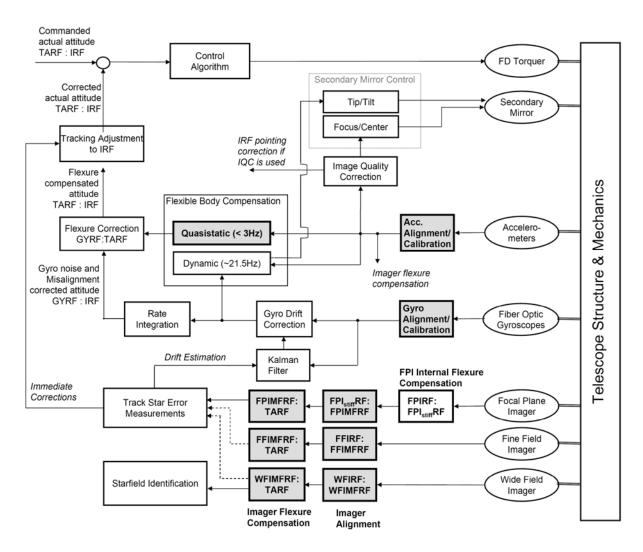
The measured misalignments of the sensors with respect to the focal plane are corrected within the control software by the alignment matrices described in [Lattner 2000, Moik 2000]. They may depend on temperature and accelerations (including gravity) which act on the telescope structure. Table 3.1 gives an overview of the provided alignment matrices and calibrations for compensating the sensor misalignments due to mounting and telescope structural deformations within the pointing control system. The table includes their error sources and dependencies and lists the sensors that can be used to identify the calibration and alignment matrices. The table includes only the error sources that are compensated within the matrices. Sensor noise that varies over time (angular random walk, etc.) is corrected by the tracking loop and not listed. The implementation of the matrices within the pointing control system introduced in chapter 2 is shown in Figure 3.14. The alignment matrices and calibrations that are treated within this chapter are highlighted in grey.

In general, the gyroscopes, the accelerometers and the imagers are compensated for misalignment with respect to a mounting location and for flexure with respect to the focal plane. The accelerometers are mounted within the gyroscope box. Their axes misalignment is assumed as a first order approach to be equal to the gyroscope axes misalignment. Internal bending of the FPI and deformations due to temperature can be compensated with a distinctive matrix.

The required calibration matrices for the Flexible Body Compensation (FBC) are determined initially with a finite element model and are improved later on with data from the modal survey test on the ground and in flight [Süß 2002]. However, the pure static portion, i.e. the telescope flexures due to gravity, is contained in the measurements on the ground.

**Table 3.1.**   Provided alignment matrices for compensating sensor misalignment and structural deformations of the telescope structure.

| Reference frames | Error source | Dependencies | Sensors used for calibration |
|---|---|---|---|
| **Telescope assembly reference frame** | | | |
| GYRF:TARF | Quasi-static flexure (< 3 Hz) | Low pass filtered accelerations (includes gravity vector) | HIPO, gyroscopes, accelerometers |
| Secondary mirror tip/tilt commands | Dynamic flexure (Dumbbell mode ~21.5 Hz) | Band pass filtered accelerations, gyroscope rates | HIPO, gyroscopes, accelerometers |
| **Accelerometer reference frame** | | | |
| ACCRF: TARF | Misalignment, calibration | Temperature | Acc, Gyros, CD encoder |
| **Gyroscope reference frame** | | | |
| GYRF:GYRF$_{initial}$ | Misalignment, calibration | Temperature | gyroscopes, HIPO |
| **Imager reference frames** | | | |
| FPIRF:FPI$_{stiff}$RF | Internal flexure due to gravity, temperature deformation | Gravity vector, Temperature | FPI, HIPO |
| FPI$_{stiff}$RF:FPIMFRF | Misalignment to mounting flange | | FPI, gyroscopes |
| FPIMFRF:TARF | TA flexure due to gravity | Gravity vector | FPI, HIPO, gyroscopes |
| FFIRF:FFIMFRF | Misalignment to mounting flange | | FFI, gyroscopes |
| FFIMFRF:TARF | TA flexure due to gravity | Gravity vector | FFI, HIPO, gyroscopes |
| WFIRF:WFIMFRF | Misalignment to mounting flange | | WFI, gyroscopes |
| WFIMFRF:TARF | TA flexure due to gravity | Gravity vector | WFI, HIPO, gyroscopes |
| **Secondary mirror reference frame** | | | |
| SMARF:TARF | Misalignment | | HIPO, FPI |
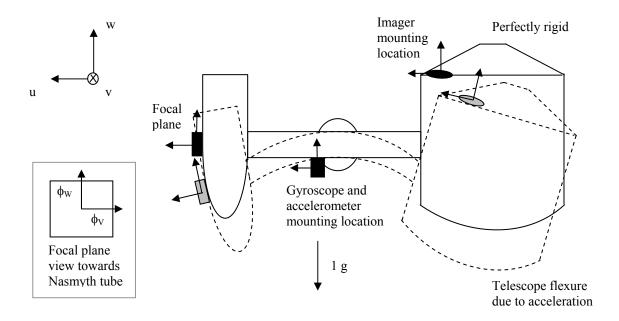
**Figure 3.14.** Schematic representation of the pointing control system. The alignment matrices that are treated within this chapter are highlighted in grey.

### 3.4.1 Compensating flexures with respect to a perfectly rigid telescope

The quasi-static deformations of the telescope structure are caused by gravity and low frequent aircraft acceleration. When the deformations occur slowly, there is approximately a simple linear relation between the accelerations acting on the telescope structure and the image motion on the telescope focal plane, respectively on the imager focal planes. The three accelerometers in the gyroscope box are used to measure these accelerations. The image motion on the focal plane is compensated within the pointing control loop by the quasi-static FBC. It modifies the relation TARF:GYRF causing a telescope move without changing the commanded TARF:IRF relation. The image motion on the imager focal planes is reflected by alignment matrices. The perfectly rigid telescope and the flexure of the telescope due to gravity are shown schematically in Figure 3.15 for a telescope elevation of 90°. The telescope is dumbbell shaped and supported by the spherical bearing in the center of the Nasmyth tube. The metering structure on the one side and the balancing plate on the other side sag down due

to the 1 g acceleration load on the structure. The geometric relations between the telescope sensors and the focal plane are changing depending on their location on the telescope structure. The gyroscopes are mounted close to the bearing and do not change their orientations significantly. In contrast, the locations of the focal plane and of the two head ring imagers are displaced.



**Figure 3.15.** Schematic representation of perfectly rigid telescope and the deformation of the telescope and corresponding sensor displacements when gravity is acting on the telescope at an elevation of 90°. This corresponds to the load case of 1 g acceleration in negative w-direction.

The image motion on the focal plane is caused by the displacements and rotations of the optical elements of the telescope in the light path. It can be calculated using the ray trace equation which reflects the mechanical motions of the three mirrors and the focal plane. The according formulas can be found in [Süß 2004a] and [Moik 2000]. Calculations with a finite element model combined with the ray trace equation deliver the approximated relation between the pointing error due to flexure and the accelerations acting on the telescope structure that cause the flexures.

The result of the computations is a matrix which describes the two-dimensional image motion on the focal plane and out of plane (focus change) for three load cases. For each load case an acceleration of 1 g is applied to the gravity-free telescope along the EL-, XEL- and LOS-axis. The results are listed in Table 3.2 [Süß 2004a]. Note, that all signs are inverted to reflect the image motion, whereas the technical note from Süß reflects the compensation for image motion.

**Table 3.2.** Image motion on focal plane due to the three load case accelerations after [Süß 2004a] (compare Figure 3.15).

| Image motion | Equivalent telescope motion | 1 g acceleration in u-direction | 1 g acceleration in v-direction | 1 g acceleration in w-direction | Units |
|---|---|---|---|---|---|
| $\Delta U$ | focus change | -6.200 | -0.100 | 10.952 | mm |
| $\phi_V$ | $-\Delta$EL | 0.455 | -2.107 | 0.612 | arcsec |
| $\phi_W$ | $-\Delta$XEL | 8.594 | -0.061 | -69.902 | arcsec |

The image of the sky appears mirrored on the focal plane due to the uneven number of telescope mirrors. Additionally, the image axes are rotated about 90° due to the ray redirection of the tertiary mirror. The image motion on the focal plane is described by two angles $\phi_V$ and $\phi_W$, which accordingly correspond to a negative telescope rotation about the u-axis (-$\Delta$EL), respectively to a negative rotation about the v-axis (-$\Delta$XEL).

The image motion at the focal plane is calculated with the measured accelerations *acc* and the values for the calculated load cases from Table 3.2 by:

$$\Delta U \; [mm] \; = \frac{-6.2}{g} acc_U + \frac{-0.1}{g} acc_V + \frac{10.952}{g} acc_W \tag{3.21}$$

$$\phi_V \; [arcsec] \; = \frac{0.455}{g} acc_U + \frac{-2.107}{g} acc_V + \frac{0.612}{g} acc_W \tag{3.22}$$

$$\phi_W \; [arcsec] \; = \frac{8.594}{g} acc_U + \frac{-0.061}{g} acc_V + \frac{-69.902}{g} acc_W \tag{3.23}$$

If it is assumed that the u-axis is perpendicular to the gravity vector, i.e. the telescope is parallel to Earth's surface, the image motion due to gravity can be calculated with the telescope elevation angle $\alpha$:

$$\phi_V \; [arcsec] \; = -2.107 \cos(\alpha) - 0.612 \sin(\alpha) \tag{3.24}$$

$$\phi_W \; [arcsec] \; = -0.061 \cos(\alpha) + 69.902 \sin(\alpha) \tag{3.25}$$

This corresponds to equation (3.22) and (3.23) for the load cases with 0 g in u-direction ($acc_U = 0$), 1 g cos($\alpha$) in v-direction ($acc_V = 1g \cos(\alpha)$) and 1 g sin($\alpha$) in negative w-direction ($acc_W = -1$ g sin($\alpha$)).

The FFI and WFI are mounted on the head ring of the metering structure and do not use the light beam coming through the main telescope optics. They are assumed to be rigid and the

rotational displacements of their mounting flange locations with respect to the gravity-free telescope are calculated with the finite element model. The results of the three load cases with 1 g acceleration applied along each telescope axis are listed in Table 3.3 [Süß 2004a]. Note, that the WFI and FFI in the technical note from Süß are swopped which could be clarified [Bremers 2005]. For a more detailed discussion and comparison on Finite Element Method (FEM) model predictions see [Meyer 2005].

**Table 3.3.**    Imager displacements in arcsec due to the three load case accelerations after [Süß 2004a].

**Load case 1g acceleration in u-direction**

|  | $rot(u_u)$ [arcsec] | $rot(v_u)$ [arcsec] | $rot(w_u)$ [arcsec] |
|---|---|---|---|
| WFI | -2.39 | -9.96 | 8.91 |
| FFI | 2.68 | -13.20 | -11.12 |

**Load case 1g acceleration in v-direction**

|  | $rot(u_v)$ [arcsec] | $rot(v_v)$ [arcsec] | $rot(w_v)$ [arcsec] |
|---|---|---|---|
| WFI | 6.66 | -2.83 | 70.13 |
| FFI | 6.91 | -3.09 | 70.75 |

**Load case 1g acceleration in w-direction**

|  | $rot(u_w)$ [arcsec] | $rot(v_w)$ [arcsec] | $rot(w_w)$ [arcsec] |
|---|---|---|---|
| WFI | 1.22 | 54.04 | 24.96 |
| FFI | 1.96 | 53.84 | -26.61 |

The displacements of the imagers about the indicated axes correspond to rotations about the telescope axes. Image motions within the imagers are in opposite direction. Regarding the image rotation about the LOS-axis, which is the w-axis for the WFI and FFI and the u-axis for the focal plane, the largest differential flexure occurs between the FFI and the focal plane. It is less than 1 arcmin (equivalent to 0.15 pixel at the edge of the chip) and can be neglegted.

The rotational displacements for both head ring imagers are calculated with the measured accelerations *acc* and the values for the calculated load cases from Table 3.3 by:

$$rot\ u_{XYI} = \frac{rot\ u_{u,XYI}}{g}acc_U + \frac{rot\ u_{v,XYI}}{g}acc_V + \frac{rot\ u_{w,XYI}}{g}acc_W \qquad (3.26)$$

$$rot\ v_{XYI} = \frac{rot\ v_{u,XYI}}{g}acc_U + \frac{rot\ v_{v,XYI}}{g}acc_V + \frac{rot\ v_{w,XYI}}{g}acc_W \qquad (3.27)$$
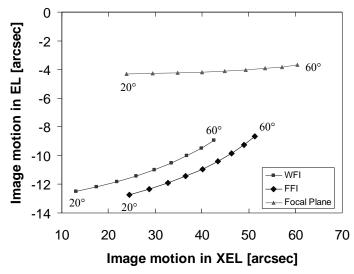
As before, it is assumed that the u-axis is perpendicular to the gravity vector, i.e. the telescope is parallel to Earth's surface, and the imager displacements due to gravity can be simplified using the telescope elevation angle α:

$$rot\ u_{\alpha,XYI} = \cos(\alpha)\ rot\ u_{v,XYI} + \sin(\alpha)\ (-rot\ u_{w,XYI}) \qquad (3.28)$$

$$rot\ v_{\alpha,XYI} = \cos(\alpha)\ rot\ v_{v,XYI} + \sin(\alpha)\ (-rot\ v_{w,XYI}) \qquad (3.29)$$

The corresponding load cases are with 0 g in u-direction ($acc_U = 0$), 1 g cos($\alpha$) in v-direction ($acc_V = 1g\ \cos(\alpha)$) and 1 g sin($\alpha$) in negative w-direction ($acc_W = -1\ g\ \sin(\alpha)$).
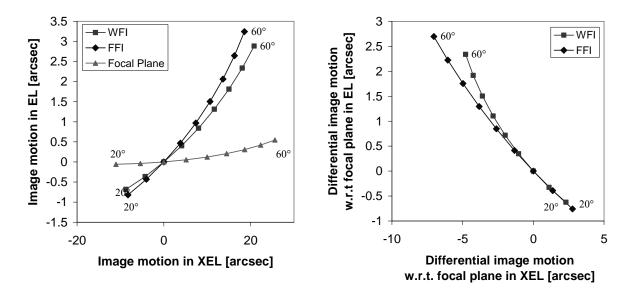
Figure 3.16 shows the FEM model predictions for the image motion due to gravity in the WFI and FFI (equations (3.28) and (3.29)) and at the focal plane (equations (3.24) and (3.25)) with respect to a gravity-free, rigid telescope. Each data point represents the image motion at an elevation angle between 20° and 60°. The gyroscopes that are mounted close to the bearing cannot sense the structural deformations and represent therefore the reference frame for the rigid telescope. If the gyroscope alignment measurements were repeated at the different elevation angles, the projected TARF origin would move along the predicted curve for the image motion at the focal plane (denoted by triangles). An alignment at 180° was assumed for the calculation of the three curves. The main image motion due to the 1 g acceleration occurs in XEL.



**Figure 3.16.** Image motion due to gravity in WFI, FFI and at the focal plane for elevations between 20° and 60° and for an optical alignment of the telescope at an elevation of 180° as predicted by the FEM model.

### 3.4.2 Combining alignment measurements with flexure compensation

During the alignment maneuvers, gravity is always acting on the telescope causing structural deformations and sensor displacements. Thus, the measured alignment matrices contain the pointing errors due to flexure at the elevation angle at which the maneuvers are performed. The FBC corrections are an option within the pointing control system and are only applied when it is activated. This includes the static part of the FBC which corresponds on ground the flexure due to gravity. Therefore, it is applicable to combine the sensor alignment with the flexure compensation, so that at a certain reference elevation – preferably in the middle of the elevation range – the sensors are aligned to the focal plane despite gravity is deforming the telescope structure. This elevation position would be ideally at an elevation of 40° or anywhere close where a suitable star for the alignment is available. If the FBC is turned off, the system is aligned with respect to this reference elevation and at other elevations only differential flexure affects the sensor alignment. In Figure 3.17, the predicted image motions in the WFI, the FFI and on the focal plane are shown on the left side with respect to the gravity-free telescope – or the gyroscope reference frame. These are the same deviations as in Figure 3.16, but this time, the boresight alignment between the imagers, the gyroscopes and the focal plane are performed at a reference elevation of 30°. The graph on the right side shows the resulting differential flexures of the head ring imagers with respect to the focal plane at elevations between 20° and 60°. If stars are consequentially imaged at different elevations and always brought to the center of the focal plane, the according centroid locations in the imagers would moves along these curves. At the elevation of 30°, the image motion is zero because all sensors are aligned to each other.



**Figure 3.17.** Image motion due to gravity in WFI, FFI and at the focal plane for elevations between 20° and 60° and for a boresight alignment at 30° elevation as predicted by the finite element model. The graph on the left side shows absolute image motions, the graph on the right side shows differential image motions with respect to the focal plane.

The alignment maneuvers that were presented in section 3.3 are summarized in Table 3.4 and brought into sequence. A short description of the alignment maneuvers is given along with the axis that will be aligned and the alignment matrix that will be calculated. In the last column, the provided matrices in the software are indicated that are part of these measurements. Repeating the sequence at different elevations reveals the flexure information.

**Table 3.4.** Summary of sequential alignment maneuvers and identified matrices.

| No. | Alignment maneuver description | Axis | Determined matrix | Provided matrices that are part of the determined matrix |
|-----|-------------------------------|------|-------------------|--------------------------------------------------------|
| 1 | Boresight definition in HIPO and imagers | LOS | XYIRF:TARF | XYIRF:XYIMFRF, XYIRF:TARF |
| 2 | Gyroscope alignment to HIPO | LOS | GYRF:TARF | GYRF:GYRF$_{initial}$, GYRF:TARF |
| 3 | Gyroscope alignment to HIPO after gyroscope LOS misalignment is compensated | EL/XEL | GYRF:TARF | GYRF:GYRF$_{initial}$, GYRF:TARF |
| 4 | Rotation of field alignment after gyroscope misalignment is compensated | EL/XEL | XYIRF:TARF | XYIRF:XYIMFRF, XYIRF:TARF |

The misalignment of the EL- and XEL-axes corresponds to a rotation of the field of view. Its influence on the image motion is negligible small over the elevation range. Thus, the alignment maneuvers need to be performed at various elevations only for the LOS-axis and the EL- and XEL-axes misalignment need to be measured only at the reference elevation. Furthermore, image motion in the WFI due to gravity can be neglected because of its pixel resolution. Over the whole elevation range, only one pixel image motion would occur in XEL with respect to the gravity-free telescope and only a third pixel with respect to the focal plane. Considering these assumptions, the number of alignment matrices that need to be identified is reduced. The remaining matrices are listed in Table 3.5. It is indicated which alignment maneuver from Table 3.4 has to be performed to measure the alignment matrices and which axes are aligned with it.

Implementing the FBC correction GYRF:TARF and imager flexure compensation matrices, must account for the boresight alignment at the reference elevation. This can be realized by recording the measured acceleration vector during the alignment at the reference elevation $el_0$ and subtracting the vector component wise from the measured acceleration that is used in equations (3.22), (3.23), (3.26) and (3.27) to calculate the flexure correction. Respectively the reference elevation $el_0$ is subtracted from the measured elevation value when using equations (3.24), (3.25), (3.28) and (3.29). As the sensor alignment takes place with respect to the focal plane, the matrices that compensate imager flexure must reflect the differential flexures between the imagers and the focal plane (corresponding to Figure 3.17, right side).

**Table 3.5.** Alignment and flexure compensation matrices that are determined at the reference elevation $el_0$ and over the elevation range as function of the elevation angle *el*.

| Alignment matrix in software | Alignment maneuver | Axes that are aligned within matrix | Dependencies |
|---|---|---|---|
| GYRF:GYRF$_{initial}$ | 2, 3 | EL/XEL/LOS at $el_0$ | - |
| FPIRF:FPIMFRF | 1, 4 | EL/XEL/LOS at $el_0$ | - |
| FFIRF:FFIMFRF | 1, 4 | EL/XEL/LOS at $el_0$ | - |
| WFIRF:WFIMFRF | 1, 4 | EL/XEL/LOS at $el_0$ | - |
| GYRF:TARF | 2 | LOS = f (el) | Low pass filtered accelerations |
| FPIMFRF:TARF | 1 | LOS = f (el) | Gravity vector |
| FFIMFRF:TARF | 1 | LOS = f (el) | Gravity vector |

Exemplarily, the image motion and its compensation are shown in Figure 3.18 for the focal plane and the FFI.
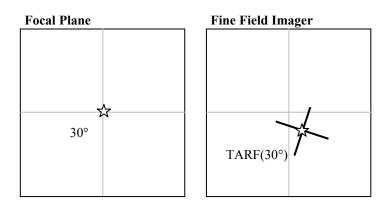
In step 1, the gyroscope and boresight alignment is performed at the reference elevation of 30°. A star is imaged at the center of the focal plane. Due to misalignment and flexure, the star is imaged in the FFI at a different location. The FFI alignment matrix reflects the measured misalignment by adjusting TARF with respect to the imager reference frame.

In step 2, the telescope moves to an elevation of 60° where a star is located exactly 30° apart in telescope elevation from the first star. Due to the flexure and associated image motion, the star is not imaged at the center of the focal plane but at an offset value. As well in the FFI, the star that would have been imaged at the TARF origin moved to an offset value due to the flexure.
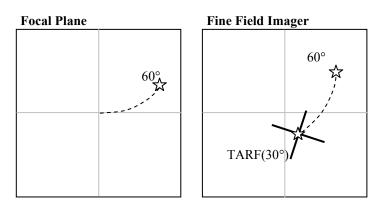
In step 3, FBC is activated and the image motion at the focal plane is compensated by adjusting the relation of GYRF:TARF. This causes the telescope to move but not to change the relation between TARF and IRF. The star is then imaged at the center of the focal plane. Due to the move, an according image motion can be seen in the FFI as well. As the orientation of TARF:IRF remains constant, the location of TARF on the imager field of view does not change. Due to the differential image motion between the imager and the focal plane, the telescope move due to FBC does not lead back to the TARF location in the FFI at 30°.

In step 4, the imager alignment matrix that compensates flexure is implemented. It manipulates the TARF location in the FFI such that it compensates for the differential flexure between the focal plane and the imager. The TARF location in the imagers is adjusted such that it reflects the location of the imaged star correctly.

1.) Gyroscope and boresight alignment at the reference elevation $el_0$=30°.



**Focal Plane**

30°

**Fine Field Imager**
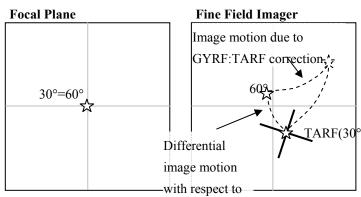
TARF(30°)
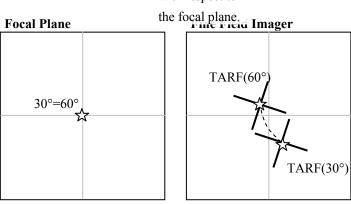
2.) After moving to an elevation of 60°, a star that would have been imaged at the boresight moved.



**Focal Plane**

60°

**Fine Field Imager**

60°

TARF(30°)

3.) At 60°, FBC is activated and the star is imaged again at the center of the focal plane. The correction causes a telescope move without changing the TARF location in the imager.



**Focal Plane**

30°=60°

**Fine Field Imager**

Image motion due to GYRF:TARF correction.

60°

TARF(30°)

Differential image motion with respect to the focal plane.

4.) The location of TARF in the FFI is adjusted by implementing the imager flexure correction.



**Focal Plane**

30°=60°

**Fine Field Imager**

TARF(60°)

TARF(30°)
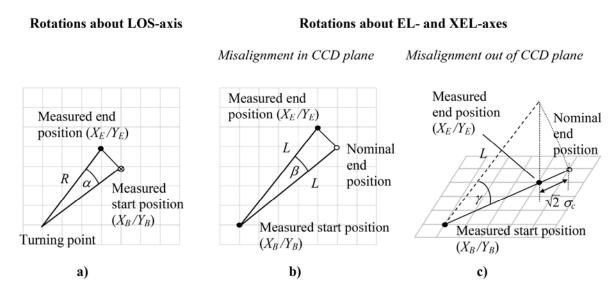
**Figure 3.18.** Image motion and compensation at the focal plane and in the fine field imager for an elevation at 30° and 60°.

## 3.5 Alignment accuracies

The alignment accuracies depend on the size of the commanded alignment maneuver and the centroid estimation error of the star images. The better the centroid position can be estimated and the larger the telescope motions are commanded during the alignment maneuvers, the better the alignment accuracies become. The centroid estimation error depends on the pixel size, the signal to noise ratio of the observed source and environmental conditions. The centroid error for both pixel coordinates *X* and *Y* are assumed to be random and uncorrelated. They are quantified with the standard deviation $\sigma_c$. In the following, the uncertainty propagation of the centroid estimation errors through the equations which determine the alignment angles is derived. Figure 3.19 summarizes the three different alignment angles that can be distinguished:

a)  For alignment maneuvers about the LOS axis, the angle *R* of the LOS axis.
b)  For alignment maneuvers about the EL and XEL axes, the angle *β* of the EL and XEL axes that lies within the CCD plane when the axes are projected on the focal plane.
c)  For alignment maneuvers about the EL and XEL axes, the angle *γ* of the EL and XEL axes that is perpendicular to the CCD plane when the axes are projected on the focal plane.



**Figure 3.19.** The three different alignment angles *R*, *β* und *γ*.

The alignment algorithms for these maneuvers are derived in section 3.3. The alignment angle *R* is calculated with equations (3.10), and the alignment angle *β* is calculated with equation (3.16). The alignment angle *γ* was disregarded as orthogonality is assumed. It is shown that the accuracy of the alignment angle *γ* is affected greatly by the centroid estimation error.

In general, if a quantity of interest $q$ can not be measured directly but as a function of the measurable quantities $q(x_1, x_2, ...)$, the measurement errors $\sigma_{X1}$, $\sigma_{X2}$, ... and their covariance $\sigma_{X1,2}$, ... of the directly measured quantities propagate through the corresponding function. The measurement uncertainty $\sigma_q$ of the function $q$ is given by:

$$\sigma_q = \sqrt{\left(\frac{\partial q}{\partial X_1}\sigma_{X,1}\right)^2 + \left(\frac{\partial q}{\partial X_2}\sigma_{X,2}\right)^2 + 2\sigma_{X1,2}\left(\frac{\partial q}{\partial X_1}\right)\left(\frac{\partial q}{\partial X_2}\right) + ...} \tag{3.30}$$

In the following, the measurement errors are assumed to be uncorrelated and equation (3.30) can be simplified with $\sigma_{X1,2} = 0$. The measurable quantities are the measured start and end positions of the centroid $X_B$, $Y_B$, $X_E$, $Y_E$. Their standard deviations are assumed to be equal: $\sigma_c = \sigma_{X,B} = \sigma_{Y,B} = \sigma_{X,E} = \sigma_{Y,E}$.

**a) Measurement error for misalignment angle R for LOS axis**

The standard deviation of $R$ can be calculated by equation (3.30) when substituting $q$ with $q=R\ (X_B, Y_B, X_E, Y_E)$:

$$\sigma_R = \sqrt{\left(\frac{\partial R}{\partial X_E}\sigma_c\right)^2 + \left(\frac{\partial R}{\partial X_B}\sigma_c\right)^2 + \left(\frac{\partial R}{\partial Y_E}\sigma_c\right)^2 + \left(\frac{\partial R}{\partial Y_B}\sigma_c\right)^2} \tag{3.31}$$

Using equation (3.10) for the calculation of the alignment angle $R$, the measurement error is given by:

$$\sigma_R = \frac{\sqrt{2}\ \sigma_c}{2\sin(\alpha/2)} \tag{3.32}$$

**b) Measurement error for misalignment angle β of EL/XEL axes in plane**

If the LOS axis is properly aligned and orthogonality is assumed, EL and XEL rotations about an angle $L$ result in a centroid displacement $L$ in the CCD plane. A misalignment of the EL axis, respectively XEL axis, causes a deviation of the measured end position from nominal end position. The misalignment angle lies within the CCD plane when the axes are projected on the CCD plane, see Figure 3.19b. Substituting $q$ in equation (3.30) with $q=\beta\ (X_E, X_B, Y_E, Y_B)$ and using equation (3.16) for $\beta$, the standard deviation of $\beta$ is given by:

$$\sigma_\beta = \frac{\sqrt{2}\ \sigma_c}{\sqrt{(X_E - X_B)^2 + (Y_E - Y_B)^2}} \tag{3.33}$$

When the LOS axis is aligned before the maneuver, then $L = \sqrt{(X_E - X_B)^2 + (Y_E - Y_B)^2}$ , and the error of $\beta$ is given by:

$$\sigma_\beta = \frac{\sqrt{2}\ \sigma_c}{L} \qquad (3.34)$$

**c) Measurement error for EL/XEL axes out of plane**

When the LOS axis is not aligned before the maneuver and/or orthogonality is not applicable, EL and XEL rotations about an angle $L$ can result in a centroid displacement smaller than $L$ in the CCD plane, see Figure 3.19c. Using the measurement technique presented, it is not possible to distinct in which direction the rotation axis is misaligned. The misaligned angle $\gamma$ can be calculated with:

$$\gamma = \pm \arccos\left(1 - \frac{\sqrt{(X_E - X_B)^2 + (Y_E - Y_B)^2}}{L}\right) \qquad (3.35)$$

Again, substituting $q$ in equation (3.30) with $q = \gamma\ (X_E,\ X_B,\ Y_E,\ Y_B)$ and assuming that $L - \sqrt{2}\ \sigma_c \approx \sqrt{(X_E - X_B)^2 + (Y_E - Y_B)^2}$ , the standard deviation of $\gamma$ is given by:

$$\sigma_\gamma = \sqrt{\frac{\sigma_c}{\sqrt{2}L - \sigma_c}} \qquad (3.36)$$

**Improvement of alignment accuracy by repeated measurements**

Repeating measurements several times decreases the error of the mean value of the measurements. When $\sigma_x$ is the standard deviation of a single measurement, the standard error of the mean $\sigma_{\bar{x}}$ for $n$ measurements is:
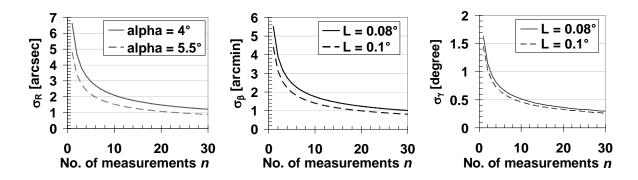
$$\sigma_{\bar{x}} = \frac{\sigma_x}{\sqrt{n}} \qquad (3.37)$$

Measurement repetition can have several meanings for the alignment angle accuracies:

1. Recording $n$ images before and after the alignment maneuver improves the accuracy of the centroid estimation error $\sigma_c$ by $1/\sqrt{n}$.

2. Repeating the alignment maneuvers $n$ times improves the accuracy of the alignment angle estimation error $\sigma_R$, $\sigma_\beta$ and $\sigma_\gamma$ by $1/\sqrt{n}$.

3. Evaluate $n$ stars in the field of view before and after the maneuver improves the accuracy of the alignment angle estimation error $\sigma_R$, $\sigma_\beta$ and $\sigma_\gamma$ by $1/\sqrt{n}$.

For improving $\sigma_R$ and $\sigma_\beta$, the different ways of measurement repetition have the same mathematical effect. This is due to the fact that the standard deviations are linearly depending on $\sigma_c$. This is not valid for $\sigma_\gamma$ but also not discussed in more detail as the alignment maneuvers regarding $\gamma$ are not applicable. In theory, recording 5 images of the star before and after the maneuver improves the accuracy in the same way as repeating the alignment maneuver 5 times or evaluating 5 stars within the same image. In practice, the different ways of measurement repetition can also eliminate systematic errors and reveal bad data.

Figure 3.20 shows how the estimation error of the alignment angles improves with increasing number of measurements. The standard deviations of all three alignment angles are shown for maneuvers with two different lengths. These are typical lengths for the alignment maneuvers with HIPO or the FPI.



**Figure 3.20.** Alignment accuracies depending on the number of measurements $n$ for alignment maneuvers with different lengths. The standard deviation for the centroid estimation is assumed to be $\sigma_c = 0.327$ arcsec which corresponds to 1 pixel in HIPO coordinates.

# 4 Inertial sensor data reduction techniques

The basic data reduction techniques that are employed to analyze the data of the inertial pointing control sensors are presented in this chapter. This includes the analysis techniques for the gyroscopes measurement of Earth's rotation rate when the SOFIA aircraft and telescope is on ground and stationary. However, the presented analysis techniques to characterize random noise errors can be applied in general for all types of measurements.

The expected results for the SOFIA gyroscopes are presented based on approximate values of manufacturer calibration measurements. The chapter explores as well the data reduction techniques for the astrometric measurements with the imagers and HIPO. The centroiding algorithms are discussed, as well as the effect of atmospheric refraction on the apparent star positions that are observed from ground. This is applied and studied when angular distances between stars are measured that extend over the telescope's elevation range.

## 4.1 Gyroscope measurements of Earth's rotation rate

When the telescope is on ground and no rotations are commanded, each gyroscope measures a component of Earth's rotation rate depending on latitude, heading and the CD elevation of the telescope. It is assumed that the telescope is centered within the bulkhead and the inner cradle and the telescope's EL axis is parallel to the aircraft's center line. Furthermore, the aircraft's centerline is assumed to be parallel to the local tangential surface of Earth's ellipsoid. The components that are measured by the EL, XEL and LOS gyro are then calculated theoretically by following equations:

$$\text{EL} \quad = \quad \Omega \, \cos(lat) \, \cos(h) \tag{4.1}$$

$$\text{XEL} \quad = \quad \Omega \, \cos(lat) \, \sin(h) \, \sin(el) \; - \; \Omega \, \sin(lat) \, \cos(el) \tag{4.2}$$

$$\text{LOS} \quad = \quad \Omega \, \cos(lat) \, \sin(h) \, \cos(el) \; + \; \Omega \, \sin(lat) \, \sin(el) \tag{4.3}$$

where *lat* is the latitude of the center of the telescope bearing, *h* is the heading of the aircraft and *el* is the telescope elevation. The absolute value of Earth's rotation rate is $\Omega = 15.0411°/h$.

## 4.2  Analysis techniques for gyroscope random noise characterization

Random noise processes can be characterized using statistical methods applied to the data in the frequency or time domain. The preferred means of analysis for random noise characterization of inertial sensors are the computation of the Power Spectral Density (PSD) in the frequency domain and the Allan Variance (AV) analysis in the time domain [IEEE 1998]. Both computation methods contain a complete description of the error sources. The PSD is better suited to analyze periodic or aperiodic signals, while random noise parameters are more difficult to identify. The AV analysis is an easier way to analyze and characterize the random noise and is usually used by sensor manufacturers to establish the performance specifications. Here, a short introduction is given to both analysis techniques and the according identification of noise sources.

### 4.2.1  Power spectral density

The PSD is a common tool to perform spectral analysis describing the power distribution of a signal with frequency. It reveals repetitive patterns and correlation structures within a signal process [Vaseghi 1996]. The unit is the squared signal unit per Hz.

Assuming a stationary process, the two-sided PSD is calculated as the Fourier transform of the autocorrelation function $K(\tau)$ with $\tau$ as correlation lag [IEEE 1998]:

$$S(f)_{two-sided} = \int\limits_{-\infty}^{\infty} e^{-i2\pi f\tau} K(\tau) \ d\tau \tag{4.4}$$

Because of the symmetry of $K(\tau)$ of many measurement signals, the term PSD can often be referred to the one-sided PSD whose amplitude is twice the two-sided PSD:

$$S(f) = S_{one-sided} = 2S_{two-sided} \tag{4.5}$$

In the following analyses, the PSD is always referred to the one-sided form.

### 4.2.2  Allan Variance analysis

The AV analysis is a data analysis technique in the time domain and is named after David Allan who originally developed it for analyzing phase and frequency stability of precision clocks and oscillators [Allan 1997]. The method has widely been adapted to characterize random drift of inertial sensors, especially gyroscopes.

In general, the AV is a method that represents the RMS standard deviation of the random noise as a function of averaging time. Although the AV is called a variance, it is usually referred to the standard deviation, thus root AV. Instead of computing the sampled mean and standard deviation from a measurement set leading to a conservative prediction of the sensor

performance, the two-sampled mean and standard deviation is computed to yield the AV. Plotting the AV over the averaging time, a characteristic curve is obtained that allows the identification and quantification of the noise sources. Furthermore, the AV plot gives a direct visual indication of the optimal sensor averaging time.

The AV for rotation rate data is computed as follows [Ng 1996]. The rate data sequence with $n$ samples is divided into $K$ clusters which each holds $m$ samples per cluster ($K=n/m$). Then, the average rate $\overline{\Omega}_k$ is computed for each cluster $k$ with:

$$\overline{\Omega}_k(m) = \frac{1}{m} \sum_{i=1}^{m} \Omega_{(k-1)m+i} \qquad k = 1, \dots, K \qquad (4.6)$$

where
| | | |
|---|---|---|
| $K$ | Number of clusters |
| $m$ | Number of samples per cluster ($K=n/m$) |
| $n$ | Number of samples |
| $\Omega_i$ | Rotation rate at sample $i$ |
| $\overline{\Omega}_k$ | Average rotation rate of cluster $k$ |

Having the rate data taken with a sample time interval $t_s$, the averaging time of a cluster becomes $\tau=mt_s$. Thus, the AV $\sigma^2_A$ associated with the cluster averaging time $\tau$ can be computed from the cluster averages $\overline{\Omega}_k$ with:

$$\sigma^2_{\Omega,A}(\tau) = \frac{1}{2} \left\langle \left( \overline{\Omega}_{k+1}(m) - \overline{\Omega}_k(m) \right)^2 \right\rangle$$
$$\cong \frac{1}{2(K-1)} \sum_{k=1}^{K-1} \left( \overline{\Omega}_{k+1}(m) - \overline{\Omega}_k(m) \right)^2 \qquad (4.7)$$

where
| | | |
|---|---|---|
| $t_s$ | Sample time |
| $\tau$ | Time of cluster ($\tau=mt_s$) |
| $\sigma^2_{\Omega,A}$ | AV of rotation rates |

The data processing flow is shown as a diagram in Figure 4.1. The data is divided into the clusters of length $\tau$ and the average $\overline{\Omega}_k$ of the rate data is computed in each bin. Then, the cluster averages of two successive bins are subtracted, and the variance of these differences is computed yielding one AV value associated with the cluster time $\tau$. In order to obtain a comprehensive AV curve over averaging time, the computation process has to be repeated with different values for the cluster time $\tau$. For a uniform spacing of the time values on the log-log plot, $\tau$ may be assigned to:

$$\tau = t_s \ m = t_s \ 2^j \qquad \text{with } j = 0, 1, \dots, j_{max} \qquad (4.8)$$

where $j$ are positive rational numbers and $j_{max}+1 \leq \log(n)/\log(2)$.

However, the values for the averaging time $\tau$, respectively the number of samples $m$ in a cluster, can be selected arbitrarily, depending on the desired resolution and range of the AV plot.

The AV $\sigma^2_{\theta,A}$ can be also computed with angular difference values. The relation to the AV $\sigma^2_{\Omega,A}$ of the rotation rates is:

$$\sigma^2_{\theta,A}(\tau) = \tau^2 \sigma^2_{\Omega,A}(\tau) \tag{4.9}$$
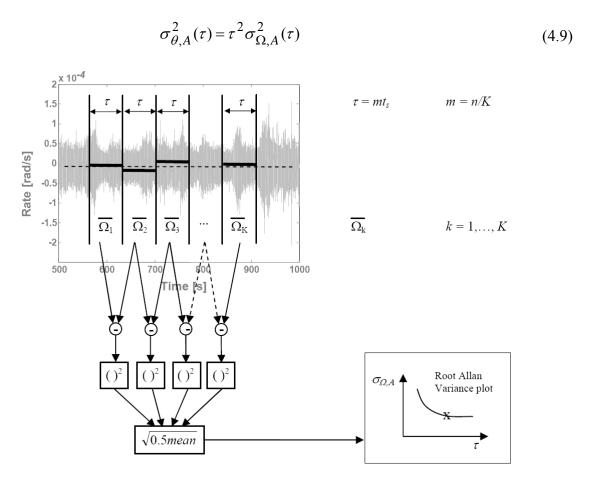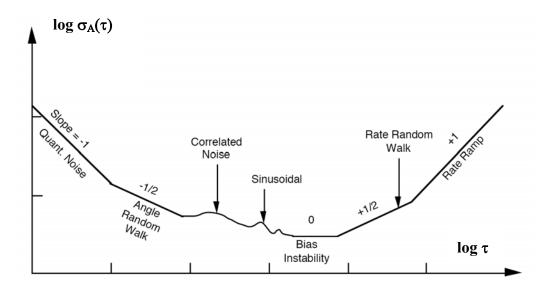


**Figure 4.1.** Allan Variance data processing flow diagram, after [Ng 1993].

### 4.2.3 Noise source identification

The different noise sources occurring in sensor signals can be identified by the slopes of the PSD and AV plots on a log-log scale. Each noise source has a certain character that can be associated with a slope. They dominate in a different frequency region, respectively averaging time region. In Figure 4.2, a sample plot of the root AV over the averaging time $\tau$ is shown, and the noise sources and corresponding slope values are indicated. The AV is expressed in the frequency domain through the following relation to the one-sided PSD [IEEE 1998]:

$$\sigma^2_{\Omega,A}(\tau) = 2 \cdot 4 \int_0^\infty S_\Omega(f) \frac{\sin^4(f\tau\pi)}{(f\tau\pi)^2} df \tag{4.10}$$

This builds the key to derive the relations of the noise characteristics and the AV. In the following, only the five, for the SOFIA gyroscopes relevant noise sources are listed with their formulations in the frequency and time domain. A complete derivation of the following relations and those of the other possible noise sources is given in reference [IEEE 1998].



**Figure 4.2.**    Sample plot of root Allan Variance analysis results [IEEE 1998].

**Quantization noise**

The rate PSD $S_{\Omega,Q}$ of the quantization noise can be expressed as:

$$S_{\Omega,Q}(f) = 2\frac{SF^2}{3t_s}\sin^2(f\pi\, t_s) \tag{4.11}$$

where the quantization interval is equal to the scale factor *SF*. For frequencies smaller than half of the sample rate, $S_{\Omega,Q}$ can be approximated with:

$$S_{\Omega,Q}(f) \approx \frac{\pi^2 SF^2 t_s}{3}\, f^2 \qquad\qquad \text{for } f < 0.5t_s \tag{4.12}$$

Thus, when plotted on a log-log scale, the PSD of the quantization noise is represented approximatley by the slope 2. Substituting equation (4.12) in (4.10) and performing the integration yields the root AV for the quantization noise:

$$\sigma_{\Omega,Q}(\tau) = \frac{SF}{2}\, \tau^{-1} \tag{4.13}$$

When plotted on a log-log scale, the root AV of the quantization noise has the slope -1.

**Angle random walk (ARW)**

The ARW is described by white noise on the rate signal. Consequently, the rate PSD $S_{\Omega,ARW}$ is flat over the whole frequency range. It is represented by a constant and is expressed in terms of the ARW coefficient $N$:

$$S_{\Omega,ARW}(f) = 2N^2 \qquad\qquad (4.14)$$

Note that the factor 2 is due to the one-sided PSD formulation.

The ARW is represented in the PSD plot with the slope 0. If the rate PSD is computed in units of $(°/h)^2/Hz$, the zero slope portion can be expressed in the more common unit for the ARW coefficient through:

$$N \;\left[°/\sqrt{h}\right] \;=\; \frac{1}{60}\sqrt{\frac{1}{2}S_\Omega\left[\;(°/h)^2/Hz\;\right]} \qquad\qquad (4.15)$$

Substituting equation (4.14) in (4.10) and performing the integration yields the root AV for the ARW:

$$\sigma_{\Omega,ARW}(\tau) = N\;\tau^{-0.5} \qquad\qquad (4.16)$$

When plotted on a log-log scale, the root AV of the ARW has the slope -0.5. Through a simple fit, the ARW coefficient $N$ can be determined.

**Bias instability**

The rate PSD of the bias instability or so-called 1/f-noise is expressed for frequencies smaller than the cut-off frequency $f_0$ with:

$$S_{\Omega,BI}(f) = \frac{B^2}{\pi\;f} \qquad\qquad f \le f_0 \qquad\qquad (4.17)$$

where $B$ is the bias instability coefficient and $f_0$ the 3-dB cut-off frequency. For $f > f_0$, the PSD is approximately zero. When plotted on a log-log scale, the PSD of the bias instability is represented by the slope -1. Substituting (4.17) in (4.10) and performing the integration yields the root AV for the bias instability:

$$\sigma_{\Omega,BI}(\tau) = \frac{B}{0.6648} \qquad\qquad \tau \gg 1/f_0 \qquad\qquad (4.18)$$

When plotted on a log-log scale, the root AV of the bias instability has the slope zero. The bias instability value can be read off the root AV plot at the flat region which has the lowest values of the curve.

**Rate Random Walk (RRW)**

The RRW is a result of integrated white noise. The rate PSD $S_{\Omega,ARW}$ is given by:

$$S_{\Omega,RRW}(f) = 2 \left( \frac{K}{2\pi f} \right)^2 \tag{4.19}$$

where $K$ is the RRW coefficient. When plotted on a log-log scale, the PSD of the RRW is represented by the slope -2.

Substituting equation (4.19) in (4.10) and performing the integration yields the root AV for the RRW:

$$\sigma_{\Omega,RRW}(\tau) = \frac{K}{\sqrt{3}} \; \tau^{0.5} \tag{4.20}$$

When plotted on a log-log scale, the root AV of the RRW has the slope 0.5.

**Rate ramp**

The rate ramp has the effect of a slow changing bias with time. It appears as input to the gyroscopes as $\Omega = Rt$ with $R$ as the rate ramp coefficient. The rate PSD associated with the rate ramp noise is given by:

$$S_{\Omega,ramp}(f) = 2 \frac{R^2}{(2\pi f)^3} \tag{4.21}$$

When plotted on a log-log scale, the PSD of the rate ramp is represented by the slope -3. The root AV of the rate ramp is computed with:

$$\sigma_{\Omega,ramp}(\tau) = \frac{R}{\sqrt{2}} \; \tau \tag{4.22}$$

When plotted on a log-log scale, the root AV of the rate ramp has the slope 1.

Table 4.1 summarizes the slope values for each of the individual noise sources in the PSD and AV plots.

**Table 4.1.** Summary of slope values for PSD and AV plots on log-log scale.

| Noise types | Rate PSD slope | AV slope |
|---|---|---|
| Quantization | 2 | -1 |
| ARW | 0 | -0.5 |
| Bias instability | -1 | 0 |
| RRW | -2 | 0.5 |
| Rate ramp | -3 | 1 |

**Composite of the noise sources**

Assuming that the random noise processes are statistically independent, the overall PSD can be composed of the PSDs of the individual noise sources by simply adding them up:

$$S_{total} = S_Q + S_{ARW} + S_{BI} + S_{RRW} + S_{Ramp} \qquad (4.23)$$

The total value for the AV is composed by the sum of the AV of the individual noise sources:

$$\sigma^2_{A,total} = \sigma^2_{A,Q} + \sigma^2_{A,ARW} + \sigma^2_{A,BI} + \sigma^2_{A,RRW} + \sigma^2_{A,Ramp} \qquad (4.24)$$

The composition of the individual noise sources and the identification process is illustrated in the following figures. The theoretical curves are shown as rate PSD plot in Figure 4.3 and as root AV plot in Figure 4.4. The figures provide an understanding of the AV technique and an approximate classification of the noise errors within these diagrams. The more extensive data analysis for each of the three SOFIA gyroscopes follows in chapter 5.

The curves are plotted in both graphs using equations (4.12) to (4.22) for the individual noise errors and equations (4.23) and (4.24) for the sum of the noise errors. The noise parameters that are exemplarily used for the computation of both plots are the specification values of the gyroscopes that are discussed in chapter 5.1. However, there are no specifications available for the RRW and rate ramp as the tracking system takes care of these noise sources. They contribute only at very small frequencies, respectively large averaging times, to the overall error. For demonstration purposes, approximate values for these noise parameters are taken that were determined for the gyroscopes, see section 5.1.

Plotting both diagrams on a log-log scale, the individual noise errors are represented by straight lines with characteristic slopes as listed in Table 4.1. The magnitudes of the noise coefficients obviously define with the location of these lines which noise processes are dominating in the data. The overall composite is shown as the thick solid curve. It overlies the lines of the individual noise errors in the area where they dominate. The noise errors clearly

dominate in different areas of frequencies in the rate PSD plot, respectively of averaging times for the root AV plot, allowing their identification and characterization.



**Figure 4.3.** Theoretical rate PSD composed from quantization noise, ARW, bias instability, RRW and rate ramp with a sample time of 0.0025 s.
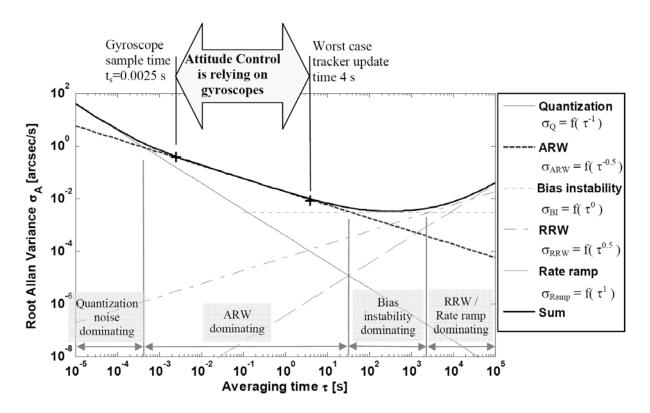
The rate PSD plot in Figure 4.3 is shown for frequencies from $10^{-6}$ to 200 Hz. The upper limit is determined by half of the sampling frequency which is used for calculating the curve of the quantization noise. The lower limit is set to such a low frequency that the area dominated by the rate ramp is visible in the graph. In practice, it is quiet difficult to get an accurate result of the PSD at such low frequencies where parameters of the estimation method have great influence on the PSD shape.

Regarding the sum of the noise errors in the PSD plot, the quantization noise has almost no influence. The ARW, the flat part of the curve, is dominating clearly above $10^{-2}$ Hz. The bias instability forms the transition of the composite curve into the RRW dominated area below $10^{-4}$ Hz. The composite finally merges into the line of the rate ramp at about $10^{-6}$ Hz.

The root AV in Figure 4.4 is computed for averaging times from $10^{-5}$ to $10^{5}$ s. Within this range, all of the noise parameters appear in the graph and contribute noticeably to the sum. The curves solely depend on the noise parameters. If real data are processed, the sampling time determines the smallest possible averaging time on the AV graph. The larger the averaging time gets, the more data samples are needed to receive accurate results, similar to the PSD plot.

**Figure 4.4.** Theoretical Allan Variance composed from quantization noise, ARW, bias instability, RRW and rate ramp for the SOFIA gyroscopes.

Regarding the sum of the noise errors in the root AV plot, the quantization noise dominates for very small averaging times. The sampling time has to be less than a millisecond in order that the quantization affects noticeably the overall error. The ARW dominates in the largest area of the graph from milliseconds to seconds. The bias instability adjoins as the flat part of the curve and dominates from seconds to 1000 s. It is not plotted that the bias instability decreases rapidly below the inverse cut-off frequency (here: 0.1 s). But it is also not relevant for the overall error and noise identification. Apart from 1000 s, the RRW shapes the curve of the noise composite until it merges into the line of the rate ramp which dominates for averaging times greater than 10 hours (36000 s). In these areas, the noise affects the data only in a deterministic way and the data signal changes very slowly.

Two explicit points are marked in the plot. The sampling time of the SOFIA gyroscopes at $\tau = 0.0025$ s determines the smallest possible averaging time. The second mark at $\tau = 4$ s represents the specified value for the largest time interval within which the tracker needs to deliver correction updates. In worst case, the attitude control relies on the gyroscopes as feedback sensors and thus on the noise errors in the area between these two marks. In this area only the ARW is the dominating noise process, flattened out by the bias instability or RRW.

The root AV plot is usually used by the manufacturers to identify and quantify the noise sources present in real data. It is better suited to assess the bias stability than the PSD technique. The standard definition of the bias stability by gyroscope manufacturers is the

minimum point of the root AV curve. The value represents the best stability that can be achieved with a fully modelled sensor and active bias estimation.

### 4.2.4   Allan Variance accuracies
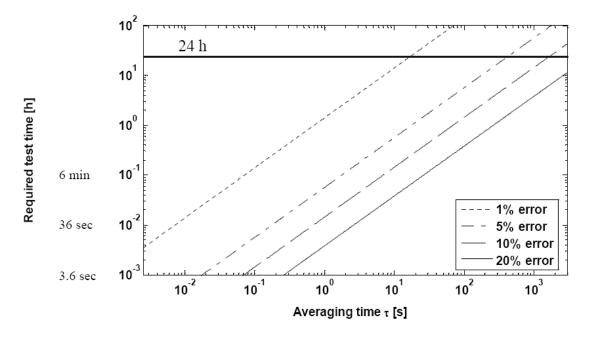
The accuracy of the estimated AV increases with the number of clusters used to compute the AV for the duration of the cluster time. The accuracy ($1\sigma$) of the AV computation for $K$ clusters is given by [Ng 1996]:

$$error = \frac{1}{\sqrt{2(K-1)}}$$
(4.25)

Note that if the number of clusters averages exceeds 200, the error becomes smaller than 5 %. Using this relation, the required test time $T$ can be determined for observing a certain noise characteristic with an averaging time $\tau$ within a given accuracy ($1\sigma$):

$$T = \tau \left( 1 + \frac{1}{2\ error^2} \right)$$
(4.26)

In Figure 4.5, the required test times are shown for averaging times between 0.0025 s and 3000 s to yield $1\sigma$-accuracies for the root AV of 1%, 5%, 10% and 20%. Even with a test duration of 24 h which is standard with gyro manufacturers, the accuracy that can be yield for the RRW with an charaterisctic averaging time over 3000 s is only about 20%.



**Figure 4.5.**   Required test time to observe a particular noise characteristic with averaging time $\tau$ within a given accuracy ($1\sigma$) of 1%, 5%, 10% or 20%.

### 4.2.5   Effect of sampling rate on angular random walk coefficient

When using housekeeping data of the TA system, it is possible that the gyroscope data are recorded with a lower sampling rate than their actual read-out rate. The recorded data is not filtered or an average of the read-out data. The PSD and AV values calculated from the recorded data are then higher than those calculated with the original read-out data and need to be corrected. In the following, the derivation of the correction terms is limited to the angular random walk.

The corrected ARW coefficient $N_{corrected}$ can be derived from equation (4.16):

$$N_{corrected} = N_{sampled} \sqrt{\frac{f_{sampled}}{f_{read-out}}} \qquad (4.27)$$

where $N_{sampled}$ is the ARW coefficient calculated with the data sampled with the sampling rate $f_{sampled}$. The read-out rate of the gyroscopes is $f_{read-out}$.

The corrected AV $\sigma_{ARW,corrected}$ is calculated with:

$$\sigma_{ARW,corrected} = \sigma_{ARW,sampled} \sqrt{f_{sampled}} \qquad (4.28)$$

The corrected PSD $S_{ARW,corrected}$ is calculated with:

$$S_{ARWcorrected} = S_{ARW,sampled} f_{sampled} \qquad (4.29)$$

## 4.3   Astrometric measurements

### 4.3.1   Centroiding algorithms

The image data reduction that is performed within this work is only concerned with the centroid calculation of imaged stars. The TA software performs the centroid calculation of target stars in the imagers when an area of interest is defined around them. The centroid positions are available within the TA housekeeping data and are already corrected for distortion of the camera optics [Lattner 2000]. The image processing and centroiding algorithms used within SOFIA's tracker system are described in [Schmolke 2001a, Levin 2008]. A short description of the basic algorithm functionality is given in the following paragraph. The algorithm is based on the "center of mass" algorithm which weighs the measured intensities $I(X,Y)$ by pixel coordinates $(X,Y)$ in the selected area. Threshold limits can be set to eliminate background noise and a constant background $B$ is subtracted.

The marginal distributions of the selected area are given for the row coordinates *X* by [Stone 1989]:

$$M(X) = \sum_{Y}\left(I(X,Y) - B\right)$$

(4.30)

Then, the centroid position $X_C$ equals the first moment of the marginal distributions:

$$X_c = \frac{\sum\limits_{X} X \cdot M(X)}{\sum\limits_{X} M(X)}$$

(4.31)

The calculation for the *Y* coordinate is performed completely analogue.
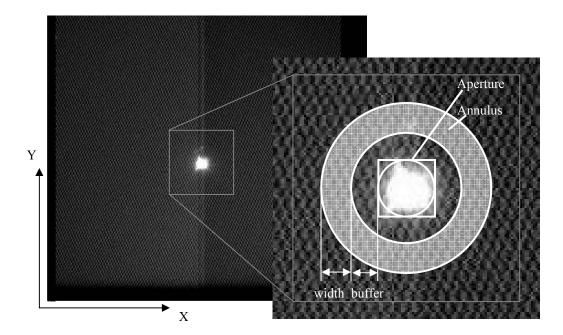
The HIPO images are recorded and reduced separately. Diverse centroiding algorithms are exemplarily tested using the images recorded during the on sky tests in 2004. The images were imported into analysis software and evaluated. A raw sample image is shown in Figure 4.6. Polaris is the imaged star at the center. Using the backup secondary mirror, a star image in HIPO is influenced by various aberrations resulting in an image with a two peak feature [Dunham 2004c]. For the alignment measurements, the data evaluation of the centroids was carried out using the quick look analysis tool for photometry of the software package IRAF (Image Reduction and Analysis Facility). The algorithm computes an initial guess of the centroid location based on the center of mass algorithm described above. The background radiation is subtracted by calculating the median of an annulus defined by the parameters buffer and width. The inner edge of the annulus is separated from the object aperture by the buffer distance and the outer edge is defined by the width for the annulus (Figure 4.6). Finally, a Moffat profile is fit to the radius and flux values of the background subtracted pixels to determine the peak intensity and the according centroid pixel locations [IRAF 1996]. A Gaussian profile is available as well.

For alignment measurements where centroid locations are compared after moves or between imagers, it is useful to apply the same algorithm to all images. Then, systematic errors due to the calculation method might be less significant. Although the tracking software uses the center of mass algorithm for centroid calculation, the HIPO images were reduced using the curve fitting algorithm. The parameter set for the Moffat type curve fit had an aperture radius of 5 pixels and for background subtraction a buffer of 5 pixels and an annulus width of 5 pixels.

The analysis software requires an initial position as user input close to the intensity peak of interest before it calculates the centroid positions. Three different algorithms were applied to the image in Figure 4.6 and the results are shown in Figure 4.7. The enlarged star image is shown with the calculated centroid positions. A three-dimensional representation of the image

detail is shown on the right side. The double peak feature can be clearly seen in both representations. The four applied algorithm combinations are:
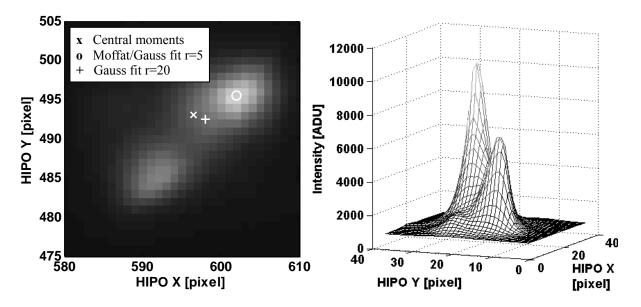
IRAF Moffat algorithm (used for the alignment evaluation in section 6) with r=5 pixels
IRAF Gauss algorithm with r=5 pixels and r=20 pixels
IRAF center of mass algorithm, selected box width is 40x40 pixels.



**Figure 4.6.** Raw HIPO image with Polaris imaged at the center of the CCD along with the pixel coordinate definition *X* and *Y*. The zoom- in section on the right shows the aperture radius and the white box which encloses the pixels that are used for the centroid calculation. The background level is calculated within the defined annulus.

The center of mass algorithm produces a centroid location in the center of the two peaks as its location is intensity weighted for a box of 40x40 pixels. Although the result lies not on one of the intensity peaks of the star image, it represents well the center of the light distribution of the distorted image. The results show that the curve fit algorithm yields very similar results for setting the curve fit type to either Moffat or Gauss. The curve fit with the smaller radius of 5 pixels yields a centroid location on the higher peak, if the initial position is selected close to it. The curve fit with the larger radius of 20 pixels includes also pixel from the second peak and yields a centroid location between them. An additional analysis of an image sequence confirmed that the relative positions between the centroid locations calculated with the different algorithms are not changing [Harms 2005a].

Using IRAF, the centroid calculation can be automated when a large number of images is evaluated. The initial centroid position, which was selected manually above, can be found using a special subroutine. It estimates the initial coordinates which then can be input to the centroiding algorithm routine [Massey 1992].

**Figure 4.7.** Section of imaged star with double peak feature. Left side: Image in 2D representation and absolute centroid values of different centroid algorithms. Right side: Image in 3D representation.

### 4.3.2 Effect of atmospheric refraction on star positions

Since the light is refracted by the atmosphere, the direction of a star differs from the true direction by an amount depending on the atmospheric conditions along the line of sight, i.e. atmospheric temperature, pressure and humidity, and the wavelength itself. The position of the observed star appears due to refraction always closer to the zenith, see Figure 4.8, and altitude is always increased. Refraction does not influence the position of stars at the zenith and has the biggest effect on the apparent position of stars at the horizon.
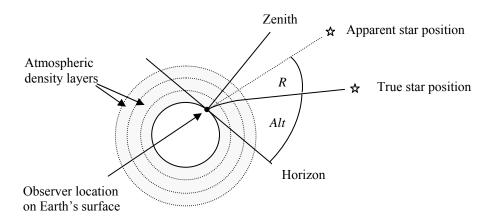


**Figure 4.8.** Refraction in Earth's atmosphere, after [Bely 2003].

There are several models describing the theory of atmospheric refraction. Evaluating telescope tests in regard to absolute pointing, an accuracy of a few arcsec is sufficient and

simplified refraction models can be used for the data analysis. This is especially true for star observations far above the horizon in the elevation range of the SOFIA telescope. In the following analysis, several models are compared and the influence of environmental conditions on the refraction angle is analyzed. The models are listed in Table 4.2 along with the valid altitude range and the basic atmosphere model.

**Table 4.2.**    List of authors and their models.

| Author, Year | Altitude requirement | Atmosphere model |
|---|---|---|
| Allen, 2000 | > 10° | Plane |
| Bely, 2003 | | Plane |
| Filippenko, 1982 | | Plane |
| Karttunen et al., 2003 | > 15° | Plane |
| Kovalevsky, 2002 | > 20° | Spherical |
| Stone, 1996 | > 15° | Spherical |

The refraction angle $R$ is defined as the difference between the true and the apparent zenith distance and can be approximated for a plane atmospheric model with [Allen 2000]:

$$R = \frac{n_0^2 - 1}{2n_0^2} \tan(90° - Alt)$$

(4.32)

The true zenith distance is the complementary angle of the star's altitude $Alt$ and the refractive index of dry air $n_0$ is given for a wavelength $\lambda_0 = 550$ nm at pressure $p_0 = 101325.2$ Pa and temperature $T_0 = 273.15$ K by $n_0 = 1.0002927$.

Assuming a spherical atmospheric model, the refraction angle is given by [Stone 1996]:

$$R = \kappa(n_0 - 1)(1 - \beta)\tan(90° - Alt) - \kappa(n_0 - 1)(\beta - (n_0 - 1)/2)\tan^3(90° - Alt)$$

(4.33)

The parameter $\kappa$ includes the apparent form of the Earth's geoid and is defined as the ratio of the gravity $g_0$ at the observing site to the sea-level gravity $g$ at the Earth's equator:
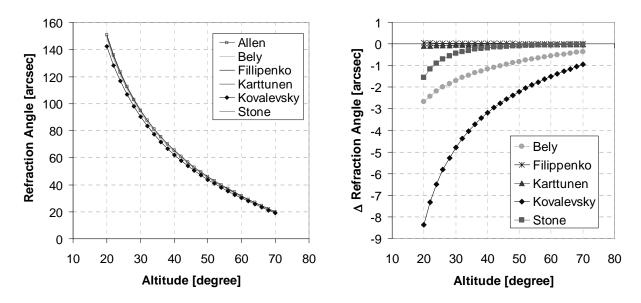
$$\kappa = g_0 / g$$

(4.34)

When $t$ is the air temperature in °C, the parameter $\beta$ is defined as:

$$\beta = 0.001254 \left( \frac{273.15 + t}{273.15} \right)$$

(4.35)

As mentioned, the index of refraction $n_0$ is depending on the wavelength and metrological data such as the air pressure, the temperature and the humidity of the air. It is the main
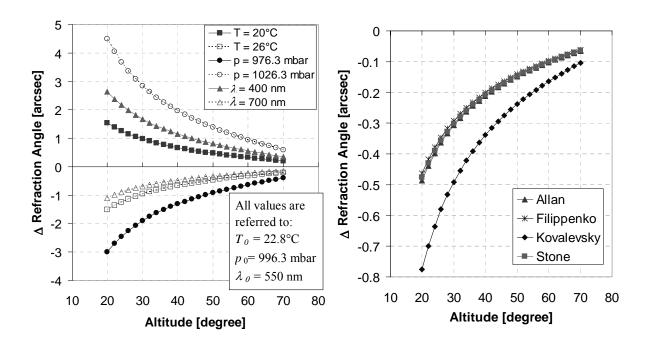
difference in the models. For detailed calculation formulas, it is referred to the authors listed in Table 4.2. Figure 4.9, left side, presents their results as refraction angle for dry air depending on the altitude position of the observed star. As reference condition, the ambient temperature was assumed to $T = 22.8°\,C$, pressure $p = 996.3$ mbar and the average wavelength $\lambda = 550$ nm. Already just for dry air, the formulas yield results that vary within 10 arcsec. In Figure 4.9, right side, the difference of the various refraction angles to a reference, the values of Allen's formula, are displayed.



**Figure 4.9.**  Left side: Refraction angles for dry air using different refraction models.
Right side: Comparing different refraction models. The refraction angles are referred to the results from [Allen 2000] for dry air.

The influence of temperature, pressure and wavelength variations on the refraction angles are studied with Stone's model and the results are shown in Figure 4.10, left side. Each curve represents the variation of one of the variables and is referred to the amount of refraction of the above mentioned values $T_0 = 22.8°C$, $p_0 = 996.3$ mbar and $\lambda_0 = 550$ nm. The lower the altitude of the star is, the larger the influence of the variation gets. For example when observing a star at an altitude of 20°, a temperature variation of 3°C affects the refraction by 1.5 arcsec; an unusual high pressure fluctuation of 30 mbar affects the amount of refraction by 4.5 arcsec.
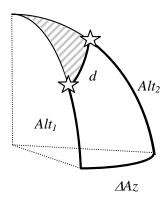
For visual wavelengths, the relative humidity has only a small effect on the refraction. The index of refraction of air - hence the refraction angle - decreases for moist air. The difference of the refraction angle of moist air to dry air is shown for the different models in Figure 4.10, right side. The curves are calculated with a relative humidity of 74% which represents a typical value for the later analyzed observations in Waco, TX. The relative humidity changes the refraction angle less than 1 arcsec over the telescope elevation range. Bely's model is not shown as it differs largely from the others. Stone's model was selected for further analysis due to its verification with empirical observations and its agreement with the other models.

**Figure 4.10.** Left side: Pressure, temperature and wavelength dependence on refraction angle of dry air. Right side: Influence of relative humidity (74%) in air on refraction angle, referred to the values for dry air.

### 4.3.3 Angular distances between stars

The astrometric positions of stars can be described in spherical coordinates: the equatorial or horizontal coordinates (Appendix C.4). The angular distances between the stars are then calculated using spherical trigonometry. Figure 4.11 illustrates the calculation. The angular distance $d$ of two stars with horizontal coordinates Altitude *Alt* and Azimuth *Az* is the side length of the spherical triangle having the stripe pattern. Using the law of cosine, the cosine of the angular distance $d$ is given by:



**Figure 4.11.** Calculating the angular distance $d$ between two stars with coordinates Azimuth *Az* and Altitude *Alt*.

$$\cos(d) = \cos(\Delta Az)\sin(90° - Alt_1)\sin(90° - Alt_2) + \cos(90° - Alt_1)\cos(90° - Alt_2) \qquad (4.36)$$

where $\Delta Az$ is the difference of the Azimuth coordinates of the stars and $Alt_1$, $Alt_2$ are the Altitude coordinates. Equation (4.36) can be simplified to:

$$\cos(d) = \cos(\Delta Az)\cos(Alt_1)\cos(Alt_2) + \sin(Alt_1)\sin(Alt_2) \qquad (4.37)$$

If the stars are observed with the TA and the orientation of the TA is known during the observations, the angular distance can be calculated as well from the TA housekeeping data. The calculation is illustrated in Figure 4.12. The orientation of the TA while observing the two stars is given by the quaternion $q_1$ representing TARF$_1$, and respectively $q_2$ representing TARF$_2$ with respect to the inertial reference frame. The attitude difference between $q_1$ and $q_2$ is given by equation (B.26) in Appendix B and contains the information about the angular distances between the stars. The attitude difference is then expressed by Euler Angles using the rotation sequence EL, XEL and LOS using equations (B.11), (B.12) and (B.13) in Appendix B.
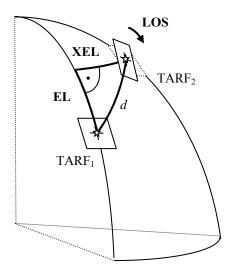


**Figure 4.12.** Calculating the angular distance of two stars using the TA coordinates *EL* and *XEL*.

As the rotation of the field is not relevant for calculating the angular distance of the stars, the LOS component being the last rotation in the sequence can be omitted. The angular distance is then given by the law of cosine for a rectangular spherical triangle with:

$$\cos(d) = \cos(EL)\cos(XEL) \tag{4.38}$$

# 5   Analysis of gyroscope performance measurements and system effects

In this chapter, the performance of the three gyroscopes are characterized by means of measurement data. The first section focuses on the measurements data taken during calibration measurements from the manufacturer. The initial performance measurements were repeated years later after replacing a part of the gyroscope electronics. Therefore, two calibration data sets are available. The measurement data is primarily used to identify and quantify the noise that is present in the gyroscope data. The second section describes the gyroscope performance measurements after the three gyroscopes were integrated into the TA system. Various system effects caused by other TA subsystems, aircraft systems or ground support equipment are seen in the gyroscope data along with the sensor noise. These effects are characterized depending on their cause and the specific TA operation mode.

## 5.1   FOG noise analysis prior to integration

The gyroscope performance and calibration measurements were performed on an isolated rate table where the applied rotation rate and position of the sensors relative to a reference are well known. Aditionally, a temperature chamber was used for calibrating temperature dependencies. As mentioned, there are two calibration data sets that are analyzed in this section. Both sets were taken by the manufacturer IXSEA. The first set was taken before the FOGs were delivered for integration 1999 [Faussot 1999] (gyro 1), respectively after a repair in 2003 [Ly 2003a-b] (gyros 2, 3). The second set was taken years later after some modifications and an electronic power board replacement in 2008 [Sergeant 2008a-c] (gyros 1, 2, 3).

The FOGs are characterized by estimating the stability parameters from the calibration data using the Allan Variance technique, as described in detail in section 4.2. As only the root AV curves are available in their measurement reports, the listed data points of the root AV curve are taken to retrace their noise parameter derivation and to estimate additional noise parameters useful for filter design and system simulations.

The noise sources can be identified by the slopes of the root AV plot. As explained in section 4.2, there are five different noise processes likely to occur. Each process is associated

with a characteristic slope and dominates in areas with different averaging times. The available measurement data is used to quantify these processes. The slopes of the individual noise processes, respectively their composite, are fitted to the measured root AV data.
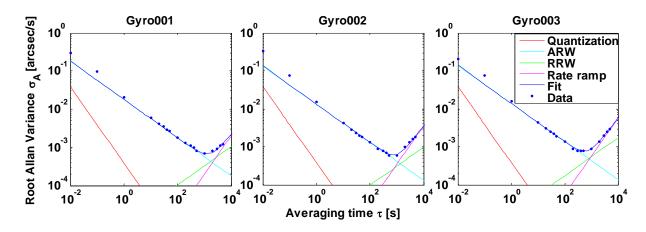
The root AV of the initial calibration data set is shown in Figure 5.1 along with the fitted slopes of four noise processes and their composite fit. The same technique was applied to the second data set which is shown in Figure 5.2 along with the noise process fits and their composite fit.

Based on the theoretically derived root AV curve in Figure 4.4, following conclusions can be drawn for each of the noise processes:
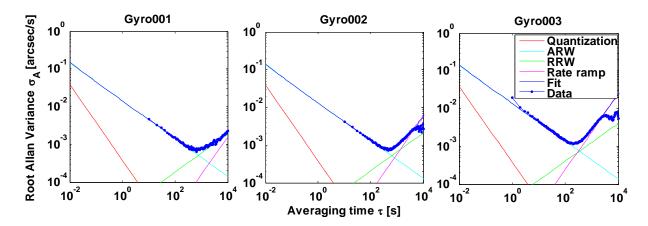
- The quantization noise is not visible in the AV curve for averaging times smaller than 0.001 s. Its noise process is well defined by the quantization interval which is the measured angular increment (0.000767 arcsec).

- The ARW is dominating in the largest area of considered averaging times. As stated in the measurement reports, the ARW can be fitted to the data between 1 s and 500 s (300 s for Gyro 003). The deviation of the 0.1 s and 0.01 s data points from the ARW slope is explained by limitations of the test equipment, as these measurements are very sensitive to vibrations. The data set from 2008 does not include averaging times smaller than 1 s.

- In both data sets, the root AV curve does not show a pronounced plateau as the minimum of the curve. The bias instability cannot be quantified as a dominating noise process. It is assumed to be smaller that the other noise processes overlaying the bias instability effect on the overall curve.

- The RRW and the rate ramp can be identified in the data and lead to the increase of the AV towards larger averaging times. The according noise process slopes can be fitted in such a way that the composite of RRW and rate ramp match the measured AV data for averaging time greater than 500 s (300 s for Gyro 003). The noise parameters for the RRW and rate ramp are not specified directly as values rather than indirectly by the in-run bias stability value. The in-run bias stability value is defined indirectly as the minimum point of the root AV curve.

The noise parameters that produce the root AV curve fits are shown in Table 5.1. Over the course of 5 years, for the Gyro 001 even 9 years, the ARW coefficient did not change significantly. On the contrary, the RRW coefficient doubled and the rate ramp increased which can be also related to less stable environmental test conditions. These results lead to higher in-run bias stability values.

The specification values for the ARW and the in-run bias stability are shown with the measured AV data for the initial calibration measurements in Figure 5.3 and for the recent calibration measurements in Figure 5.4. Note that the in-run bias stability is a parameter to describe the best stability that can be achieved with all noise sources present. It is not to be confused with the term bias instability which is a single noise process. The FOGs fulfill the specifications regarding ARW and the in-run bias stability. The $1\sigma$ error of the AV data is specified by equation (4.25) and depends on the total test length.
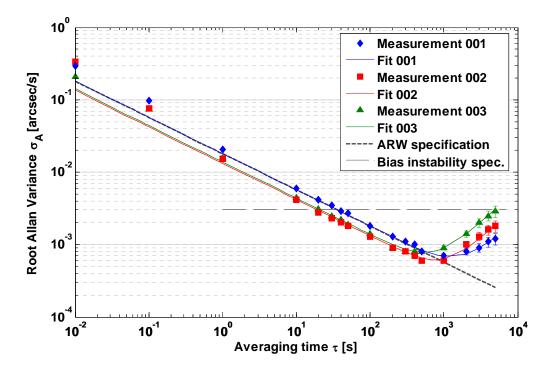
**Figure 5.1.** Root Allan Variance of the initial manufacturer measurements in 1999/2003 with fits of the four identified noise processes.
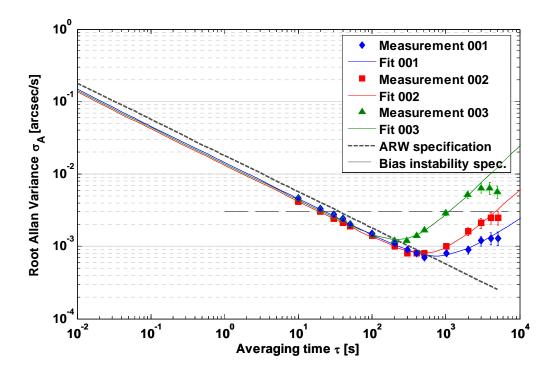


**Figure 5.2.** Root Allan Variance of the recently repeated manufacturer measurements in 2008 with fits of the four identified noise processes.

**Table 5.1.** Noise parameters derived by curve fitting of manufacturer measurements.

| Noise parameters | Unit | Specification | Gyro 001 | | Gyro 002 | | Gyro 003 | |
|---|---|---|---|---|---|---|---|---|
| Measurement year | | | 1999 | 2008 | 2003 | 2008 | 2003 | 2008 |
| Test length | h | | 24 | 18 | 24 | 19 | 24 | 15 |
| ARW coefficient $N$ | $°/\sqrt{h}$ | 0.0003 | 0.0003 | 0.00024 | 0.00022 | 0.00022 | 0.00023 | 0.00023 |
| RRW coefficient $K$ | $°/h^{3/2}$ | n/a | 0.0648 | 0.1152 | 0.0612 | 0.1296 | 0.0144 | 0.252 |
| Rate ramp coefficient $R$ | $°/h^2$ | n/a | 0.00102 | 0.0008 | 0.00178 | 0.00288 | 0.00204 | 0.01224 |
| In-run bias stability | $°/h$ | 0.003 | 0.0007 | 0.0007 | 0.0006 | 0.0007 | 0.0008 | 0.0011 |
| at averaging time | s | n/a | 1000 s | 700 s | 700 s | 500 s | 500 s | 200 s |

**Figure 5.3.** Comparing the root Allan Variance of the initial manufacturer measurements in 1999/2003 with the noise specifications.



**Figure 5.4.** Comparing the root Allan Variance of the recently repeated manufacturer measurements in 2008 with the noise specifications.

## 5.2 FOG noise analysis under various TA subsystem configurations

Between June 21st and 23rd 2007, a test series of stability measurements of the three fiber optic gyroscopes mounted on the SOFIA telescope was performed to assess their noise characteristics. There was a concern based on measurements taken during the on sky testing period in 2004 and during the preparation period for the aircraft ground vibration test in 2006 that the gyroscopes did not perform as well as specified and as initially measured by the manufacturer. The measurements taken in 2004 showed a much higher noise level than anticipated from the measurements of the manufacturer. It was not clear if these high noise levels were caused by the noisy environment (air-conditioning, fans, people in aircraft) or if the noise was caused by performance degradation of the gyroscopes themselves. Thus, the measurements were repeated with a quiet test environment and longer test duration in order to assess the sensor performance properly.

The performance measurements are ideally made on a rate table in a vibration-free and temperature controlled environment such as the calibration measurements described in section 5.1. Since it is not desired to demount the gyros for the stability measurements, the telescope system was configured in such a way that its own vibration isolation is most effectively used. To acquire knowledge about the influence of the different telescope operation modes on the sensor measurements, the test series consists out of four different tests in which the SUA is activated step by step to isolate vibrations.

The RIS activates the hydrostatic bearing and enables the operation of the FD. Once the FD brakes are released, the telescope is floating on the oil film around the bearing. The telescope is then protected from rotational vibrations, although vibration noise is added through the active oil return pumps.
The FD rotation is controlled either locally with the spherical sensors of the bearing or inertially with the gyroscopes as feedback sensors. If the control loop is closed, the sensor measurements include the behavior of the controller and the feedback sensors. This is also valid for the CD control, although it is assumed to have a negligible effect.
The VIS can be set to a caged mode, where the air springs are pressurized and centered tangentially, but pressed and clamped against hard stops in axial direction. Vibrations are isolated tangentially, but are still transmitted through the axial hard stops. Transitioning to the uncaged mode during flight, centers the VIS in all directions due to the pressure differential between the cabin and the cavity. To create a similar status on ground, the air springs in axial direction are evacuated moving the telescope away from the axial hard stops.
The possible subsystem modes of the RIS, the drives and the VIS are listed in Table 5.2. The effects of the nominal subsystem modes on the sensor data are added. The subsystem modes that are set during nominal operation are marked in bold.
The first test is conducted with the RIS shutdown. The second test case is conducted with the RIS active (TA floated) but FD braked and the VIS caged. The third test case is conducted

with the RIS active but FD braked and the VIS uncaged. The fourth test case is conducted with the RIS active, the FD brakes released and FD in open loop and the VIS uncaged.

**Table 5.2.** TA subsystem configurations and their effects on sensor data during nominal operation (in bold).

| TA subsystem configurations | Effect on sensor data during nominal operation |
|---|---|
| RIS: deactivated **activated** | Oil pump system noise |
| FD: braked **unbraked** | Vibrations isolated (RIS) |
| control loop open, TA balanced **control loop closed** | Control loop characteristics, influence of feedback sensors |
| CD: braked **unbraked, controlled** | Control loop characteristics |
| VIS*: caged **uncaged**** | Vibrations isolated (VIS) |

\*     *Depressurization of the VIS is neglected.*
\*\*    *VIS airsprings are evacuated to create uncaged status on ground.*

## 5.2.1   Test set up and procedure

**Aircraft and hangar conditions**

During the tests, the SOFIA aircraft was parked in the weight and balance hangar on Edwards AFB, CA. Detailed position and heading information was measured via GPS and can be found in the next section. Both hangar doors were shut and only minor noise sources in the hangar were present. Aircraft and ground support systems were turned off as far as possible but yet allowed power supply for the TA: the ground power supply unit and the transformer-rectifier unit on the aircraft were running. The ventilation fans in the cabin were turned off manually. Two cooling carts were operated only for those of the four Test Cases (TC) that required TA oil cooling. No parallel work in the aircraft was taking place and walking in the aircraft was avoided.

**TA subsystem configuration, test cases**

The telescope CD elevation was at 40.1077°. The telescope FD was centered within the inner cradle. The four different test cases with the telescope configuration are summarized below.

Test case TC-1:
- RIS is shutdown, telescope is not floated.
- VIS is caged.
- Long term test, 4 h

Test case TC-2:
- RIS is active, telescope is floated.
- FD brakes are closed.
- VIS is caged.
- Long term test, 4 h

Test case TC-3:
- RIS is active, telescope is floated.
- FD brakes are closed.
- VIS is uncaged (on ground: axial air springs are evacuated).
- Long term test, 4 h

Test case TC-4:
- RIS is active, telescope is floated.
- FD brakes are open; FD control is operated in open loop.
- VIS is uncaged (on ground: axial air springs are evacuated).
- Short term test, 25 min.

The length of the test determines the accuracy with which the AV and thus the stability parameters can be estimated. Here, the test length for the three long term tests was selected to be 4 h, refer to section 4.2.3 for further description. The detailed test plan and procedure can be found in [Harms 2007a].

## 5.2.2   Environmental and TA subsystem conditions

**GPS position and heading measurements**

Three position points on the centerline of the aircraft were measured with three different GPS receivers (Magellan, Mio and Nextel). Ensuring receiver reception, two position points were located outside the hangar; the third point was located about 80 m further outside the south east door. The three GPS measurements were averaged each and the heading was calculated by using the two most distant position points and applying spherical geometry. The results are listed in Table 5.3.

**Table 5.3.**    Position, heading and elevation measurements.
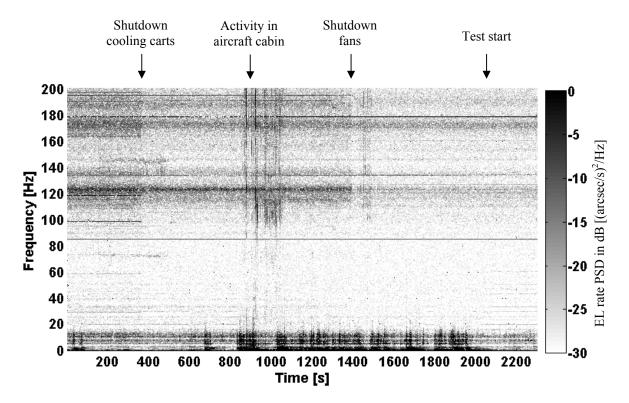
|  | GPS measurements | Other |
|---|---|---|
| Position bulkhead | N   34° 56.21'<br>W 117° 53.35' |  |
| True heading | 324° | 320° (cockpit compass reading: magnetic North, offset to true North about 13°E, assumed to be inaccurate inside hangar, due to local magnetic fields) |
| Altitude | 697 m | 699 m (airport map) |

**Aircraft and ground support system influence**

For conducting TC-1, the aircraft and ground support systems were (as mentioned) not needed and were shut down sequentially. During the test setup and shut down of the systems, data were recorded to investigate their influence on the gyroscope measurements. As an example, the spectrogram of the measured EL gyro rates is shown in Figure 5.5. The spectrogram is a graph which shows the time history of the PSD of a signal. For estimating the PSD, the short-time Fourier transform is used. While the two axes of the graph are time and frequency, the magnitude of the PSD is represented by gray colors. The magnitude is on a logarithmic scale in dB.

On the upper side of the figure, the time line of the shut down events is approximately indicated. When both cooling carts are shut down, a clear drop in noise over the measured frequency region is visible. The same is valid for higher frequencies during the shutdown of the ventilation fans. Calculating the PSDs before and after the shutdown events allows the identification of frequencies that are measured by the gyros due to the active system. The identified frequencies for the cooling carts and the ventilation fans in the aircraft are listed in Table 5.4. Note that the sampling frequency of the gyros is 400 Hz, thus identified frequencies could be alias frequencies.

While people were present in the aircraft and especially walking in the aircraft, a very high frequency content in the region below 20 Hz is noticeable. Once the stability measurement test was started and all activities on the aircraft were prevented, these low frequencies are not measured anymore. Thus, the very high noise figures that were measured during earlier tests (i.e. during the on sky test series in 2004) are most likely due to activities that took place on the aircraft at the same time.

**Figure 5.5.** Spectrogram of measured angular rate with the EL gyro during test setup. The PSD value is gray color coded and the frequency content is shown over time. The influence of the cooling carts, the aircraft fans and activity in the aircraft can be clearly seen.

**Table 5.4.** Major measured frequencies excited by cooling carts and aircraft fans. Note that the sampling frequency of the gyros is 400 Hz, thus identified frequencies could be alias frequencies.

| Frequencies excited by cooling carts [Hz] | | | Frequencies excited by aircraft fans [Hz] | | |
|---|---|---|---|---|---|
| EL | XEL | LOS | EL | XEL | LOS |
| 45.1 | | 45.1 | 71.9 | | 71.9 |
| 58.7 | 58.7 | 58.7 | | 95.0 | 95.0 |
| 73.1 | 73.1 | | 122.8 | 122.8 | 122.8 |
| 98.3 | 98.3 | 98.3 | 135.6 | | |
| 115.3 | 115.3 | 115.3 | | | 143.8 |
| 118.4 | 118.4 | 118.4 | | 146.1 | |
| | 120.0 | 120.0 | 190.0 | 190.1 | 190.0 |
| 163.3 | | 163.3 | 194.4 | 194.4 | 194.4 |
| 186.6 | | 186.6 | | | |
| 189.7 | | 189.7 | | | |
| 196.8 | 196.8 | 196.8 | | | |

**RIS influence**

Except for TC-1, the RIS was active and the oil pump system was running to enable the floating of the TA. The main oil pump is located in the forward lower lobe and is constantly active. Two return pumps are located directly on the rotating part of the telescope and are activated periodically. In the current configuration, one oil pump can be set to a high rate mode. Depending on the activation status of the pumps, certain frequencies are induced and measured by the gyroscopes. There are four activation combinations possible:

- Main pump on high rate
- Main pump on high rate and return pump 1 activated
- Main pump on high rate and return pump 2 activated
- Main pump on high rate, return pump 1 and 2 activated

The identified frequencies that are induced by the pump activation are listed in Table 5.5 depending on their activation status. Note that the sampling rate of the gyros is 400 Hz. Therefore, frequencies can be identified up to 200 Hz and the identified frequencies could be alias frequencies.

**Table 5.5.**    Induced frequencies by oil pump activation (only major frequencies mentioned).

| Oil pump status change | Measured frequencies [Hz] | | |
|---|---|---|---|
| | EL | XEL | LOS |
| Activating main pump | 30.0 | 30.0 | 30.0 |
| | 190.2 | 190.2 | |
| Activating return pump 1 | 11.7 | | |
| | 120.3 | 120.3 | 120.3 |
| | 139.9 | 139.9 | 139.9 |
| | | 159.9 | |
| | | 186.5 | 186.5 |
| Activating return pump 2 | | | 130.3 |
| | 170.5 | | 170.5 |
| | 175.2 | | 175.2 |
| | 190.2 | 190.2 | 190.2 |

**VIS position behavior**

For performing long term measurements and assessing long term noise parameters of the gyroscopes, a change of the VIS air spring positions can influence the measurements considerably. During the test series, the tangential VIS air springs were pressurized. For TC-3 and TC-4, the axial air springs were evacuated reproducing the uncaged mode on ground and disconnecting the telescope's outer cradle from the brackets mounted to the bulkhead. This allows better vibration isolation of the telescope from the aircraft. The positions of the VIS air springs are measured by seven sensors: three in axial direction and four in tangential direction. The time history plots of the VIS positions sensors for all four test cases are shown in [Harms 2007b]. In Table 5.6, the maximal deviation of the measured position values is listed for each sensor for all test cases. This reflects the difference between the position measured at test start and test end.

**Table 5.6.**     Maximal position deviation of VIS sensors measured during the four different test cases.
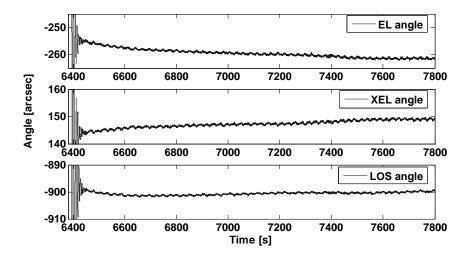
| VIS sensor | Maximal position deviation [mm] | | | |
|---|---|---|---|---|
| | TC-1 | TC-2 | TC-3 | TC-4 |
| VIS mode | caged | caged | uncaged, 4 h | uncaged, 25 min. |
| tg1 | 0.18 | 0.09 | 0.63 | 0.02 |
| tg2 | 0.06 | 0.03 | 0.20 | 0.02 |
| tg3 | 0.07 | 0.09 | 0.73 | 0.02 |
| tg4 | 0.05 | 0.03 | 0.08 | 0.02 |
| ax1 | 0.05 | 0.05 | 0.73 | 0.03 |
| ax2 | 0.05 | 0.04 | 1.79 | 0.03 |
| ax3 | 0.04 | 0.04 | 0.59 | 0.02 |

A drift in position can be observed, even for the caged test cases. Due to temperature effects, a large motion in all of the position sensors is seen during TC-3, the 4h long term test while the VIS was uncaged. The drift decreases during the course of the test. For the test evaluation of TC-3, only the data section is analyzed for which the position change is either negligible or linear.

**FD open loop conditions**

During TC-4, the FD brakes of the floating TA were released and the FD was operated in open loop. After the FD brakes were released, the telescope was oscillating until it settled to its balance position. Figure 5.6 shows the measured angles by the spherical sensors. Initially, the TA was centered within the inner cradle and settled then in its balance position at about -260 arcsec in EL, 150 arcsec in XEL and -900 arcsec in LOS. Over the course of the test

which started at about t=6600 s, the TA position drifted only about 4 arcsec in EL and XEL and 3 arcsec in the LOS-axis.



**Figure 5.6.** Spherical sensor measurements during FD open loop test.

### 5.2.3 Angular rate data assessment

Before processing the measured angular rate data and determining the noise parameters, the raw rate data were examined for disturbances and data anomalies. The most suitable data sections were then selected for further analysis. The processed angular rates were already calibrated internally in the ATCU (Attitude Control Unit): the temperature dependent absolute bias was subtracted from the raw rate data and the temperature dependent scale factor was corrected as well.

During data checking, a large angular rate deviation was discovered for TC-1 which revealed a gyro malfunction of the EL gyro. The large rate deviation influences the analysis of the noise parameters substantially. Therefore, the section with the EL gyro anomaly was excluded for further analysis. The analyzed data are split up into two sections – one before the anomaly and one after – and are evaluated separately.

Data sections of the angular rates for all four test cases are compared in Figure 5.7. The activation of the oil pumps can be clearly seen for TC-2 – TC-4 and the frequencies are identified in the previous section 5.2.2. The amplitudes of the measured frequencies are increasing when the telescope configuration is changed from caged to uncaged (TC-2 – TC-3). Through the uncaging process on ground, the telescope is pulled away from the axial VIS hard stops. This permits vibration isolation from the aircraft, but at the same time, the telescope structure is more unrestrained axially and the excited frequencies can develop more freely. Hence, their amplitudes rise. When the FD brakes are released (TC-4), the amplitude of the frequencies decrease again due to the rotational isolation of the RIS. All angular rate plots for the four test cases are shown in [Harms 2007b].
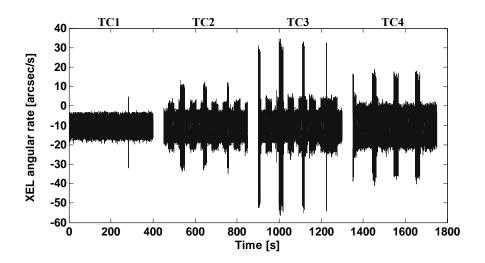
**Figure 5.7.**    Example of angular rates from the XEL gyro during the different test cases.

### 5.2.4    Rate bias and integrated rates

The measured rotation rates were averaged for each test case in order to assess the absolute rate bias values. As mentioned, the rates were calibrated with a temperature dependent scale factor and bias model. The mean values of the angular rates are shown in Table 5.7. They show good consistancy over the three day test period. The average of all test cases is then corrected for its known misalignment using the latest gyro alignment matrix [Harms 2005a].

The mean values of the measured rotation rates are then compared to the theoretically expected values given in section 4.1. The theoretical values are calculated using equations (4.1)-(4.3) with the CD elevation of 40.1007°, the latitude of N 34.9368° and the GPS measured heading of 324°. All values are listed in Table 5.7.

The deviations of these values were calculated to the aligned average of all the perfomed test cases. The absolute value of the measured rate deviates from the theoretical value about 0.16°/h indicating the residual bias errors of the gyros.

With a heading of 324°, the bias values for each axis are between 0.3 and 0.5°/h. As the theoretically calculated rotation rates are sensitive to errors of the heading measurements and the heading error is assumed to be as large as 2°, these bias values are most likely not real. When calculating the bias values for various headings, the minimum least square value of the biases appears at a heading of 327.7°. The bias values are then between 0.06 and 0.16°/h.

**Table 5.7.**    Measured angular rates compared with theoretical values. Values are recalibrated with correct axis assignment.
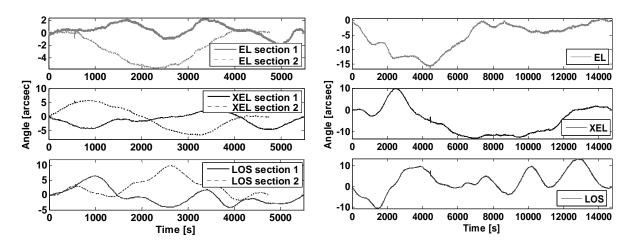
|  | EL [°/h] | XEL [°/h] | LOS [°/h] | Absolute value [°/h] |
|---|---|---|---|---|
| Measurement mean values |  |  |  |  |
| TC-1 section 1 | 10.4734 | -10.5698 | 0.2601 | 14.8822 |
| TC-1 section 2 | 10.4754 | -10.5663 | 0.2582 | 14.8811 |
| TC-2 | 10.4719 | -10.5593 | 0.2563 | 14.8736 |
| TC-3 | 10.4506 | -10.5634 | 0.2685 | 14.8618 |
| TC-4 | 10.5024 | -10.5465 | 0.2473 | 14.8859 |
| Average of all test cases | 10.4747 | -10.5610 | 0.2581 | 14.8769 |
| Misalignment corrected average | 10.3002 | -10.7287 | 0.3495 | 14.8769 |
|  |  |  |  |  |
| Theoretical values |  |  |  |  |
| GPS measured |  |  |  |  |
| Heading = 324° | 9.9755 | -11.2571 | 0.0059 | 15.0411 |
| Deviations to aligned average of test cases | 0.3247 | 0.5284 | 0.3436 | -0.1642 |
|  |  |  |  |  |
| Minimum least square value of biases |  |  |  |  |
| Heading = 327.7° | 10.3645 | -10.8911 | 0.4404 | 15.0411 |
| Deviations to aligned average of test cases | -0.0643 | 0.1624 | -0.0909 | -0.1642 |

A simple integration of the rates can be performed when the gyro rates of each axis are treated separately. The measured rates can be converted back to the initially measured angular increments by multiplying the rates with the sampling period. Summing up these angular increments yields the rotated angle over time. The measured rotation angles are due to Earth's rotation rate and the constant biases of the gyros but also show the effect of the integrated noise present in the data.
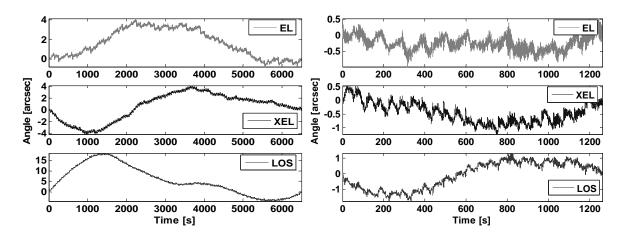
After subtraction of the averaged rate over the total test time, the residual angular error can be extracted for each gyro. The angular error progressions over time are shown for the four different test cases in Figure 5.8 and Figure 5.9.

Assuming that the exact bias error is known, the data show that the angular errors are within 20 arcsec, even for TC-2 with the longest test duration of 4 hours. Generally, the LOS gyro has the largest error. Sinusoidal oscillations are noticeable for the LOS gyro during TC-1 and TC-4 with a period of approximately 20 min. This oscillation was noticed before and is documented in [Moik 2000]. During TC-2 the periodic oscillation that is visible, has a period of 40 min.

In practice, the angular errors will be larger because the exact bias over the test time is not known ahead of time (this includes also the long term noise). The angular error will not be zero at the test end but rather rise linearly depending on the accuracy of the estimated bias.

**Figure 5.8.**  Mean value subtracted, integrated rates during TC-1 (left side) and TC-2 (right side).



**Figure 5.9.**  Mean value subtracted, integrated rates during TC-3 (left side) and TC-4 (right side).

### 5.2.5  Power spectral density results

The PSD was estimated using MATLAB with its integrated Welch's averaged, modified periodogram method. The number of Finite Fourier Transform (FFT) points was set to $2^{16}$ and the data were divided into sections of length equal to $2^{14}$ with 50% overlap. Each section was windowed with a Hamming window and a modified periodogram was computed. The periodograms were then averaged. The estimated PSD is one-sided and the frequency values span the interval from 0 to 200 Hz (Nyquist frequency).

The angular rate PSD plots are shown for the EL, XEL and LOS gyros for all test cases in Figure 5.10 to Figure 5.12. The ARW (white noise on the angular rates) has a flat spectrum in the rate PSD plots and the specified value is added into the PSD plots as a constant, dashed line. In the low frequency region, two frequencies at 0.7 Hz and 1.3 Hz stand out and are present during all test cases. Their largest amplitude is measured by the EL gyro.

During TC-1, a series of frequencies is prominent in the EL and XEL gyros between 10 and 100 Hz. They have an equal spacing of about 3.3 Hz. The frequency with the largest amplitude is found at 179.1 Hz which is associated with the operation of the gyros themselves. The underlying white noise (ARW) has the specified level.

The activation of the oil pump system (TC-2 – TC-4) leads to an additional 30 Hz frequency and a rise of the high frequency content (>100 Hz). The frequencies are identified in section 5.2.2. As well, the amplitude of the frequency band around 10 Hz rises. The level of the underlying white noise (ARW) slightly increased.

As expected, the process of uncaging leads to a drop of the PSD for TC-3 for frequencies larger than 3 Hz. This is visible in particular for the XEL and LOS gyro. An increase of the natural frequency of the VIS at 2.3 Hz is noticeable. The underlying white noise (ARW) has the specified level.

The PSD measured during TC-4 shows the improvement of vibration isolation by the RIS with released FD brakes for frequencies larger than 1.5 Hz. While the frequency amplitudes of 0.7 Hz and 1.3 Hz decrease for the XEL and LOS, they clearly rise for the EL gyro. Additionally, the EL gyro measures frequencies at 1.0 Hz and 3.4 Hz. For all three axes, the PSD rises for frequencies smaller that 0.4 Hz. This could indicate a unsought influence of the spherical sensors on this open loop test since they show a high amplitude frequency at 1 Hz.
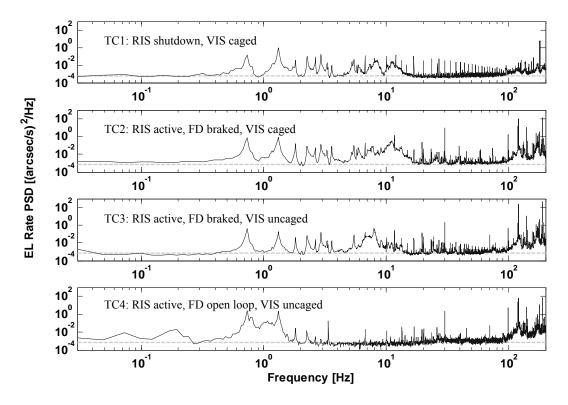


**Figure 5.10.** Rate PSD of EL gyroscope shown for all test cases.
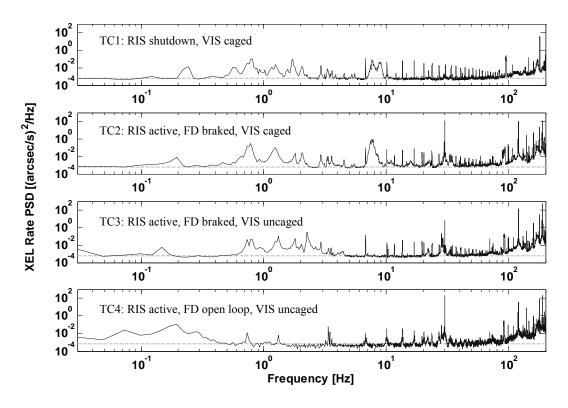
**Figure 5.11.** Rate PSD of XEL gyroscope shown for all test cases.
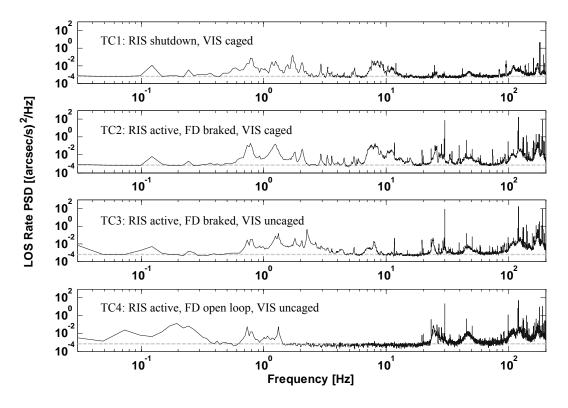


**Figure 5.12.** Rate PSD of LOS gyroscope shown for all test cases.

### 5.2.6    Allan Variance results

The identification of the noise processes occurring in gyroscopes signals is described in section 4.2. For the SOFIA gyroscopes, the noise parameters of interest are the ARW and the bias stability. The ARW can be identified in the AV plot with the slope -0.5 on a log-log scale. The bias stability is the lowest point on the AV curve.

The complete results of the AV analysis are shown for each test case and each gyro in [Harms 2007b]. A selection is given below.

To produce a smooth AV plot, the AV values are calculated for multiple averaging times. The smallest averaging time is the sampling time 0.0025 s and the largest averaging time is a third of the test time which yields an 1-$\sigma$ error of 50% for that AV value (equation (4.25)). The calculated AV curve is plotted along with the results of the manufacturer and the specifications as a reference. The same plots are summarized in Figure 5.13 to Figure 5.16 in which the AV results for the three gyros are plotted in one figure for each test case. The 1 $\sigma$ error bars are added.

For TC-1, where the data set is divided into two sections, two AV curves are available. In the following comparison, the data sections with the better noise parameters are used. This is section 1 for the LOS gyro and section 2 for the EL and XEL gyro.

The results of TC-1 confirm that the ARW of the gyros is smaller than the specified value for averaging time > 10 s. The bias stability, the lowest point on the AV curve, is also better than the specification. For comparison, the data gathered during the on sky test period in 2004 are added to the plot, showing the significant drop of the noise level of the new measurements.

Several bulges of the AV curve are visible for averaging times smaller than 10 s and are caused by present frequencies in the data. They are identified in section 5.2.5 and are real measured frequencies as opposed to noise of the sensors. The AV curve has its lowest point at much smaller averaging times than originally measured by the manufacturer. They measured the bias stability at averaging times of about 500 s, whereas here, the bias stability values are measured at an averaging time of 240 s for the EL gyro, 100 s for the XEL gyro and only 50 s for the LOS gyro. It indicates a higher rate random walk and rate ramp coefficients, respectively a higher white noise on the measured angular accelerations caused by the environment. Particularly for the LOS gyro, the AV values are high for large averaging times, but abate for even larger averaging times. This is caused by the 20 min. oscillation of the data as seen in Figure 5.8.
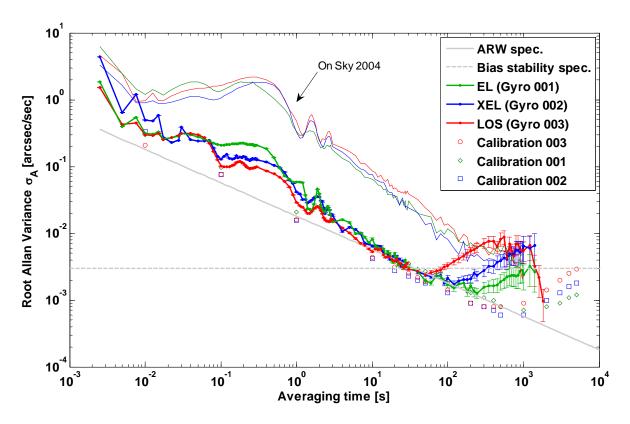
The results of TC-2 show that the activation of the oil pump system increases the measured ARW, respectively the level of white noise on the measured angular rates. The noise level rises especially for the EL gyro. The AV values also rise for small averaging times confirming the sensitivity of these measurements to the induced vibrations. As TC-2 is the test with the longest set of data that was suitable for analysis, the AV could be calculated for averaging times up to 4800 s. Although the error bars are high, the data indicate that the AV curves come close to the manufacturer measurements for averaging times larger than 3000 s. The

data corroborate that the rise of the AV between averaging times of 100 s and 1000 s is due to the 20 min. oscillation which appears particularly in the LOS gyro.

The results of TC-3 show that the AV curve has a significant bulge at an averaging time of about 20 s for the XEL and LOS gyro. The AV curve of the EL gyro is not much affected which is an indication that this low frequent oscillation is introduced by the uncaging of the VIS. Regarding the AV curve at high averaging times shows a good agreement with the manufacturer measurements for the EL gyro. The bias stability value for the XEL gyro is also lower at high averaging times than during the caged measurements. The AV values of the LOS gyro are slightly reduced compared to the caged measurements but yet much higher than measured by the manufacturer due to the 20 min. oscillation.

The results of TC-4 show a much higher ARW for averaging times between 1 and 60 s than during the previous tests. The ARW, respectively noise level on the angular rates, drops for averaging times larger than 60 s. The additional measured frequency of 3.4 Hz causes the significant bulge of the AV curve on the EL gyro at 0.3 s. Due to the short test time, the AV curve can be calculated only up to an averaging time of 500 s and no statement about the bias stability is possible.

The ARW coefficients are determined by performing least square fits on the AV curves for the averaging time regions with the slopes -0.5. The results are listed for all the test cases in Table 5.8. The averaging time regions for which the fits were performed are explicitly mentioned. For TC-3 and TC-4, two ARW coefficients are determined: one for the high noise level up to an averaging time of 50 s, the other for averaging times larger than 70 s. The bias stability values are determined by the lowest value of the AV curve. The averaging time is indicated at which the value is read off.

**Figure 5.13.** Root Allan Variance results for TC-1. The AV curves from the on sky measurement in 2004 are added.
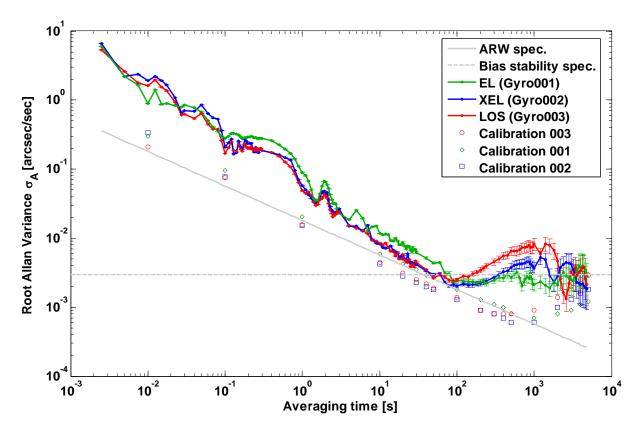


**Figure 5.14.** Root Allan Variance results for TC-2.
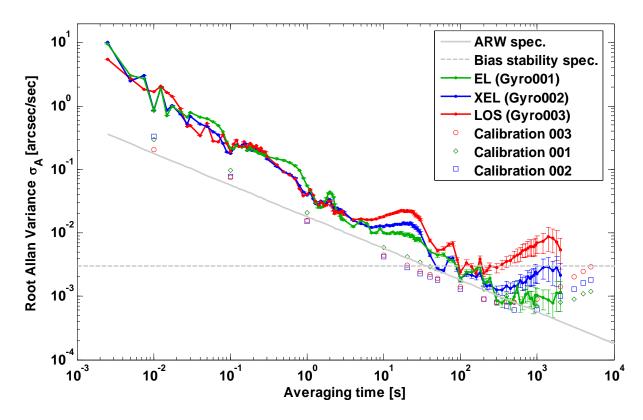
**Figure 5.15.** Root Allan Variance results for TC-3.
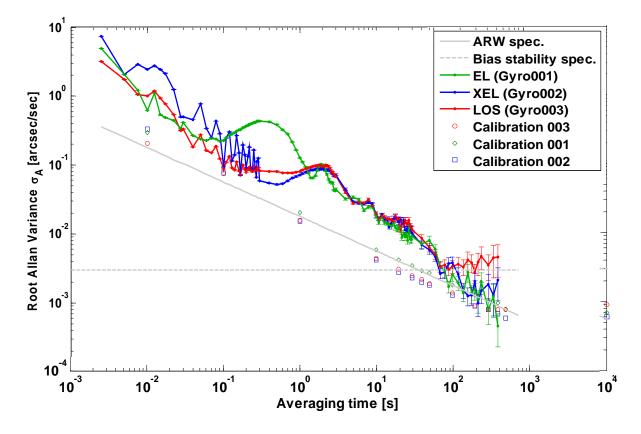


**Figure 5.16.** Root Allan Variance results for TC-4.

**Table 5.8.** Measured ARW and bias stability coefficients.

| | ARW [arcsec/√s] | Fit performed for averaging times between | Bias stability [arcsec/s] | Parameter read at averaging times |
|---|---|---|---|---|
| Specification | 0.0180 | | 0.0030 | |
| **EL** | | | | |
| Manufacturer measurement | 0.0144 | 1 and 300 s | 0.0008 | at 500 s |
| TC-1 | 0.0173 | 17 and 220 s | 0.0013 | at 240 s |
| TC-2 | 0.0370 | 3 and 140 s | 0.0019 | between 10 and 2000 s |
| TC-3 | 0.0350 | 3 and 120 s; 300 and 350 s | 0.0007 | at 600 s |
| TC-4 | 0.0567 0.0227 | 4 and 50 s 70 and 400 s | n/a | |
| **XEL** | | | | |
| Manufacturer measurement | 0.0132 | 1 and 500 s | 0.0007 | at 1000 s |
| TC-1 | 0.0183 | 9 and 140 s | 0.0019 | at 100 s |
| TC-2 | 0.0233 | 12 and 100 s | 0.0020 | at 100 s |
| TC-3 | 0.0235 | 50 and 350 s | 0.0013 | at 350 s |
| TC-4 | 0.0656 0.0239 | 4 and 50 s 70 and 400 s | n/a | |
| **LOS** | | | | |
| Manufacturer measurement | 0.0180 | 1 and 500 s | 0.0006 | at 500 s |
| TC-1 | 0.0178 | 6 and 60 s | 0.0027 | at 50 s |
| TC-2 | 0.0223 | 12 and 80 s | 0.0024 | at 90 s |
| TC-3 | 0.0363 | 1 and 4s; 90 and 160 s | 0.0023 | at 160 s |
| TC-4 | 0.0691 | 4 and 50 s | n/a | |

The ARW coefficients measured during TC-1 meet the specifications. The ARW coefficients measured during TC-2 – TC-4 do not meet the specification due to the noise and vibrations induced by the oil pump system. The bias stability values meet the specification during all long term test cases (TC-1 – TC-3). No bias stability information is available for TC-4 due to the short test time.

Comparing the AV curves and resultant noise coefficients of the four different test cases and the manufacturer measurements leads to some conclusions given below. The corresponding plots for the EL, XEL and LOS gyros are shown in Figure 5.17. The error bars are not shown to keep the plots clear.

During TC-1, the smallest ARW coefficient is measured. The long term noise parameter, the bias stability, occurs at smaller averaging times and is higher than during the vibration isolated test cases. The AV for TC-2 is high due to induced vibration by the oil pump system. But for very large averaging times, the AV values approach the values measured by the manufacturer.

The AV for TC-3 matches partly the low values of TC-1, but for various regions the higher values of TC-2. This indicates the frequency isolation regions of the VIS. The bias stability values during TC-3 are the lowest for all test cases and agree well with the manufacturer measurements for the EL gyro.
The AV for TC-4 is low for small averaging times proving the rotation isolation of the RIS but rises to an unexpected high level for medium averaging times due to low frequent oscillation on the data.

Certain frequencies are measured disturbing the noise analysis. They are induced by ground support and TA subsystems and could be identified. The step by step activation of the SUA can be verified with the PSD results. The activation of the oil pump system leads to an increase of the overall noise and excites certain frequencies. The VIS uncaging isolates vibrations in XEL and LOS larger than 3 Hz and leads to an amplitude increase of its natural frequency at 2.3 Hz. Releasing the FD brakes and allowing the TA to float isolates residual vibrations above 2 Hz. At the same time, low frequency content rises and a 1 Hz frequency is additionally measured. It is not understood why the outstanding frequencies at 0.7 and 1.3 Hz are not isolated through the RIS. This effect might be caused by the spherical sensors signals.

EL (Gyro 001)

XEL (Gyro 002)

LOS (Gyro 003)
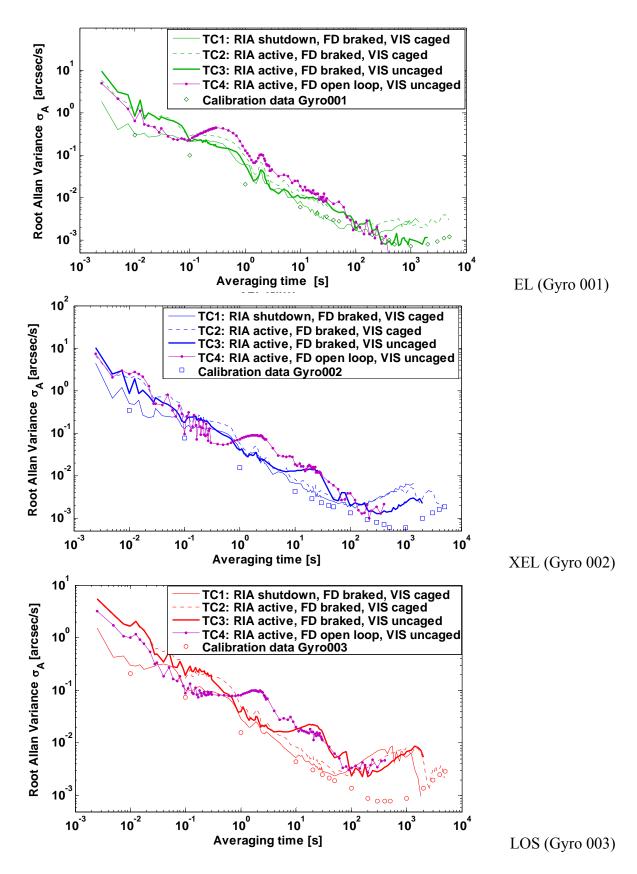
**Figure 5.17.** Comparison of root Allan Variance curves for TC-1 – TC-4 in each gyro.

# 6  Analysis of on sky sensor alignment measurements

The first on sky observations with the SOFIA telescope were performed between August 18th and September 10th 2004. In addition to the functional testing of the various TA subsystems that interacted together for the first time, a variety of alignment measurements, structural flexure measurements and pointing measurements were performed. The results are discussed in this chapter and related to the reference frame alignment concept described in chapter 3. Together with the acquired knowledge of sensor and system performance in chapter 5, recommendations are established regarding a basic concept for automating these measurements. The process can be streamlined regarding the sequence of the maneuvers and the tools that are used for post-processing of the measurement data.

The test series was accomplished without a reflecting coating applied to the primary mirror, which was compatible with the bright stars selected for this work. From an astronomical observing point of view, the environmental conditions were not optimal considering the high outside temperatures and humidity. Since Polaris is one of the brighter stars in the night sky and makes only small changes in position throughout the night, it was selected as a reference star for most of the alignment tests.

## 6.1  Gyroscope reference frame alignment

This section describes the GYRF alignment measurements that were performed during the on sky test in 2004 with the reference instrument HIPO. The alignment procedure and the used algorithms are described in detail in section 3.3.2.

Due to the high noise levels in the data, the alignment procedure was performed iteratively. The major uncertainty in the data, aside from image wander due to atmospheric seeing, was gyroscope drift. Before the series of alignment commands were executed, the gyroscope bias drift was estimated for several minutes. Beyond this, a residual drift was seen in the data, which was estimated and taken out of the data by post-processing.

The TA was also exposed to various external perturbations. These include aircraft and ground support equipment but also perturbations that are caused by the people that were present on

the aircraft. The influence of the TA subsystem activation as well as the external perturbations are described and analyzed in detail in section 5.2.2. Typical noise levels during an observation night are shown in Figure 5.13 by means of AV analysis of the measured gyroscope data. During the alignment measurements in 2004, the TA was operated in inertial stabilization and the VIS was caged.

Effects from atmospheric seeing were mitigated by taking images with an exposure time as long as possible without saturation of the CCD pixels. The fact that the primary mirror had not been aluminum coated was helpful in this regard. Most of the measurements were performed using Polaris and an exposure time of 0.5 seconds was selected. For the few measurements with fainter stars, an exposure time of 5 seconds was set. After reducing the data for the residual linear gyroscope drift, these perturbations produce centroid instabilities of approximately 0.3 arcsec RMS (1 pixel in HIPO) in each axis. This is in agreement with the AV noise level shown in Figure 5.13. Table D.1 and D.2 in Appendix D provides an overview and more details of the performed alignment tests.

Conforming to the proposed alignment sequence in section 3.4.2, the LOS-axis alignment measurements are presented first. The maximum angle for LOS rotations is limited to 6° depending on the position of the FD. However, operationally the LOS rotation angles were limited to between 3° and 5.5° to keep away from end of travel limits. The LOS turning point which corresponds to the projected origin of TARF on the HIPO CCD is used as a measure for the LOS-axis misalignment. Table 6.1 shows the results for the five alignment test runs with respect to the nominal TARF origin. It is defined in HIPO at pixel location $(X_0=559/Y_0=489)$.

**Table 6.1.** Differences of turning point locations to nominal position at $(X_0=559/Y_0=489)$ along HIPO axes X and Y.

| Implemented matrix | Raw values [arcsec] | | Values corrected for drift [arcsec] | | Values used for alignment matrix [arcsec] | | Residual drift [arcsec/min.] | |
|---|---|---|---|---|---|---|---|---|
| | ΔX | ΔY | ΔX | ΔY | ΔX | ΔY | X | Y |
| **not aligned** | -1151.5 | -324.8 | * | * | -1237.5 | -319.8 | * | * |
| **#2** | -24.3 | 222.8 | -17.9 | 226.5 | 0.2 | 205.7 | 1.9 | 2.3 |
| **#3** | 14.5 | 31.8 | 9.9 | 35.4 | | | -1.3 | 0.8 |
| **#4 (repeat)** | 3.4 | 17.8 | 3.0 | 17.7 | -18.7 | 18.6 | -0.8 | -0.1 |
| **#5** | 25.7 | 1.3 | 24.9 | 3.5 | | | -0.5** | 0.4** |

\*        *No drift information available for LOS measurements*

\*\*       *Drift estimated from 30 frames taken after measurement*

In the first column, the results of the turning point deltas are shown using raw, not drift corrected centroid data. The initial measurement - before an alignment matrix was implemented - reveals a misalignment of the LOS-axis of about 20 arcmin relative to its nominal position. The second column lists the turning point deltas that were calculated taking the residual gyroscope drift into account. This was done mainly after the test series was completed during post-processing.

The values that were calculated during the real-time analysis and that were used for the matrix implementation are shown in the third column. The values are not correct as the data was evaluated only partially during the test series and the algorithm used at that time had minor errors. However, their disagreement with the drift corrected values explains the former need for multiple test runs. Despite these circumstances during the alignment measurements, the initial misalignment of about 20 arcmin was reduced to 25 arcsec after the last alignment matrix was implemented.

Usually, three to four images are taken before and after an alignment maneuver. The averaged centroid values of these images are then taken to calculate the rotation axis. The images are also used to estimate the residual gyro drift. Minimizing the sum of the square errors of the measurements to a simple time linear function yields the estimate of the residual drift. The UTC at the center of an exposure can be used to establish the time dependency. All images can be used for fitting when the rotation maneuvers are of equal size.

When the alignment maneuvers are done during ground observations, the TA is in inertial stabilization and due to the limited FD motion range, the motion limit is approached frequently. Alignment maneuvers of different sizes can avoid that situation but the images cannot be used for the drift estimation. Then, the residual gyro drift needs to be estimated by a set of frames taken directly after the alignment measurements.

In Table 6.2, the turning point locations are shown in HIPO pixels for positive and negative rotations along with their standard deviations as well as the RSS of the two pixel standard deviations. Systematic errors that depend on the rotation direction cannot be noticed. It can be seen that the standard deviation depends on the number of performed maneuvers and in particular on the size of the alignment maneuver as derived in section 3.5.

While the alignment matrix #2 was implemented, two stars could be captured within HIPO's field of view at the same time. An alternative method also described in section 3.3.2 was applied to calculate the turning point location. The results are presented in Table 6.3 and compared to the method that uses only one star to calculate the turning point. However, accounting for the number of measurement, the single-star-method is applied to both stars and the resulting turning points are averaged. As expected, the two methods provide the same results and the standard deviations are of the same order of magnitude.

**Table 6.2.** Turning point locations on HIPO CCD for positive and negative alignment maneuvers.

| Implemented matrix | Rotation direction | Drift values [pixel] | corrected | Standard deviation [pixel] | | | No. of maneuvers | Total angle [degree] |
|---|---|---|---|---|---|---|---|---|
| | | Pixel *X* | Pixel *Y* | Pixel *X* | Pixel *Y* | RSS | | |
| **#2** | Positive | 505.9 | 1181.4 | 3.0 | 10.2 | 10.6 | 3 | 15.0 |
| | Negative | 502.8 | 1181.8 | 3.0 | 7.5 | 8.1 | 3 | -14.5 |
| | Both | 504.4 | 1181.6 | 3.3 | 8.9 | 9.5 | 6 | |
| **#3** | Positive | 588.7 | 595.3 | 10.7 | 16.4 | 19.6 | 3 | 13.5 |
| | Negative | 590.4 | 600.3 | 2.4 | 39.4 | 39.5 | 2 | -9.0 |
| | Both | 589.3 | 597.3 | 8.5 | 28.1 | 29.4 | 5 | |
| **#4 (repeated)** | Positive | 561.1 | 544.2 | 1.7 | 11.4 | 11.5 | 3 | 15.0 |
| | Negative | 575.4 | 541.9 | 10.9 | 12.9 | 16.9 | 3 | -13.5 |
| | Both | 568.3 | 543.0 | 10.6 | 12.2 | 16.2 | 6 | |
| **#5** | Positive | 621.8 | 548.8 | 7.2 | 3.3 | 7.9 | 3 | 15.0 |
| | Negative | 648.4 | 493.1 | 16.9 | 12.8 | 21.2 | 3 | -14.0 |
| | Both | 635.1 | 499.7 | 18.6 | 11.4 | 21.8 | 6 | |

**Table 6.3.** Turing point locations on HIPO CCD calculated using an alternative method with two stars.

| Implemented matrix | Rotation direction | Drift corrected values [pixel] | | | | Standard deviation [pixel] | | | |
|---|---|---|---|---|---|---|---|---|---|
| | | Single star | | Two stars | | Single star | | Two stars | |
| | | Pixel *X* | Pixel *Y* | Pixel *X* | Pixel *Y* | Pixel *X* | Pixel *Y* | Pixel *X* | Pixel *Y* |
| **#2** | Positive | 505.8 | 1182.5 | 505.0 | 1182.5 | 3.1 | 9.7 | 2.7 | 10.9 |
| | Negative | 502.8 | 1182.4 | 504.3 | 1177.4 | 3.1 | 6.8 | 1.7 | 2.2 |
| | Both | 504.3 | 1182.5 | 504.7 | 1180.5 | 3.4 | 8.4 | 2.3 | 8.9 |

After the LOS-axis alignment is performed, the EL- and XEL-axes misalignment can be measured according to the alignment sequence in section 3.4.2. The rotation angle for the alignment commands are set for EL and XEL to 6 arcmin, after initial LOS-axis alignment to 4.8 arcmin keeping the centroid within HIPO's 5.6 arcmin field of view but allowing large rotations. The results are presented in Table 6.4. The EL- and XEL-axes alignment measurements were performed before an alignment matrix was implemented. The measurements reveal an initial misalignment of about 1 degree. As the angle selected for the alignment matrix calculation #5 was slightly smaller, a remaining misalignment error of about 4 arcmin was measured after the last alignment matrix was implemented.

**Table 6.4.** Misalignment angles determined during EL and XEL measurements.
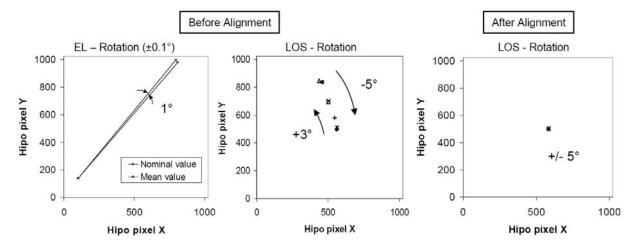
| Implemented matrix | Rotation axis | Angle corrected with drift | Standard deviation | Angle used for calculation | Residual drift [arcsec/min] | |
|---|---|---|---|---|---|---|
| | | [arcmin] | [arcmin] | [arcmin] | X | Y |
| Not aligned | U | 61.6 | 3.9 | 56.7 | -0.01 | -1.15 |
| | V | 59.9 | 4.4 | 56.7 | -0.24 | -0.17 |
| #5 | U | 3.8 | 2.0 | | 1.46 | 0.10 |
| | V | 4.0 | 2.6 | | 0.99 | 0.01 |

Using the results from Table 6.2 and Table 6.4 for the residual axes misalignment that was measured while alignment matrix #5 was implemented, a new alignment matrix can be calculated:

$$A_{TARF,GYRF} = \begin{pmatrix} 9.9984199e\text{-}01 & 1.7431537e\text{-}02 & -3.4832506e\text{-}03 \\ -1.7413946e\text{-}02 & 9.9983577e\text{-}01 & 5.01810311\text{-}03 \\ 3.5701519e\text{-}03 & -4.9476375e\text{-}03 & 9.9998186e\text{-}01 \end{pmatrix} \qquad (6.1)$$

The results of the alignment procedure are summarized in Figure 6.1, displaying the situation before (left side for the EL and center for LOS rotations) and after the misalignment was corrected (right side). In each figure, the centroid locations are shown before and after the rotations took place. The results indicated that GYRF without calibrations, i.e. the as-built and mounted orientation of the gyroscope box, is rotated relative to TARF by approximately 20 arcmin for the LOS axis and by approximately 1° for the EL and XEL axes.



**Figure 6.1.** HIPO measurements before (left side and center) and after (right side) the misalignment was corrected.

As shown in Figure 6.1 on the right side, the implementation of the alignment matrix is clearly improving the LOS axis orientation. While performing LOS rotations of ± 5°, the centroid location after the few calibrations accomplished remains reasonably constant at the center of the SI flange.

The alignment maneuvers were performed for each axis six times (Table 6.2). Before and after a rotation, three HIPO images were recorded and the calculated centroid locations were averaged. These two numbers are combined to a total of 3 x 6 = 18 measurements for one axis. Using the relations in section 3.5 this leads to the expected misalignment errors shown in Table 6.5. For this analysis, it is assumed that $\sigma_c$ equals at best one pixel RMS in each direction, which corresponds on the HIPO CCD to 0.327 arcsec. However, the environmental conditions varied greatly during the course of the alignment measurements. Therefore, the measured standard deviations shown in Table 6.2 are partially larger than the expected standard deviations.
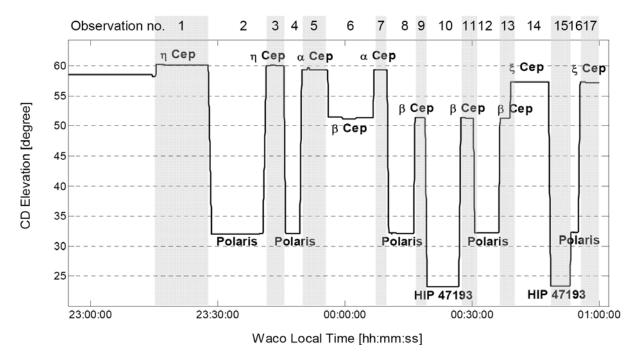
**Table 6.5.** Expected misalignment errors depending on number of measurements for a centroiding error $\sigma_c$=0.327 arcsec (1 pixel on HIPO CCD).

| | **LOS ($\gamma$=4°)** | | **EL/XEL (L=4.8 arcmin)** |
|---|---|---|---|
| n [-] | $\sigma_R$ [arcsec] | $\sigma_R$ [pixel] | $\sigma_\beta$ [arcmin] |
| 1 | 5.3 | 16.2 | 5.5 |
| 18 | 1.2 | 3.8 | 1.3 |

## 6.2   Imager reference frame flexure measurements

Using Polaris at an elevation of ~32°, the pixel location of TARF's origin in the three imagers and their transformations to each of the other reference frames were determined and documented [Meyer 2005]. For measuring elevation dependencies, six different stars were brought successively in the field of view of the FPI and were located at the TARF origin. These six stars have large angular separations covering nearly the entire operational elevation range of the telescope. The telescope was moved several times between these six stars, mostly between stars with a large elevation difference. In total, sixteen motions between these stars were commanded, which cover the CD elevation range from approximately 23° to 60°. Figure 6.2 provides an overview of the test series showing the time dependent actual CD position in degrees, as an approximate measure of the elevation angle, and the identifier of the observed stars at this elevation. In addition, the star observations are numbered consecutively. Star chart sections with the six observed stars at begin and at the end of the test are shown in Figure 6.3 along with the horizontal coordinates Azimuth and Altitude (Appendix C.4.2). The altitude is the angle of the star above the horizon at the observatory location and at the observation time and corresponds approximately to the CD elevation angle of the telescope.
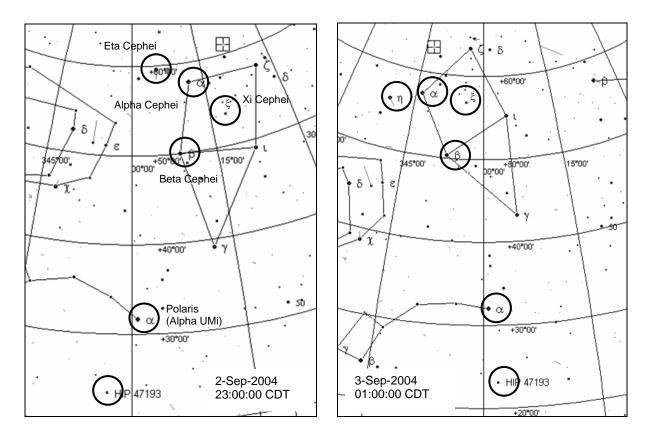
More details on the observatory location in Waco, TX and the conditions during the tests are described in [Harms 2005c].



**Figure 6.2.**  Telescope elevation (CD angle) during star observations over observation time (local time in Waco: CDT) in the night from 02.-03.09.2004.

During the test, the observed stars are imaged in two of the three cameras: FPI and FFI, as well as in HIPO. The exposure time of HIPO was set to 0.5 seconds for Polaris, Beta Cephei, Alpha Cephei and Eta Cephei, and to 2 seconds for HIP47193 and Xi Cephei. The exposure times of the FPI and FFI were set to 2 seconds for the entire test series.

The HIPO centroid data was obtained using the center of mass algorithm described in section 4.3.1. Synchronizing the HIPO centroid data and the imager centroid data requires knowing the exact timing between the two systems. This can be done using the UTC timestamp which is recorded with the HIPO images and the TA housekeeping data using the EGSE (Electrical Ground Support Equipment). However, the UTC timestamp could not be extracted with the data recorded with the EGSE and the time difference to the local computer system time had to be read out manually causing imperfect correlation [Harms 2005b]. In addition, different sampling rates of HIPO and the imager centroid data required interpolation of the imager data to match the according HIPO timestamps.
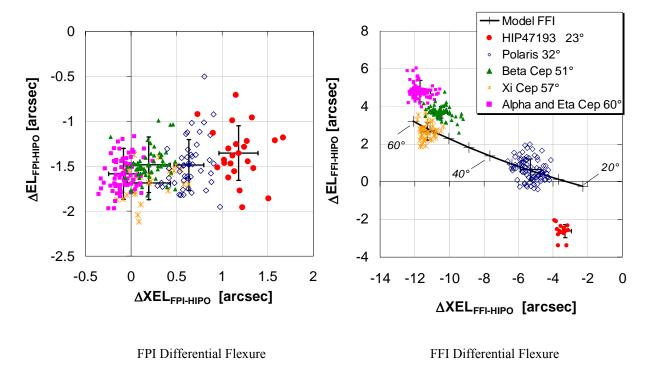
**Figure 6.3.** Observed stars along with horizontal coordinates Azimuth and Altitude at start and end time of the test run. The Sky chart is produced using [Cartes du Ciel 2004].

The centroids obtained from the FPI and FFI are compared to those from HIPO by building their differences in EL and XEL, see Figure 6.4. The standard deviations are indicated as error bars at the mean values. It is measured that the boresight position in the FPI relative to that in HIPO changes about 1.1 arcsec in XEL for an elevation change from 23° to about 60°. The effect in elevation is less than 0.27 arcsec. The internal flexure of the HIPO focal plane and the SI flange assembly focal plane itself is measured to be about 0.3 arcsec each in EL and XEL [Haas 2005]. Finite element calculations predict much less flexure (about 0.1 arcsec) for the FPI [Herdt 1998b]. Over the same elevation range, the boresight of the FFI changes relative to that in HIPO by about 9 arcsec in XEL and about 8 arcsec in EL. The differential flexure measured in the FFI is significantly larger due to the fact that the FFI (like the WFI) is mounted on the metering structure and the FPI at the instrument flange. The FEM model predictions for the FFI (see section 3.4.1) are compared to the measurement data in Figure 6.4 and agree reasonably well. These results are very similar to the differential flexures measured between the FFI and the FPI, analyzed in [Meyer 2005]. Temperature effects were not considered during this first experiment series.

While the measurement was performed, the imager boresights were not aligned by means of alignment matrices. The alignment was performed manually by setting the SI boresight definition in the imagers to the measured TARF origin values in [Meyer 2005]. The TARF origin values were measured using Polaris at ~32° and differential flexure is assumed to be

zero at that elevation. The data in Figure 6.4 suggests that there is still a small offset remaining between the measured TARF origin and the data used for the boresight definition.



FPI Differential Flexure                    FFI Differential Flexure

**Figure 6.4.** Boresight changes of imagers relative to HIPO at the focal plane depending on the telescope's elevation angle. The differential flexure for the FPI is shown in the left plot and for the FFI in the right plot.

## 6.3  Absolute pointing measurements

The observations of the six stars used in the previous section 6.2 permitted evaluation of absolute pointing performance. The positions of these stars are known to significantly less than 1 arcsec on the sky and published in a number of star catalogues [Perryman 1997]. After correcting for atmospheric refraction (between 30 arcsec for the star at highest elevation and 130 arcsec at lowest, see below), the expected apparent angular separations between these stars can be calculated for the ground observing location. These angles are then compared to the measured rotation angles which were comprised of the gyroscope information and the small correction from the image position in the sensor.
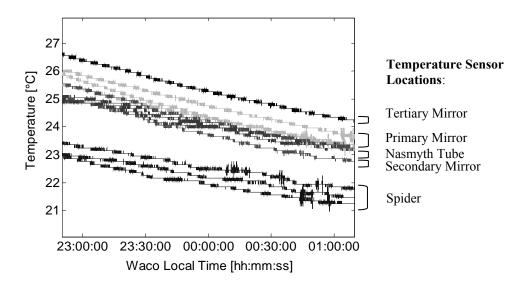
The astrometric position of the six observed stars is represented on the sky by their equatorial coordinates Right Ascension and Declination (Appendix C.4.1). The star coordinates are listed in Table 6.6 along with their observation numbers assigned in Figure 6.2. The precession corrected coordinates are calculated using an astronomical database [SIMBAD 2001]. The epoch and equinox 2004.7 is assumed to be constant over the observation period.

**Table 6.6.** Right Ascension and Declination of observed stars for an epoch and equinox of 2004.7 [SIMBAD, 2001].

| Star identifier | Observation No. | Right Ascension [degree] | Declination [degree] |
|---|---|---|---|
| Eta Cephei | 1, 3 | 311.3464 | 61.8574 |
| Polaris | 2, 4, 8, 12, 16 | 39.3260 | 89.2848 |
| Alpha Cephei | 5, 7 | 319.6732 | 62.6058 |
| Beta Cephei | 6, 9, 11, 13 | 322.1799 | 70.5816 |
| HIP 47193 | 10, 15 | 144.4339 | 81.3048 |
| Xi Cephei | 14, 17 | 330.9822 | 64.6513 |

Before deriving the apparent angular separations of the observed stars, their astrometric positions on the sky had to be adjusted for refraction (section 4.3.2). Therefore, the star positions had to be expressed in horizontal coordinates Altitude and Azimuth taking into account the observer's location and the observing time (equations (C.1)-(C.3), Appendix C.4.2).
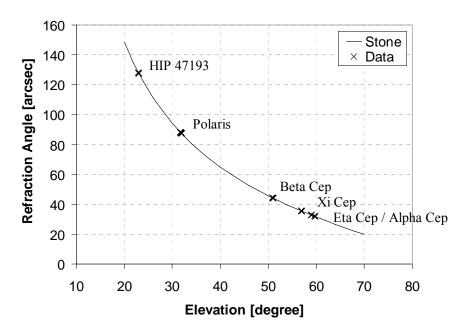
The only TA sensors in the cavity that give information about the atmospheric conditions are several temperature sensors that are placed on the rear side of the three mirrors and on the metering structure. The measurements are shown for the test period in Figure 6.5. The temperature in the cavity varies about 3.5°C between the sensors and about 2°C over the 2h test duration.



**Figure 6.5.** Temperature at several TA structure locations.

Other metrological data was not recorded and are obtained for this data analysis from the National Climatic Data Center [NCDC 2004] which is publishing compiled information from

official weather observing sites. At the Waco Regional Airport following atmospheric conditions were measured on 02.09.2004, 24:00 CDT: a dry bulb temperature of $T$=22.8°C, an air pressure of $p$=996.3 mbar and a relative humidity of 74%. The temperature of dry air matches well the temperature measured at the spiders. Using Stone's model to calculate the refraction angles (section 4.3.2), the refraction results for the six observed stars are shown in Figure 6.6 for an average wavelength of $\lambda$=550 nm and for the according observation time. Refraction angles of the observed stars are between 30 and 130 arcsec.



**Figure 6.6.** Calculated absolute refraction angles for observed stars with the model from Stone.

As illustrated in Figure 4.8, the atmospheric refraction causes the altitude of a star to appear higher in the sky than it actual is. When calculating the angular distance of two observed stars, an astrometric altitude *Alt* that is derived from catalogue values needs to be adjusted by the refraction angle *R*. The Altitude $Alt_{apparent}$, that is determined when observing through the atmosphere is yielded by:

$$Alt_{apparent} = Alt + R \qquad (6.2)$$

The angular distance between the observed stars can now be derived using equation (4.37) in section 4.3.3. The results for the observed stars are listed in Appendix D, Table D.3. The Altitude and Azimuth are calculated from catalogued equatorial coordinates. As their values change with observing time, Altitude and Azimuth positions are calculated for each observing time. The angular distance between the consequentially observed stars is shown with and without adjustment for refraction along with the amount of refraction.

The astrometric angular distances between the stars that are derived from star catalogue coordinates are compared to the rotated angular distances measured by the TA pointing sensors. The inertial rotations of the TA during the observations are measured by the three

gyroscopes and position differences on the imager field of views are taken into account by their centroid pixel location. Although HIPO data was recorded and evaluated (for section 6.2), only centroid data of the TA imagers are considered for this data analysis due to the high drift values, limited amount of recorded centroids and difficulties in time synchronization.

Two data sets are presented that were measured during different nights. The data of 03.09.2004 is more carefully analyzed and less noisy. Its data processing approach is exemplarily presented in this section. The detailed data analysis of the data of 31.08.2004 can be found in [Harms 2005c].

The main test sequence is conducted using the TA move command "Move-to-Boresight (MTBS)". The command has two options [Schmolke 2001b]: The *MTBS_CENTROID* command is used to move the TA such that the centroid of the specified area of interest (AOI) is positioned at the boresight. The *MTBS_INERTIAL* command is used to move the TA such that the specified IRF position is at the defined boresight location. Prior to test start, the boresight definitions in the imagers were set to the measured TARF origin pixel values. The *MTBS_INERTIAL* is typically used when a star is to be brought into the field of view which is beyond the field of view of any imager.

The centroid data selection was performed based on the FD motion status which delivers information about the control loop deviation, thus the actual FD position in regard to the commanded position. There are three parameters describing the motion status [Schmolke 2001b]:

|  |  |
|---|---|
| *transient* | The commanded move is still in process. |
| *settled* | The control loop deviation is outside the limit, i.e. telescope motion takes place but only due to overshoot control. |
| *locked* | The control loop deviation is inside the limit, i.e. no considerable telescope motion takes place. |

The limit is adjustable and was set during the testing to 1 arcsec RSS of all three axes. The FD position must be within the limit for a certain time (0.1 sec) to fulfill the condition "locked". The data selection using the FD motion status is shown in Figure 6.7 and Figure 6.8.
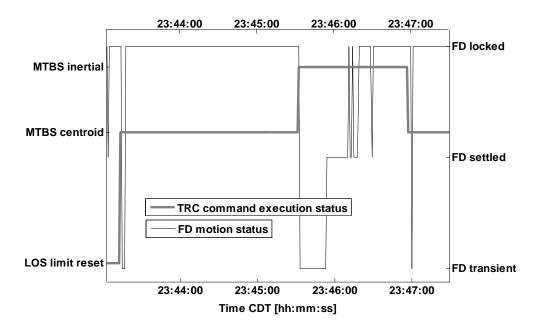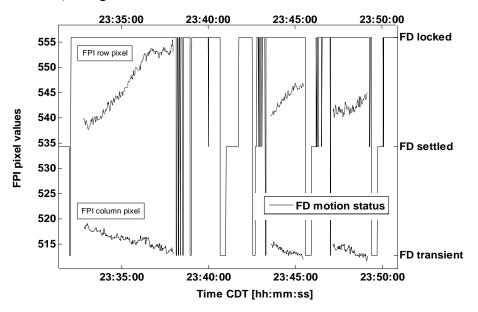
**Figure 6.7.** Processed tracker command (left y-axis, grey thick line) and FD motion status (right y-axis, black thin line) by showing exemplarily the move between η Cep and Polaris (Observation # 3 and #4).

First the command execution of the Tracker Controller (TRC) is observed (thick grey line in Figure 6.7). As soon as the *MTBS_CENTROID* command is executed, the TA moves the assigned centroid to the TA boresight position. While performing the move, the FD motion status (black thin line) becomes during the move first *transient*, then *settled* and finally *locked*. The centroid data that is recorded while the FD motion status is *locked* is selected for further analysis. Figure 6.8 shows an example of the selected FPI centroid data (row and column pixel values) along with the recorded FD motion status.



**Figure 6.8.** Selected FPI centroid data: column and row pixels (left y-axis, short data segments) along with the FD motion status (right y-axis, black line).

119

The data is used to assess the performance of these MTBS moves. The centroid data was selected approximately 5-10 sec after the move command was executed. The first three images of the selected centroid data are averaged and its centroid locations are shown in Figure 6.9 as diamonds. The mean value of the initial centroid positions of all 17 moves is at (515.0/540.7) and the standard deviation for column pixels is 1.2, respectively for row pixels 0.9. The centroids that deviate from the boresight location more than 2 pixels are selected more than 30-40 seconds after the move. In Appendix D, Table D.4 provides an overview of the length of the selected data sets and the time between the selected data sets.
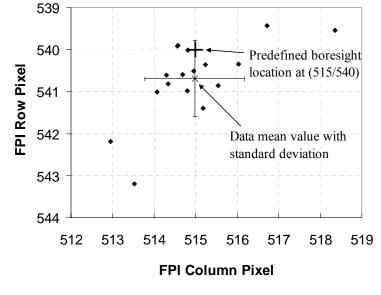


**Figure 6.9.** FPI centroid positions (♦) after *MTBS_CENTROID* for all 17 moves shown with mean value (x) and standard deviation for row and column pixels.

Although drift estimation took place prior to the test series, a strong residual drift is noticeable in the FPI centroid data (Figure 6.8). Whereas the centroid column pixels appeared to have a linear drift which changed magnitude and sign over the test duration, the drift of the row pixel values seemed to be sinusoidal. A non-linear curve fitting tool in MATLAB [Rousseau 2000] was used to determine the fit parameters. The detailed drift analysis can be found in [Harms 2005c].

For the column pixels, the amount of drift varies from -2.5 to +1 pixel/min. For drift removal, each of the measured drift values was used for the subsequent move. For the row pixels, a combined linear and sinusoidal curve fitting to data segments that show a full sine period yielded a drift of 1.4 pixel/min and a sinusoid with an average period of 5.2 min. and amplitude of 2.2 pixel. The linear drift value was used for the following drift removal. However, it will be shown that the row centroid drift is more crucial and the column drift has a minor influence for this sort of test evaluation.

The gyroscope data that was used to calculate the angular distance between the stars needed to be corrected using the drift values determined by the FPI centroid values. The recorded gyroscope quaternions representing the inertial TA rotations are first transformed into Euler Angles which are then corrected by the above determined drift values:

$$EL_c = EL + drift_{row} \cdot \Delta t \tag{6.3}$$

$$XEL_c = XEL - drift_{col} \cdot \Delta t \tag{6.4}$$

where *drift* is the amount of drift in the FPI row and column centroid values and $\Delta t$ is the time

between two selected centroid start times in seconds. The according data is listed in Appendix D, Table D.5.

In addition to removing the effect of residual bias drift of the gyroscopes, the data have to be compensated for remaining misalignment. The TA attitude change represented by the differential quaternion can be also expressed by a rotation about a rotation axis $\mathbf{r}_{misaligned}$ with a certain angle $\theta$ (equations (B.17) and (B.18) in Appendix B). Then, a rotation axis $\mathbf{r}$ can be established that accounts for the remaining misalignment:
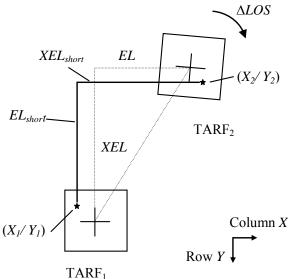
$$\mathbf{r} = \mathbf{A}_{new,FPI}\ \mathbf{A}_2^{-1}\ \mathbf{r}_{misaligned} \tag{6.5}$$

The remaining misalignment is composed by the inverse of matrix $\mathbf{A}_2$ (Table D.2 in Appendix D) that was implemented during the test and a new misalignment matrix $\mathbf{A}_{new,FPI}$ that is derived from the latest alignment matrix $\mathbf{A}_5$ (Table D.2 in Appendix D) and the misalignment angle from FPI alignment measurements described in [Meyer 2005]:

$$\mathbf{A}_{new,FPI} = \begin{pmatrix} 0.99997822 & 0.00560498 & -0.00348535 \\ -0.00558776 & 0.99997222 & 0.00493285 \\ 0.00351281 & -0.00491331 & 0.99998176 \end{pmatrix} \tag{6.6}$$

The Euler Angles can be obtained from the differential quaternions using equation (B.14), (B.15) and (B.16) in Appendix B which are then used to calculate the angular distances between the stars.

The effect of the drift and misalignment (especially on LOS rotations) can be reduced by shortening the time between the selected centroid data. It affects the calculation of the angular distance so little that it even can be neglected. Data were evaluated just before moving to the next target and just after the star was in the FPI field of view, later referred to as "short moves". The centroid pixel values and the time length between the moves are shown in Appendix D, Table D.4. As the star positions are now not located at the defined boresight, the centroid location on the FPI field of view has to be taken into account for calculating the angular distance between the stars (Figure 6.10). The differential quaternion expressing the attitude change between the two TA orientations TARF₁ and TARF₂, can be represented by the Euler Angles *EL* and *XEL*



**Figure 6.10.** Determination of angular distance between the observed stars for short moves.

which are then corrected for the centroid offset from the boresight. Similar to the calculation in section 4.3.3, the LOS component needs to be the last rotation angle in the sequence.

The angular distance is then calculated using Euler Angles $EL_{short}$ and $XEL_{short}$ from the short moves that are corrected for the centroid offsets:

$$EL_{short} = EL + 0.55 \ \ (Y_1 - Y_2)$$
(6.7)

$$XEL_{short} = XEL + 0.55 \ \ (X_2 - X_1)$$
(6.8)

when *EL* and *XEL* are the Euler angles obtained from the differential quaternion, the factor 0.55 is the image scale of the FPI in arcsec/pixel, $(X_1/\ Y_1)$ are the pixel coordinates of the star before the move and $(X_2/\ Y_2)$ after the move. The corrected Euler Angles and the resulting angular distances for the short moves are shown in Table D.6 in Appendix D.
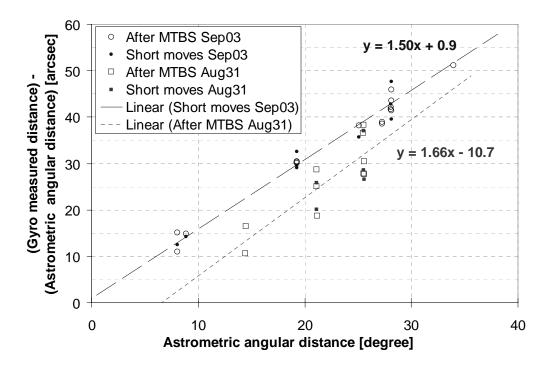
In Table 6.7, the angular distances measured by the gyroscopes and corrected for centroid offsets are compared for the different reduction methods. The table contains the raw data, the drift corrected data, the misalignment corrected data and the combined drift and misalignment corrected data. The drift and misalignment influence the angular distance measurement by tens of arcsec.

**Table 6.7.** Angular distances calculated from raw data, drift corrected data, misalignment corrected data and drift and misalignment corrected data.

| | Angular distances [arcsec] | | | | |
|---|---|---|---|---|---|
| Observation # | Raw data | Drift corrected | Misalignment corrected | Misalignment, drift corrected | Short moves |
| 1-2 | 101252.2 | 101238.1 | 101253.8 | 101239.7 | |
| 2-3 | 101233.6 | 101248.2 | 101223.3 | 101237.9 | 101236.0 |
| 3-4 | 101247.3 | 101242.6 | 101247.2 | 101242.6 | 101244.3 |
| 4-5 | 98167.7 | 98176.6 | 98161.4 | 98170.3 | |
| 5-6 | 28947.3 | 28933.4 | 28947.1 | 28933.3 | |
| 6-7 | 28923.7 | 28929.3 | 28923.7 | 28929.3 | 28930.8 |
| 7-8 | 98164.1 | 98155.7 | 98178.6 | 98170.2 | |
| 8-9 | 69359.4 | 69363.7 | 69359.4 | 69363.6 | 69362.5 |
| 9-10 | 101151.9 | 101141.7 | 101159.5 | 101149.3 | |
| 10-11 | 101145.0 | 101150.0 | 101145.0 | 101150.0 | 101150.6 |
| 11-12 | 69365.1 | 69358.9 | 69370.2 | 69364.1 | 69366.2 |
| 12-13 | 69357.9 | 69364.0 | 69357.8 | 69364.0 | 69363.4 |
| 13-14 | 24457.7 | 24466.0 | 24449.6 | 24457.9 | |
| 14-15 | 122370.3 | 122361.4 | 122370.2 | 122361.3 | |
| 15-16 | 32040.3 | 32044.2 | 32040.3 | 32044.1 | 32043.5 |
| 16-17 | 90317.0 | 90321.3 | 90316.9 | 90321.3 | 90318.8 |

When the rotation contains a large LOS component, the effect of misalignment is significant (i.e. move between observation numbers 2-3). The last column shows data that are derived from the short moves. The drift and misalignment corrected data agrees well with the short move data.

The deviations between the apparent angular distances derived from the catalogue values (Table D.3 in Appendix D) and the angular distances derived from the gyroscope and imager centroid data (Table 6.7) increase linearly with the distance of the observed stars. The results are shown in Figure 6.11. In addition, the results from the test series on 31.08.2004 are shown although fewer moves were executed and drift conditions were bad during the test. Linear curve fits are added for both data sets. The angular distances calculated from the short moves compare well to the drift and alignment corrected values.



**Figure 6.11.** Deviation of measured angular distances between stars and their apparent angular distance determined from catalogue values. The data set from Sept 3rd is less noisy than the data set from Aug 31st. The data is compared to the angular distances derived from short moves which represent quick rotations that provide the least noisy data.

Initially, the test evaluation was intended to gain information about the structural bending of the telescope. When looking at angular distances between stars that are separated largely, the angular distance is only affected when the EL component changes largely. Gravity deformation effects the pointing mainly in the XEL direction as predicted by the finite element calculations (see section 3.4.2). Also, the gyroscope's scale factor error should be a small effect. Vendor information indicates that, depending on temperature, scale factor errors are expected to be less than 3 arcsec over the operational elevation range. During later testing,

it was noted that the gyroscope calibration parameters were assigned to the wrong axes. As this is performed within the TA software the effect cannot be taken out via post-processing. Having the wrong temperature dependent scale factor modeling can cause deviations in angular separation as is was measured.

## 6.4 Recommendations for automated alignment measurements and data processing

The sensor alignment approach described in chapter 3 suggests performing consecutive alignment maneuvers on the sky. The alignment between the sensors and the focal plane could change over time due to demounting of the optical components or the sensors themselves, and a semi-autonomous method for the alignment is pursued. As well, systematic pointing errors that are measured to be larger than the pointing accuracy requirement (Table 2.2) imply the need for realignment of the sensors.

This section suggests recommendations in regard to an automated alignment process on the basis of the proposed alignment maneuvers in Table 3.4 and the data analysis that was performed during the data evaluation of the on sky tests in 2004. An example for an automated calibration system applied on attitude control sensors of satellites can be found in [Sedlak 2004]. Apart from the pure calibration measurements and their data analysis, it includes the identification of the need for new calibration and the scheduling of the calibration maneuvers into other planned spacecraft events. This can be considered for the calibration maneuvers for the SOFIA telescope once full operational capability is deployed. This section gives recommendations for an initial stage of automating the sensor alignment procedure and is arranged in the according process steps. They are summarized in Figure 6.12. The steps that are already or could be automated are denoted by (A), whereas the steps that need manual interaction are denoted by (M).

**Establishing the alignment maneuver sequence**
Depending on the identified sensor alignment that need to be repeated, a consecutive sequence of the maneuvers need to be followed. It is outlined in Table 3.4. Gyroscope drift estimation should be performed immediately before the alignment measurements and is automatically performed when the telescope is commanded to track on a star. If a series of alignment maneuvers are performed, the tracking, and thus the gyroscope drift estimation, should be repeated hourly. As the alignment accuracy improves significantly when the maneuvers are repeated (section 3.5), a number of at least six maneuvers is recommended. More than ten maneuvers do not improve the accuracy greatly.

**Selecting target stars for the alignment measurements**

For the alignment measurements from ground it is recommended to use circumpolar stars that are close to the North Celestial Pole. This has the advantage that the telescope does not hit its motion limits in EL and XEL while being inertially stabilized and observing the same stars during an entire night. For elevation dependent measurements, non-circumpolar stars have to be selected that are in the telescope field of view at the same aircraft heading. The star availability depends on the observing location and time. In [Meyer 2003] a compilation of available stars is presented that has to be adjusted for the new latitude and longitude of the present aircraft position. A fair amount of star catalogues and astrometric software are available as the ones used in section 6.3. Target stars for the FFI and WFI alignment measurements should have a visual magnitude of 7 or brighter, the alignment measurements with the FPI and HIPO can be fainter for the desired exposure times described in the next paragraph. For automating the star selection, a catalogue of desired target stars can be established that is customized for the alignment measurements.

| Identify need for re-alignment and layout according maneuvers (M) |
| --- |

| **Select target stars** <br> Target star catalogue depending on observing location and time (A) |
| --- |

| **Perform alignment measurements** <br> Monitor environmental conditions (A) <br> Execute commands (M) <br> Assess data and maneuver quality (A) |
| --- |

| **Extract and analyze data** <br> Extract data (A) <br> Import data into analysis software (A) <br> Synchronize data (A) <br> Select data segments (A) <br> Correct data for residual drift (A) <br> Analyze data and calculate alignment matrix (A) |
| --- |

| **Verify implementation** <br> Implement alignment matrix (M) <br> Repeat simplified alignment maneuver for verification (A) <br> Repeat simplified data analysis (A) <br> Accept alignment (M) |
| --- |

**Figure 6.12.** Alignment steps that could be automated (A) and that need to be performed manually (M).

**Performing the alignment measurements**
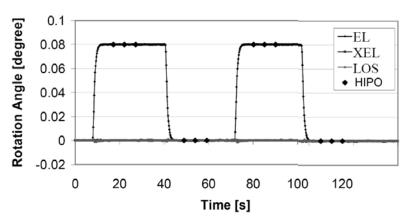
Before and also during the alignment maneuvers, predefined environmental conditions should be fulfilled to assure reasonable measurement results. Especially when automating the measurements and the data processing, these conditions should be monitored permanently and include: Atmospheric seeing, the gyroscope drift conditions and the telescope vibrations due to its subsystems and due to external disturbances such as aircraft ground support systems. The TA is particularly exposed to the external perturbations because the VIS is not fully operational as there is no pressure difference between cabin and cavity on ground as it would be on airborne operation. The conditions can be monitored by means of TA housekeeping data and the raw image data.

The atmospheric seeing is reduced taking images with an exposure time as long as possible but avoiding saturation of the CCD pixels. Alternatively or in addition, multiple images can be averaged. In the beginning of the alignment test series, the optimal exposure time need to

be determined by inspecting raw images from the imagers and HIPO. A good rule of thumb is when the measured intensity of the observed star is about two-third of its intensity limit.

The data analysis can be greatly simplified when the recording of the HIPO images is carefully timed. An example is shown in Figure 6.13. The simultaneous rotation angles are shown for two alignment maneuvers about the EL axis. Three HIPO images are recorded (indicated by diamonds) after the FD motion is finished.



**Figure 6.13.** Example for alignment maneuvers and image acquisition with HIPO.

Telescope vibrations can be monitored and assessed by the motion status parameters of the FD controller. It evaluates the amount of the present control deviation (see section 6.3 and next paragraph for further details on the parameters).

**Extracting and analyzing the measurement data**

A set of variables needs to be defined for extraction that includes all the TA housekeeping data used in the subsequent data reduction process. After the selected data set recorded by the EGSE and DCC is available, they need to be imported and synchronized along with the HIPO image data into common analysis software. The time synchronization can be performed via the UTC timestamps that are recorded together with the data. As mentioned in the previous section, it is desired that the recording of the HIPO images is timed with the maneuver execution. Various TA housekeeping data can be used to identify the TA status, i.e. the command status and time and the FD motion status which describes if the control deviation is for an extended period within a certain limit. This status information can be applied to automatically select the data segments that are then used for calculating the misalignment correction. An example for this data selection process is described in section 6.3. The selected data is then processed in the common analysis software in regard to centroid calculation (semi-automation described in section 4.3.1), averaging, residual drift correction and finally the calculation of the alignment matrix.

**Implementing and verifying the alignment corrections**

The calculated alignment matrix is then implemented into the software and verified by means of simplified alignment maneuvers and according data reduction. When the alignment results are satisfying, the implemented alignment matrix can be accepted.

# 7 Conclusions

The present work focuses on the pointing control system of the SOFIA telescope. During science observations, the pointing control is achieved by an array of sensors including the three imagers, the gyroscopes, as well as the accelerometers and during alignment and calibration of the telescope assembly by the reference instrument HIPO mounted on the focal plane. Each of the sensors is associated with a reference frame. Sensor errors as well as external perturbations can be compensated within a theoretical concept that is established based on these reference frames. The dissertation develops the alignment strategy for the reference frames. Using measurement data, the alignment maneuvers are analyzed and the sensor performance is characterized.

The proposed alignment strategy describes the alignment maneuvers and their required sequence in order to measure the misalignment between the gyroscopes, the imagers and the focal plane. The reference at the focal plane is the reference instrument HIPO. Algorithms are derived to calculate the matrices that need to be implemented into the TA software compensating the measured sensor misalignments. The alignment strategy incorporates as well the compensation concept for pointing errors due to static structural deformation and combines it with the alignment measurements. The alignment accuracy can be improved by repeating the maneuevers and recording multiple images at the alignment positions and is estimated by means of error propagation.

A set of data reduction techniques is presented that is used for the analysis of the sensor performance and alignment measurements. This includes the data reduction for the gyroscopes and for astrometric measurements with the imagers and HIPO. Theoretical predictions of the gyroscope noise characteristic are given based on the manufacturer calibration results.

The alignment measurements could be partially performed during the first on sky test series in 2004. The sensor misalignment is measured by the sensors themselves and any sensor errors are interpreted as misalignment. This includes also external disturbances that appear in the sensor signals and that are caused by TA subsystems or aircraft support systems. In order to reduce the alignment measurement data correctly, the characteristics of the sensor data have

to be well understood. Due to the fact that all rotations that are commanded within the inertial TA stabilization system are sensed and fed back by the gyroscopes, their sensor signals evaluation is particularly significant. Therefore, a major part of this work is dedicated to the sensors and system effects measured by the gyroscopes. During the first on sky tests, the gyroscope signals were affected by high noise and drift values. Within this work measurements were performed to assess their characteristic and their TA integrated performance.

The results of the conducted gyroscope stability measurements show that all three fiber optic gyroscopes integrated in the TA system perform as specified. The influence of ground support equipment and vibration isolation subsystems of the TA was assessed with long term tests while these systems were turned on step by step. Single frequencies could be identified which are excited by the activated equipment that are above 30 Hz. Below 30 Hz a high noise increase is noticeable when people are present on the aircraft which lead to previously measured high noise figures.

Comparing the measured angular rates with the theoretical values of Earth's rotation rate indicates that the absolute value of the gyroscope biases is about 0.19°/h. The exact bias values of each gyro are difficult to assess as heading measurement errors have a great effect. However, the stability analysis of the gyroscopes does not depend on the constant bias errors. Assuming that the exact bias error is known, the angular error over time is smaller than 20 arcsec even for the longest evaluated test duration of four hours.

The noise analysis of the gyroscopes was performed via Power Spectral Density and Allan Variance analysis. Both methods revealed that the ARW or the white noise on the measured angular rates lies within the specified values even with the gyroscopes integrated into the TA system. Certain frequencies are measured disturbing the noise analysis. They are induced by ground support and TA subsystems and could be identified. The step by step activation of the suspension assembly can be verified with the PSD results. The activation of the oil pump system leads to an increase of the overall noise and excites certain frequencies. The VIS uncaging isolates vibrations in XEL and LOS larger than 3 Hz and leads to an amplitude increase of its natural frequency at 2.3 Hz. Releasing the FD brakes and allowing the TA to float open loop isolates residual vibrations above 2 Hz. At the same time, low frequency content rises and a 1 Hz frequency is additionally measured. The outstanding frequencies at 0.7 and 1.3 Hz are not isolated through the RIS and are possibly introduced through the spherical sensors. The noise analysis via Allan Variance shows as well that the bias stability values of the integrated gyroscopes fulfill the specification. A 20 min. oscillation was seen on the LOS gyro as already documented causing an apparent higher rate random walk and rate ramp on the Allan Variance curve.

The first on sky observations with the SOFIA telescope were performed in 2004. In addition to the functional testing of the various TA subsystems that interacted together for the first time, a variety of alignment measurements, structural flexure measurements and pointing measurements were performed. The test series was accomplished without a reflecting coating

applied to the primary mirror, which was compatible with the bright stars selected for this work. From an astronomical observing point of view, the environmental conditions were not optimal considering the high outside temperatures and humidity.

The gyroscope alignment procedure was performed iteratively and measurements revealed an initial misalignment for the EL- and XEL- axes of 1° and for the LOS-axis of about 20 arcmin. During these measurements, the alignment procedure was not thoroughly in place and minor errors affected the alignment calculation. Despite that, the calculated and implemented alignment matrix only left a remaining misalignment error for the EL- and XEL-axes of 0.1° and for the LOS-axis of 0.4 arcmin. Elevation depending measurements were performed by observing stars at different elevations simultaneously in the FPI, the FFI and HIPO. Differential flexures are calculated for the FFI and FPI with respect to the focal plane. It is measured that the boresight position in the FPI relative to that in HIPO changes about 1.1 arcsec in XEL for an elevation change from 23° to about 60°. The effect in elevation is less than 0.27 arcsec. Over the same elevation range, the boresight of the FFI changes relative to that in HIPO by about 9 arcsec in XEL and about 8 arcsec in EL. Finite element calculations predict much less flexure for the FPI, whereas the FFI predictions agree reasonably well.

The star observations over the elevation range permitted evaluation of absolute pointing performance. Initially, the test evaluation was intended to gain information about the structural bending of the telescope, but it was shown that this is of minor influence for this sort of test evaluation. The star positions are well known on the sky and published in star catalogues. After correcting for atmospheric refraction, the expected apparent angular separations between these stars can be calculated for the ground observing location. These angles are then compared to the measured rotation angles which were comprised of the gyroscope information and the small correction from the image position in the sensor. After the effects of misalignment and the residual bias drift of the gyroscope have been removed, it is shown that the deviation between the gyroscopic measured angles and the true separation angles increases linearly with the relative angular distance of the observed stars. For a maximum measured angular separation between two stars of 34°, a residual deviation between the measured gyroscopic and calculated astrometric angular distance is about 50 arcsec. This error might be traced back to a wrong axes calibration assignment for the gyroscopes that was implemented during the tests.

Eventually, recommendations are given on automating the alignment measurements. The recommendations are based on the proposed alignment strategy, the elaborated data reduction methods, the conducted experiments and the analyzed data. Within the scope of this work, several scripts were developed to import TA housekeeping data into MATLAB, to synchronize them and analyze sensor performance and alignment measurements. Recently, in preparation for the next alignment test series, automated evaluation of the gyroscope alignment measurements are prepared in collaboration with the HIPO instrument team.

# A   Pointing stability budget

**Table A.1.**   Pointing stability budget telescope subsystems [Kärcher 2000b].

| Telescope subsystems | | Error Contribution [arcsec] |
|---|---|---|
| 1. | **Tracking Loop** | |
| 1.1 | Tracker stability (imagers etc.) | 0.05 |
| 1.2 | Aliasing | 0.03 |
| 1.3 | Gyro random walk | 0.05 |
| 1.4 | Gyro drift estimation | 0.03 |
| | **Total RSS** | **0.08** |
| | | |
| 2. | **Inertial Stabilization Loop** | |
| 2.1 | Telescope disturbances | |
| 2.1.1 | Cradle Couplings (coarse drive, bearing friction, seal friction etc.) | 0.04 |
| 2.1.2 | Balancer Drives (stick/slip etc.) | 0.02 |
| 2.1.3 | Overall Imbalance (mismatch CoG etc.) | 0.02 |
| 2.2 | Gyro resolution | 0.01 |
| 2.3 | Fine Drive (Torquer ripple etc.) | 0.07 |
| 2.4 | Fine Drive Controller Noise | 0.03 |
| | **Total RSS** | **0.09** |
| | | |
| 3. | **Secondary Mirror Assembly** | |
| 3.1 | SMA position stability | 0.05 |
| | **Total RSS** | **0.05** |
| | | |
| 4. | **Alignment** | |
| 4.1 | Dynamic Misalignment SI – FPI | 0 |
| 4.2 | Coordinate transformation error FPI – Gyro | 0.02 |
| 4.3 | Coordinate transformation error Gyro –Spherical Sensor | 0.02 |
| | **Total RSS** | **0.03** |
| | | |
| **Total RSS telescope subsystems (1.-4.)** | | **0.14** |

**Table A.2.** Pointing stability budget aircraft environment [Kärcher 2000b].

| Aircraft Environment | | Error contribution [arcsec] | | | |
|---|---|---|---|---|---|
| | | Freq. 0-10Hz | Freq. 0-35Hz | Freq. 0-70Hz | Freq. 0-110Hz |
| **Total RSS telescope subsystems (1.-4.)** | | **0.14** | **0.14** | **0.14** | **0.14** |
| 5. | **Flexible Body Compensator** | | | | |
| 5.1 | FBC Sensors (accelerometers) | 0.04 | 0.04 | 0.04 | 0.04 |
| 5.2 | FBC Actuators | | | | |
| 5.2.1 | Fine Drive | 0.07 | 0.07 | 0.07 | 0.07 |
| 5.2.2 | SMA | 0 | 0.05 | 0.05 | 0.05 |
| 5.3 | FBC Controller (estimation error) | 0.04 | 0.04 | 0.04 | 0.04 |
| | **Total RSS** | **0.09** | **0.10** | **0.10** | **0.10** |
| 6. | **Thermal Effects** | | | | |
| 6.1 | Focal Plane Imager | 0 | 0 | 0 | 0 |
| 6.2 | Tertiary Mirror | 0.02 | 0.02 | 0.02 | 0.02 |
| | **Total RSS** | **0.02** | **0.02** | **0.02** | **0.02** |
| 7. | **Aircraft Vibrations** | | | | |
| 7.1 | 0-10 Hz | 0.16 | 0.16 | 0.16 | 0.16 |
| 7.2 | 10-30 Hz | | 0.25 | 0.25 | 0.25 |
| 7.3 | 30-70 Hz | | | 0.09 | 0.09 |
| 7.4 | 70-110 Hz | | | | 0.04 |
| | **Total RSS** | **0.16** | **0.30** | **0.31** | **0.31** |
| 8. | **Aerodynamic Loads** | | | | |
| 8.1 | 0-10 Hz | 0.30 | 0.30 | 0.30 | 0.30 |
| 8.2 | 10-30 Hz | | 0.40 | 0.40 | 0.40 |
| 8.3 | 30-70 Hz | | | 0.49 | 0.49 |
| 8.4 | 70-110 Hz | | | | 0.85 |
| | **Total RSS** | **0.30** | **0.50** | **0.70** | **1.10** |
| **Commands** | | | | | |
| 9. | **Tracking Commands** | | | | |
| 9.1 | Non-inertial tracking | 0 | 0 | 0 | 0 |
| | **Total RSS** | **0.00** | **0.00** | **0.00** | **0.00** |
| **Total RSS pointing error (1.-9.)** | | **0.38** | **0.61** | **0.79** | **1.16** |

# B  Attitude representations

## B.1  Notation and definitions

The attitude of a rigid body expressed in a reference frame can be represented in following four ways [Moik 2000, Wertz 1978].

### B.1.1  Direction Cosine Matrix (DCM)

The DCM is an orthonormal transformation matrix defined by nine parameters. Three parameters are independent. The attitude matrix **A** of the body reference frame (BF) with respect to a reference frame (RF) is composed with the three unit vectors of the BF expressed in the RF:

$$\mathbf{A}_{BF,RF} = \begin{pmatrix} u_{1,BF,RF} & v_{1,BF,RF} & w_{1,BF,RF} \\ u_{2,BF,RF} & v_{2,BF,RF} & w_{2,BF,RF} \\ u_{3,BF,RF} & v_{3,BF,RF} & w_{3,BF,RF} \end{pmatrix} \tag{B.1}$$

For orthonormal matrices:

$$\mathbf{A}^{-1} = \mathbf{A}^{T} \tag{B.2}$$

The matrix transforms a vector **r** from the RF to the BF with:

$$\mathbf{r}_{BF} = \mathbf{A}_{BF,RF}\mathbf{r}_{RF} \tag{B.3}$$

### B.1.2  Euler angles

The orientation of the BF with respect to the RF is described by three consecutive rotations about at least two of the BF axes. Both reference frame coincide at begin, then, the rotations take place about the new BF axes. There are 12 different conventions of Euler angles according to the possible rotation axis combinations. The DCM of the complete rotation is composed with the three single axis rotation matrices.

For a rotation sequence of body axis 1-2-3 with Euler angles ($\alpha$, $\beta$, $\gamma$), the according DCM is composed with:

$$\mathbf{A}_{BF,RF} = \begin{pmatrix} \cos\gamma & \sin\gamma & 0 \\ -\sin\gamma & \cos\gamma & 0 \\ 0 & 0 & 1 \end{pmatrix} \begin{pmatrix} \cos\beta & 0 & -\sin\beta \\ 0 & 1 & 0 \\ \sin\beta & 0 & \cos\beta \end{pmatrix} \begin{pmatrix} 1 & 0 & 0 \\ 0 & \cos\alpha & \sin\alpha \\ 0 & -\sin\alpha & \cos\alpha \end{pmatrix} \tag{B.4}$$

### B.1.3   Rotation axis and angle

This attitude representation is based on Euler's Theorem. Any sequence of rotations or equivalent rotation matrix can be expressed by a single rotation about a fixed axis. The DCM is given in terms of a unit vector along the "Euler axis" $\mathbf{r}$ and the rotation angle $\theta$. To reduce redundancy the rotation vector is multiplied by the rotation angle yielding three simultaneous rotation angles about the body axes.

### B.1.4   Quaternions

A quaternion is a hypercomplex number with three imaginary parts $q_1$, $q_2$, $q_3$ and a real part $q_4$. The quaternion $q_{RF2,RF1}$ describes a rotation from RF 1 to RF 2. There are three independent parameters with following property:

$$q_{RF2,RF1} = \begin{pmatrix} q_1 \\ q_2 \\ q_3 \\ q_4 \end{pmatrix}; \qquad |q| = q_1^2 + q_2^2 + q_3^2 + q_4^2 = 1 \tag{B.5}$$

The quaternion components are composed with the components of the unit vector $\mathbf{r}$ describing the rotation axis and the rotation angle $\theta$:

$$\begin{aligned} q_1 &= r_u \sin(\theta/2) \\ q_2 &= r_v \sin(\theta/2) \\ q_3 &= r_w \sin(\theta/2) \\ q_4 &= \cos(\theta/2) \end{aligned} \tag{B.6}$$

The inverse quaternion is calculated with:

$$q^{-1} = \begin{pmatrix} -q_1 \\ -q_2 \\ -q_3 \\ q_4 \end{pmatrix} \tag{B.7}$$

If all four elements of the quaternion are inverted, both quaternions represent the same attitude change:

$$q = \begin{pmatrix} q_1 \\ q_2 \\ q_3 \\ q_4 \end{pmatrix} = \begin{pmatrix} -q_1 \\ -q_2 \\ -q_3 \\ -q_4 \end{pmatrix} \tag{B.8}$$

## B.2 Relation between attitude representations

A complete description on converting the four different attitude representations is given in [Moik 2000]. Only the conversions used within this work are listed in the following.

### DCM from Quaternions

$$\mathbf{A} = \begin{pmatrix} q_4^2 + q_1^2 - q_2^2 - q_3^2 & 2(q_1 q_2 + q_4 q_3) & 2(q_1 q_3 - q_4 q_2) \\ 2(q_1 q_2 - q_4 q_3) & q_4^2 - q_1^2 + q_2^2 - q_3^2 & 2(q_2 q_3 + q_4 q_1) \\ 2(q_1 q_3 + q_4 q_2) & 2(q_2 q_3 - q_4 q_1) & q_4^2 - q_1^2 - q_2^2 + q_3^2 \end{pmatrix} \tag{B.9}$$

### Quaternions from DCM

There are in total four different ways to convert quaternions into the DCM. Here, only one possibility is shown. See [Moik 2000] for a complete list. Due to equation (B.8) there are two possible quaternions expressing the same DCM.

$$
\begin{aligned}
q_4 &= \pm \frac{1}{2} \sqrt{1 + a_{11} + a_{22} + a_{33}} \\
q_1 &= \frac{1}{4 q_4}(a_{23} - a_{32}) \\
q_2 &= \frac{1}{4 q_4}(a_{31} - a_{13}) \\
q_3 &= \frac{1}{4 q_4}(a_{12} - a_{21})
\end{aligned}
\tag{B.10}
$$

### Euler angles ($\alpha,\ \beta,\ \gamma$) sequence 1-2-3 from Quaternions

$$\alpha = \arctan \frac{2(q_4 q_1 - q_2 q_3)}{q_4^2 - q_1^2 - q_2^2 + q_3^2} \tag{B.11}$$

$$\beta = \arcsin 2(q_4 q_2 + q_1 q_3) \tag{B.12}$$

$$\gamma = -\arctan \frac{2(q_4 q_3 - q_1 q_2)}{q_4^2 + q_1^2 - q_2^2 - q_3^2} \tag{B.13}$$

**Euler angle ($\alpha$, $\beta$, $\gamma$) sequence 1-2-3 from Rotation axis and angle**

$$\beta = \arcsin\left(r_v \sin\varphi + r_u r_w (1 - \cos\varphi)\right) \tag{B.14}$$

$$\alpha = -\arctan\frac{r_v r_w (1 - \cos\varphi) - r_u \sin\varphi}{\cos\varphi + r_w^2 (1 - \cos\varphi)} \tag{B.15}$$

$$\gamma = -\arctan\frac{r_u r_v (1 - \cos\varphi) - r_w \sin\varphi}{\cos\varphi + r_u^2 (1 - \cos\varphi)} \tag{B.16}$$

**Rotation axis and angle from Quaternions**

$$r = \frac{1}{\sin\dfrac{\theta}{2}} \begin{bmatrix} q_1 \\ q_2 \\ q_3 \end{bmatrix} \tag{B.17}$$

$$\theta = 2\arccos(q_4) \tag{B.18}$$

**Simultaneous rotation angles $\theta_u$, $\theta_v$, $\theta_w$ about body axes u, v, w from Quaternions**
$\theta$ is the total rotation angle about the fixed rotation axis.

$$\theta = \sqrt{\theta_u^2 + \theta_v^2 + \theta_w^2} = 2\arccos(q_4) \tag{B.19}$$

$$\theta_u = \frac{q_1\theta}{\sin(\theta/2)} \tag{B.20}$$

$$\theta_v = \frac{q_2\theta}{\sin(\theta/2)} \tag{B.21}$$

$$\theta_w = \frac{q_3\theta}{\sin(\theta/2)} \tag{B.22}$$

## B.3  Rotation sequences

**DCM**
Rotation sequences are expressed by multiplying matrices that describe single rotations. Two successive rotations from RF 1 to RF 2 given by $\mathbf{A}_{RF2,RF1}$ and RF 2 to RF 3 given by $\mathbf{A}_{RF3,RF2}$ are described with a rotation from RF 1 to RF 3 with:

$$\mathbf{A}_{RF3,RF1} = \mathbf{A}_{RF3,RF2}\mathbf{A}_{RF2,RF1} \tag{B.23}$$

The attitude difference between an initial orientation $\mathbf{A}_{RF2,RF1}$ and an end orientation $\mathbf{A}_{RF3,RF1}$ is given by:

$$\mathbf{A}_{RF3,RF2} = \mathbf{A}_{RF3,RF1}\mathbf{A}_{RF2,RF1}^{-1} \tag{B.24}$$

**Quaternions**

The successive rotations $p_{RF2,RF1}$ and $q_{RF3,RF2}$ can be combined to a quaternion $r_{RF3,RF1}$ by quaternion multiplication. The multiplication rule that is applied within the SOFIA documentation is left to right and is given by:

$$r_{RF3,RF1} = \begin{pmatrix} p_1 \\ p_2 \\ p_3 \\ p_4 \end{pmatrix}_{RF2,RF1} \begin{pmatrix} q_1 \\ q_2 \\ q_3 \\ q_4 \end{pmatrix}_{RF3,RF2} = \begin{pmatrix} p_1 q_4 + p_2 q_3 - p_3 q_2 + p_4 q_1 \\ - p_1 q_3 + p_2 q_4 + p_3 q_1 + p_4 q_2 \\ p_1 q_2 - p_2 q_1 + p_3 q_4 + p_4 q_3 \\ - p_1 q_1 - p_2 q_2 - p_3 q_3 + p_4 q_4 \end{pmatrix} \tag{B.25}$$

The attitude difference between an initial orientation $p_{RF2,RF1}$ and an end orientation $r_{RF3,RF1}$ is given by:

$$p_{RF2,RF1} = r_{RF3,RF1}q_{RF3,RF2}^{-1} \tag{B.26}$$

# C   Reference frame definitions

## C.1  Telescope reference frames

### C.1.1   Body-fixed telescope reference frames

**Telescope Assembly Reference Frame (TARF)**

TARF is a reference frame fixed to the rotating part of the telescope assembly. It represents the telescope pointing for a perfectly aligned and rigid telescope. The TARF axes are the elevation, the cross-elevation and line-of-sight axes.

| Origin | Center of bearing | |
|---|---|---|
| Axes definition | U | along centerline of Nasmyth tube towards cabin side |
| | V | perpendicular to U- and W-axis as defined by right hand rule |
| | W | perpendicular to primary mirror towards secondary mirror |

**Gyroscope Reference Frame (GYRF)**

The sensing axes of the three gyroscopes build up the GYRF and are mounted in such a way that their axes correspond to the TARF axes. GYRF matches TARF for a perfectly aligned and rigid telescope.

| Origin | Center of bearing | |
|---|---|---|
| Axes definition | U | defined by sensing axis of gyroscope mounted corresponding to TARF U–axis |
| | V | defined by sensing axis of gyroscope mounted corresponding to TARF V-axis |
| | W | defined by sensing axis of gyroscope mounted corresponding to TARF W-axis |

**Principal Axes of Inertial Reference Frame (PAIRF)**

The TA is controlled in its principal axes of inertia and the commanded torque must be applied in these axes to avoid cross-coupling. Due to the configuration of the primary mirror and the balancing weights, the principal axes of inertia differ from TARF. The PAIRF U- and W-axis are rotated 16° about the V-axis. The V-axes of both reference frames coincide.

| | | |
|---|---|---|
| Origin | Center of bearing | |
| Axes definition | U | in TARF UW-plane, pointing towards upper part of balancing plate |
| | V | corresponds to TARF V-axis |
| | W | perpendicular to U- and V-axis as defined by right hand rule |

**Inner Cradle Reference Frame (ICRF)**

The ICRF is fixed to the telescope's inner cradle. It provides the reference when the telescope is locally stabilized. The spherical sensors provide the attitude information between the telescope orientation (TARF) and the inner cradle. For a perfectly aligned and rigid telescope, TARF and ICRF match when the telescope is centered within the physical motion range of the FD.

| | | |
|---|---|---|
| Origin | Center of bearing | |
| Axes definition | U | perpendicular to CD bearing plane towards cabin side |
| | V | in bearing plane horizontal out the left side of the aircraft |
| | W | in bearing plane towards Zenith |

**Outer Cradle Reference Frame (OCRF)**

The OCRF is fixed to the telescope's outer cradle. It matches the ICRF when the telescope is pointing towards the Zenith (CD elevation of 90°).

| | | |
|---|---|---|
| Origin | Center of bearing | |
| Axes definition | U | perpendicular to CD bearing plane towards cabin side |
| | V | in bearing plane horizontal out the left side of the aircraft |
| | W | in bearing plane towards Zenith |

### C.1.2   Inertial telescope reference frame

**Inertial Reference Frame (IRF), telescope centered, inertial**

IRF is established when the gyroscopes are turned on. Then, IRF is identical to the initial orientation of TARF until the first rotation of the telescope occurs. The initial orientation of TARF is yielded by flexure and misalignment corrected GYRF.

| | | |
|---|---|---|
| Origin | Center of bearing | |
| Axes definition | U | initial TARF u-axis |
| | V | initial TARF v-axis |
| | W | initial TARF w-axis |

### C.1.3   Imager reference frames

**Imager Pixel Reference Frame (for FPI, FFI and WFI)**
The pixel coordinate system is defined by the image that is produced by the camera CCD chip and its read-out electronics.

| | | |
|---|---|---|
| Origin | Pixel location (0/0) in camera image | |
| Axes definition | X | column axis |
| | Y | row axis |

**Imager Reference Frame (XYRF, XY stands for FPI, FFI and WFI)**
The imager reference frames are defined by the center pixel location of the CCD chip and its pixel row and column axes.

| | | |
|---|---|---|
| Origin | Center of CCD chip, fixed to the camera head | |
| Axes definition | U | positive towards increasing column pixel numbers (X) |
| | V | positive towards increasing row pixel numbers (Y) |
| | W | perpendicular to U and V |

**Imager Mounting Flange Reference Frame (XYMFRF, XY stands for FPI, FFI and WFI)**
The mounting flange provides the imager interface to the TA. For a perfectly rigid and aligned telescope, its axes coincide with the TARF axes.

| | | |
|---|---|---|
| Origin | Center of mounting flange, fixed to the mounting flange | |
| Axes definition | U | corresponds to U-TARF axis |
| | V | corresponds to V-TARF axis |
| | W | corresponds to W-TARF axis |

## C.2 Science instrument reference frames

**Science Instrument Reference Frame (SIRF)**

The SIRF is a pixel coordinate system at default. It is based on the detector layout of the science instrument.

| | | |
|---|---|---|
| Origin | Pixel location (0/0) | |
| Axes definition | X | along x-axis of SI |
| | Y | along y-axis of SI |

**Science Instrument Mounting Flange Reference Frame (SIMFRF)**

The SIMFRF is used to provide the mounting orientation information of the SI. Its position is nominal when the TA is parked at 40° elevation. The X- and Y-axis intersect the dowel pin locations. The Z-axis is offset to the TARF U-axis by 84mm.

| | | |
|---|---|---|
| Origin | Center of Instrument Mounting Flange (IMF) | |
| Axes definition | X | when TA parked at 40°, pointing horizontal out the left side of aircraft intersecting dowel pins |
| | Y | when TA parked at 40°, pointing up intersecting dowel pins |
| | Z | parallel to centerline of Nasmyth tube toward cabin side |
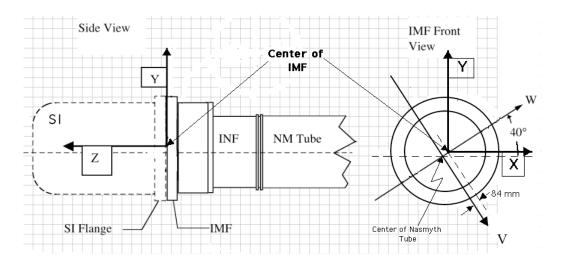


**Figure C.1.** Definition of SIMFRF (X,Y,Z) [Webb 2004].

## C.3 Aircraft fixed reference frames

### C.3.1 Aircraft System Reference Frame (ASRF)

B747 standard coordinate systems

| | |
|---|---|
| Origin | It is located 90 inches [2286 mm] in negative X direction from the tip of the nose and at the intersection of waterline 0 and buttline 0. Waterline 0 is the section 91 inches [2311.4 mm] below the bottom of the constant section. Buttline 0 is the vertical center section of the aircraft. |

| | | |
|---|---|---|
| Axes definition | X | in centerline towards rear of aircraft |
| | Y | pointing horizontal out the right side of aircraft |
| | Z | pointing up as defined by right hand rule |
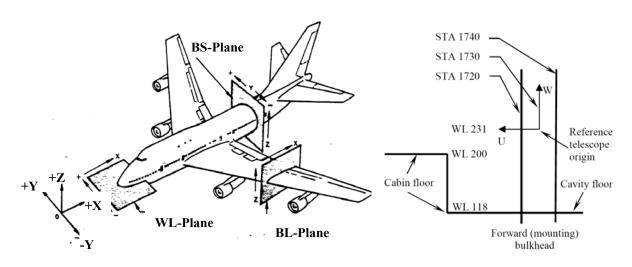


**Figure C.2.** Left side: Aircraft system reference frame with sample plane for waterline (WL), buttline (BL) and Bulkhead station (BS) plane [Kaluza 2001].
Right side: Side view of the aft cavity. Station numbers (STA) and WL numbers are shown for the forward bulkhead and the location of the reference telescope origin, the Aircraft Bulkhead Reference Frame (ABRF) [Machak 1992].

### C.3.2 Aircraft Bulkhead Reference Frame (ABRF)

| | |
|---|---|
| Origin | Center of bulkhead hole matching TA bearing center at STA 1730. It is 1730 inches [43942 mm] in X direction, 0 mm in the Y direction and 231 inches [5867.4 mm] in Z direction. |

| | | |
|---|---|---|
| Axes definition | U | negative X direction of ASRF, perpendicular to bulkhead plane towards cabin side |

| V | negative Y direction of ASRF, in bulkhead plane horizontal |
|---|---|
| W | positive Z direction of ASRF, in bulkhead plane towards Zenith |

## C.4 Celestial reference frames

### C.4.1 Equatorial Reference Frame (ERF)

The coordinates of an object on the sky is usually expressed in spherical coordinate equatorial reference frame is a spherical reference frame that

| Origin | Center of the Earth |
|---|---|

*Definition as spherical coordinate system*

| Reference plane | Celestial equator | |
|---|---|---|
| Reference direction | Vernal equinox | |
| Spherical coordinates | Latitude: | Declination ($\delta$ or DEC) |
| | Longitude: | Right ascension ($\alpha$ or RA) |

*Definition as Cartesian coordinate system*
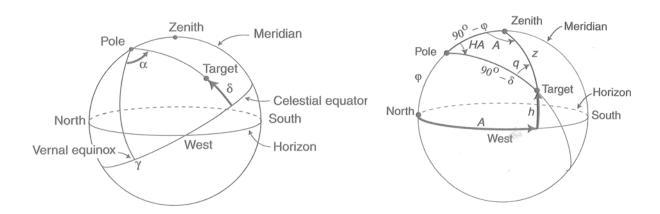
| Axes definition | X | Pointing toward the vernal equinox |
|---|---|---|
| | Y | In plane of celestial equator, perpendicular to X and Z, completes right-hand-rule |
| | Z | Pointing toward the North pole |



**Figure C.3.** Equatorial reference frame (on the left side) and Horizontal reference frame (on the right side) [Bely 2003].

### C.4.2  Horizontal Reference Frame (HRF)

Origin                                      Center of bearing

*Definition as spherical coordinate system*

Reference plane              Horizon

Reference direction          North

Spherical coordinates       Latitude:        Altitude (h)

                                       Longitude:      Azimuth (A)

*Definition as Cartesian coordinate system*

Axes definition                   X              Pointing toward the North in the horizon plane

                                          Y              perpendicular to X and Z, completes right-hand-rule, in the horizon plane

                                          Z              Pointing toward the zenith (local vertical)

With the observer's latitude *lat*, the Local Sidereal Time *LST* and the equatorial coordinates Right Ascension *RA* and Declination *DEC*, the horizontal coordinates are given by [Bely 2003]:

$$h = \arcsin\big(\cos(LST - RA)\cos(DEC)\cos(latitude) + \sin(DEC)\sin(latitude)\big) \tag{C.1}$$

For sin(*LST-RA*) < 0:

$$A = \arccos\left(\frac{\sin(DEC) - \sin(h)\sin(latitude)}{\cos(h)\cos(latitude)}\right) \tag{C.2}$$
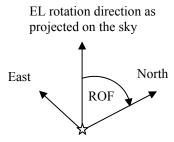
For sin(*LST-RA*) > 0:

$$A = 360° - \arccos\left(\frac{\sin(DEC) - \sin(h)\sin(latitude)}{\cos(h)\cos(latitude)}\right) \tag{C.3}$$

### C.4.3  Rotation of Field (ROF)

The horizontal and equatorial coordinates are spherical coordinates and describe the position of an object on a sphere. The parameter ROF is introduced to describe the orientation of a field at a certain position on the sky. At this position, ROF is defined as the angle between the projected TARF EL direction on the sky and the direction to celestial North. The sign convention for ROF is shown in Figure C.5. Once the telescope is inertially pointing, the ROF

will stay constant while LOS slowly changes as the celestial object moves across the night sky, until LOS has reached a limit.



**Figure C.5.** Sign convention for rotation of field (ROF), after [Webb 2004].

# D   Test run and observation details

**Table D.1.**   Listing of performed gyroscope alignment tests during the on sky test series in 2004.

| UTC date | Object | Exposure time [s] | Performed rotations | Aligned axes (*) | Description |
|---|---|---|---|---|---|
| 25.08.04 | Polaris | 1 | u, v, w | - | Initial measurement without any alignment. Evaluation yields alignment matrix #1. |
| 02.09.04 | Polaris | 0.5 | w | w | Measurement after implementing alignment matrix #1 which compensates w-axis misalignment. Simple evaluation shows worse alignment, wrong implementation of the matrix. Inverting of alignment matrix #1 produces matrix #2. |
| 02.09.04 | Star pair $\varepsilon = 47°$ | 0.5 / 5 | u, v, w | w | Measurement after implementing alignment matrix #2. Evaluation yields alignment matrix #3. |
| 08.09.04 | Polaris | 0.5 | w | w | Measurement after implementing alignment matrix #3 which compensates for residual w-axis misalignment. Evaluation yields alignment matrix #4. |
| 08.09.04 | Star pair $\varepsilon = 35.5°$ | 5 | u, v, w | u, v | Measurement after implementing alignment matrix #4 which compensates for u- and v- axes misalignment. Evaluation yields alignment matrix #5 |
| 09.09.04 | Polaris | 0.5 | w | - | Repeated measurement with implemented alignment matrix #4 |
| 09.09.04 | Polaris | 0.5 | u, v, w | w | Measurement after implementing alignment matrix #5 which compensates for residual w-axis misalignment. Final measurement of gyro alignment status |

*(*) This column indicates which gyro axes were corrected with respect to the previous measurements.*

**Table D.2.**   Alignment matrices that were implemented during the test runs.

---

UTC 09/02/2004 03:28:46

|  | 9.999962390016000e-01 | 0 | 2.742623317000000e-03 |
|---|---|---|---|
| $A_1 =$ | 1.563467213000000e-05 | 9.999837512947000e-01 | -5.700605410000000e-03 |
|  | -2.742578750000000e-03 | 5.700626854000000e-03 | 9.999799903574000e-01 |

UTC 09/02/2004 08:48:24

|  | 9.999962390016000e-01 | 1.563467214000000e-05 | -2.742623317000000e-03 |
|---|---|---|---|
| $A_2 =$ | 0 | 9.999837512947000e-01 | 5.700605410000000e-03 |
|  | 2.742578750000000e-03 | -5.700626854000000e-03 | 9.999799903574000e-01 |

UTC 09/08/2004 01:38:11

|  | 9.999937570982190e-01 | 1.962852696457961e-05 | -3.533465622955655e-03 |
|---|---|---|---|
| $A_3 =$ | -1.785047541327101e-06 | 9.999872494423987e-01 | 5.049784601438758e-03 |
|  | 3.533519689702028e-03 | -5.049746768725346e-03 | 9.999810066552546e-01 |

UTC 09/08/2004 06:09:11

|  | 9.998612667631196e-01 | 1.629757328616948e-02 | -3.440306247754789e-03 |
|---|---|---|---|
| $A_4 =$ | -1.627993672582380e-02 | 9.998544984895204e-01 | 5.093673557196793e-03 |
|  | 3.522820196108990e-03 | -5.036958926729290e-03 | 9.999811089004224e-01 |

UTC 09/09/2004 06:42:49

|  | 9.998608004680677e-01 | 1.629822920000000e-02 | -3.570264345000000e-03 |
|---|---|---|---|
| $A_5 =$ | -1.627989750000000e-02 | 9.998544423400000e-01 | 5.104808650000000e-03 |
|  | 3.652944007000000e-03 | -5.036958926730000e-03 | 9.999811089004200e-01 |

---

**Table D.3.** Azimuth, Altitude, refraction angle and angular distance of the observed stars derived from catalogue positions.

| # | Star identifier | Date | Time | Altitude | Azimuth | Angular distance | | Refraction angle | Refraction adjusted distance |
|---|---|---|---|---|---|---|---|---|---|
| | | [CDT] | | [deg] | [deg] | [deg] | [arcsec] | [arcsec] | [arcsec] |
| 1 | Eta Cep | 2.Sep.04 | 23:22:16 | 59.77 | 0.06 | 28.1 | 101252.8 | 31.8 | 101196.3 |
| | Polaris | 2.Sep.04 | 23:22:16 | 31.65 | 0.84 | | | 88.3 | |
| 2 | Polaris | 2.Sep.04 | 23:32:51 | 31.68 | 0.84 | 28.1 | 101252.8 | 88.2 | 101196.4 |
| | Eta Cep | 2.Sep.04 | 23:32:51 | 59.73 | 357.57 | | | 31.9 | |
| 3 | Eta Cep | 2.Sep.04 | 23:43:38 | 59.58 | 355.07 | 28.1 | 101252.8 | 32.1 | 101196.7 |
| | Polaris | 2.Sep.04 | 23:43:38 | 31.72 | 0.83 | | | 88.1 | |
| 4 | Polaris | 2.Sep.04 | 23:47:13 | 31.73 | 0.83 | 27.3 | 98186.7 | 88.0 | 98131.4 |
| | AlphaCep | 2.Sep.04 | 23:47:13 | 58.99 | 1.90 | | | 32.8 | |
| 5 | AlphaCep | 2.Sep.04 | 23:53:40 | 59.02 | 0.46 | 8.0 | 28929.7 | 32.8 | 28918.3 |
| | Beta Cep | 2.Sep.04 | 23:53:40 | 51.01 | 1.60 | | | 44.2 | |
| 6 | Beta Cep | 3.Sep.04 | 00:04:15 | 51.05 | 0.20 | 8.0 | 28929.7 | 44.1 | 28918.3 |
| | AlphaCep | 3.Sep.04 | 00:04:15 | 58.99 | 358.09 | | | 32.8 | |
| 7 | AlphaCep | 3.Sep.04 | 00:08:23 | 58.96 | 357.17 | 27.3 | 98186.7 | 32.9 | 98131.7 |
| | Polaris | 3.Sep.04 | 00:08:23 | 31.79 | 0.82 | | | 87.8 | |
| 8 | Polaris | 3.Sep.04 | 00:14:30 | 31.81 | 0.81 | 19.3 | 69377.0 | 87.8 | 69333.4 |
| | Beta Cep | 3.Sep.04 | 00:14:30 | 51.03 | 358.84 | | | 44.1 | |
| 9 | Beta Cep | 3.Sep.04 | 00:17:36 | 51.01 | 358.43 | 28.1 | 101191.7 | 44.2 | 101107.7 |
| | HIP47193 | 3.Sep.04 | 00:17:36 | 22.93 | 0.12 | | | 128.2 | |
| 10 | HIP47193 | 3.Sep.04 | 00:25:03 | 22.94 | 0.43 | 28.1 | 101191.7 | 128.1 | 101107.9 |
| | Beta Cep | 3.Sep.04 | 00:25:03 | 50.96 | 357.45 | | | 44.3 | |
| 11 | Beta Cep | 3.Sep.04 | 00:28:39 | 50.92 | 356.97 | 19.3 | 69377.0 | 44.3 | 69333.7 |
| | Polaris | 3.Sep.04 | 00:28:39 | 31.85 | 0.80 | | | 87.6 | |
| 12 | Polaris | 3.Sep.04 | 00:33:01 | 31.87 | 0.79 | 19.3 | 69377.0 | 87.6 | 69333.9 |
| | Beta Cep | 3.Sep.04 | 00:33:01 | 50.86 | 356.40 | | | 44.4 | |
| 13 | Beta Cep | 3.Sep.04 | 00:37:26 | 50.80 | 355.83 | 6.8 | 24469.1 | 44.5 | 24459.8 |
| | Xi Cep | 3.Sep.04 | 00:37:26 | 56.97 | 0.67 | | | 35.5 | |
| 14 | Xi Cep | 3.Sep.04 | 00:44:26 | 56.97 | 359.29 | 34.0 | 122402.4 | 35.5 | 122310.2 |
| | HIP47193 | 3.Sep.04 | 00:44:26 | 23.00 | 1.22 | | | 127.8 | |
| 15 | HIP47193 | 3.Sep.04 | 00:50:59 | 23.03 | 1.49 | 8.9 | 32069.4 | 127.6 | 32029.3 |
| | Polaris | 3.Sep.04 | 00:50:59 | 31.92 | 0.77 | | | 87.4 | |
| 16 | Polaris | 3.Sep.04 | 00:53:50 | 31.93 | 0.76 | 25.1 | 90334.9 | 87.4 | 90283.1 |
| | Xi Cep | 3.Sep.04 | 00:53:50 | 56.92 | 357.45 | | | 35.6 | |
| 17 | Xi Cep | 3.Sep.04 | 00:57:03 | 56.88 | 356.82 | | | 35.6 | |

**Table D.4.**  Specification of selected FPI centroid data sets after the command *MTBS_CENTROID*.

| Obs. No. | Object name | Start time of centroid data | End time of centroid data | Duration [sec] | Time to next MTBS_C [sec] |
|---|---|---|---|---|---|
| 1 | Eta Cep | 02.09.2004 23:22:16 | 02.09.2004 23:27:31 | 315 | 635 |
| 2 | Polaris | 02.09.2004 23:32:51 | 02.09.2004 23:38:01 | 310 | 647 |
| 3 | Eta Cep | 02.09.2004 23:43:38 | 02.09.2004 23:45:30 | 112 | 215 |
| 4 | Polaris | 02.09.2004 23:47:13 | 02.09.2004 23:49:10 | 117 | 387 |
| 5 | Alpha Cep | 02.09.2004 23:53:40 | 02.09.2004 23:55:52 | 132 | 635 |
| 6 | Beta Cep | 03.09.2004 00:04:15 | 03.09.2004 00:06:33 | 138 | 248 |
| 7 | Alpha Cep | 03.09.2004 00:08:23 | 03.09.2004 00:08:57 | 34 | 367 |
| 8 | Polaris | 03.09.2004 00:14:30 | 03.09.2004 00:16:08 | 98 | 186 |
| 9 | Beta Cep | 03.09.2004 00:17:36 | 03.09.2004 00:18:51 | 75 | 447 |
| 10 | HIP 47193 | 03.09.2004 00:25:03 | 03.09.2004 00:26:48 | 105 | 216 |
| 11 | Beta Cep | 03.09.2004 00:28:39 | 03.09.2004 00:30:13 | 94 | 262 |
| 12 | Polaris | 03.09.2004 00:33:01 | 03.09.2004 00:36:10 | 189 | 265 |
| 13 | Beta Cep | 03.09.2004 00:37:26 | 03.09.2004 00:38:53 | 87 | 420 |
| 14 | Xi Cep | 03.09.2004 00:44:26 | 03.09.2004 00:47:54 | 208 | 393 |
| 15 | HIP 47193 | 03.09.2004 00:50:59 | 03.09.2004 00:53:04 | 125 | 171 |
| 16 | Polaris | 03.09.2004 00:53:50 | 03.09.2004 00:55:01 | 71 | 193 |
| 17 | Xi Cep | 03.09.2004 00:57:03 | 03.09.2004 00:59:59 | 176 | |

**Table D.5.** Time between last centroid at star 1 and first centroid at star 2 and the appropriate pixel values.

| Move between Stars No. | Time between last centroid at star 1 and first centroid at star 2 | Column Pixel | Row Pixel | Column Pixel | Row Pixel |
|---|---|---|---|---|---|
| | [sec] | STAR 1 | | STAR 2 | |
| 2 – 3 | 71.0 | 510.20 | 546.20 | 437.20 | 588.40 |
| 3 – 4 | 51.0 | 512.50 | 546.40 | 530.70 | 552.70 |
| 6 – 7 | 38.0 | 515.17 | 546.99 | 491.66 | 579.39 |
| 8 – 9 | 48.0 | 514.79 | 543.67 | 548.76 | 534.78 |
| 10 – 11 | 49.0 | 516.61 | 548.25 | 554.25 | 545.70 |
| 11 – 12 | 36.0 | 515.17 | 543.96 | 677.62 | 596.14 |
| 13 – 14 | 38.0 | 514.34 | 549.96 | 566.83 | 556.86 |
| 15 – 16 | 32.0 | 514.47 | 544.97 | 566.21 | 570.48 |
| 16 – 17 | 67.0 | 513.93 | 542.31 | 473.55 | 566.62 |

**Table D.6.** Euler Angles and angular distances for the short moves as measured by the gyroscopes and corrected for the centroid displacement in the FPI field of view.

| Move between Obs. No. | EL | XEL | LOS | Spherical Sum EL and XEL |
|---|---|---|---|---|
| | [arcsec] | [arcsec] | [arcsec] | [arcsec] |
| 2 – 3 | 101150.7 | -4334.8 | 1151.0 | 101236.0 |
| 3 – 4 | -100679.4 | 11139.4 | 2702.1 | 101244.3 |
| 6 – 7 | 28825.7 | -2471.9 | 192.9 | 28930.8 |
| 8 – 9 | 69194.4 | -4919.8 | 886.3 | 69362.5 |
| 10 – 11 | 100920.2 | -7118.1 | 1856.1 | 101150.6 |
| 11 – 12 | -68879.3 | 8362.6 | 1347.2 | 69366.2 |
| 13 – 14 | 68528.7 | -10932.5 | 1883.8 | 69363.4 |
| 15 – 16 | 31984.7 | -1948.7 | 177.0 | 32043.5 |
| 16 – 17 | 90226.7 | -4217.9 | 1000.1 | 90318.8 |

# Bibliography

[Allan 1997]          D.W. Allan: *The Science of Timekeeping*, HP Application Note 1289, Hewlett-Packard, 1997

[Allen 2000]          C.W. Allen: *Astrophysical Quantities*, Fourth Edition, Springer-Verlag New York, 2000

[AlliedSignal 1998]   AlligedSignal: Product description, Redmond, WA, 1998

[Bayard 2004]         D. Bayard: Advances in precision pointing control for the NASA Spitzer space telescope. *Advances in the Astronautical Sciences*, **118**, AAS-04-71, pp. 527-545, 2004

[Becklin 2007]        E. Becklin; A. Tielens; R. Gehrz; H. Callis: Stratospheric Observatory for Infrared Astronomy (SOFIA). *Infrared Spaceborne Remote Sensing and Instrumentation XV*, M.Strojnik-Scholl, Proc. SPIE **6678**, pp. 66780A, 2007

[Bely 2003]           *The design and construction of large optical telescopes*, P.Y. Bely (ed.), Springer-Verlag, Heidelberg, 2003

[Berry 2005]          R. Berry, J. Burnell: *Handbook of Astronomical Image Processing*, 2nd edition, Willmann-Bell Inc., Richmond, VA, 2005

[Bittner 2002]        H. Bittner, M. Erdmann, J. Schmolke, K. Lattner, T. Levin, M. Erhard: SOFIA Tracking Subsystem: Results of Assembly, Operation and Calibration Tests, *Airborne Telescope Systems*, R. Melugin; H.-P. Röser (Eds.), Proc. SPIE **4857**, pp. 344-355, 2002

[Bremers 2005]        Personal communication with E.Bremers and A.Meyer, 13.04.2005

[Cartes du Ciel 2004] Sky Charts – Cartes du Ciel, P. Chevalley, Version 2.76, 2004

[Casey 2004]          S. Casey: The SOFIA Program: Astronomers return to the stratosphere, Advances in Space Research **34**, pp. 560–567, COSPAR, 2004

*Bibliography*


[Culshaw 2006]       B. Culshaw: The optical fibre Sagnac interferometer: an overview of its principles and applications, *Measurement Science and Technology*, **17** R1-R16, IOP 2006

[Davidson 2003]      J. Davidson: Building Blocks of TA Motion for Observing, Internal note, Rev. E, 2003

[Davenport 1988]     P.B. Davenport, G.L. Welter: Algorithm for in-flight gyroscope algorithm. Flight Mechanics/Estimation Theory Symposium, N89-15934 08-13, pp. 114-127, 1988

[Dunham 2002]        E.W. Dunham: Predicted SOFIA Image Size vs. Wavelength, Technical Note TN-EWD-005.R4, 2002

[Dunham 2004a]       E.W. Dunham, J.L.Elliot, T.A.Bida, B.W.Taylor: HIPO – A High-speed Imaging Photometer for Occultations, *Ground-based Instrumentation for Astronomy*, A. Moorwood, M. Iye (Eds.), Proc. SPIE **5492**, p. 592-603, 2004

[Dunham 2004b]       E.W. Dunham: HIPO-TA Coordinate Transformation, Internal note, 2004

[Dunham 2004c]       E.W. Dunham: Preliminary HIPO Results From Waco Ground Operations, Internal note, 2004

[Dunham 2008]        E.W. Dunham: HIPO-TA Coordinate Transformation, Internal note, 20.Nov.2008

[Erdmann 2001]       M. Erdmann: TA Optical Assembly Alignment and Verification Plan, SOF-PLA-KT-1000.0.01, Issue 6, 2001

[Erdmann 2002]       M. Erdmann: Image quality budget, SOF-LIS-KT-0000.0.01, Issue 8, 2002

[Erickson 2000]      E. Erickson, E. Dunham: Image Stability Requirement for the SOFIA Telescope, *Airborne Telescope Systems*, R. Melugin; H.-P. Röser (Eds.), Proc. SPIE **4014**, pp. 2-13, 2000

[Erickson 2005]      E. Erickson: The SOFIA Program, *The Dusty and Molecular Universe, A Prelude to Alma and Herschel*, ESA SP-577, 69, Paris, France, 2005

[Erhard 2000]        M. Erhard: Flange Assembly Description, SOF-SPE-KT-4000.0.02. Issue 3, 2000

[Erhard 2004]        M. Erhard: TA Optical Assembly Alignment during JAITV in Waco, SOF-TN-KT-054, Issue 3, 2004

[Faussot 1999]        N. Faussot: Test Report FOG180, 3454-SX-GF-01-001. Photonetics, Marly-Le-Roi, France, 1999

[Filippenko 1982]     A. Filippenko: The importance of atmospheric differential refraction in spectrophotometry, Astronomical Society of the Pacific **94**, pp.715-721, 1982

[Frank 2003]          J. Frank: SOFIA's Choice: Scheduling Observations for an Airborne Observatory, Proceedings of the 13th International Conference on Automated Planning and Scheduling (ICAPS), pp.226-235, 2003

[Gillessen 2004]      S. Gillessen: Sub-Bogenminuten-genaue Positionen von TeV-Quellen mit H.E.S.S., Ph.D. dissertation, Naturwissenschaftlich-Mathematische Gesamtfakultät, Ruprecht-Karls-Universität Heidelberg, 2004

[Haas 2005]           M.R. Haas: Optical Alignment and Image Quality Measurements and Tests during JAITV, SSMOC-TA-REP-1000-050602, 2005

[Harms 2005a]         F. Harms: Summary of the Gyro Alignment, SSMOC-TA-RP-5010.02-050722, Rev. 3, 2005

[Harms 2005b]         F. Harms: Differential Flexures between FPI and HIPO, SSMOC-TA-REP-5010.03-050719, Rev. 1, 2005

[Harms 2005c]         F. Harms: On sky absolute pointing measurements, SSMOC-TA-REP-5004-050722, Rev. 2, 2005

[Harms 2007a]         F. Harms: Test plan for gyroscope stability measurements, SOF-DSI-PLA-5211.0.01, Issue 2, 2007

[Harms 2007b]         F. Harms: Perfomance evaluation of integrated TA gyroscopes, Internal report, SOF-DSI-REP-5211.0-0001, Issue 2, 2007

[Hecht 2002]          E. Hecht: *Optics*, 4th edition, Addison Wesley, San Francisco, 2002

[Herdt 1998a]         B. Herdt: Imagers Description, SOF-SPE-KT-5100.0.04, Issue 2, 1998

[Herdt 1998b]         B. Herdt: Pointing Performance Analysis FPI/FA, SOF-TAN-KT-5100.0.02, Issue 1, 1998

[Howell 2000]         S. Howell: *Handbook of CCD Astronomy*, Cambridge University Press, Cambridge, UK, 2000

[IEEE 1998]           *IEEE Standard Specification Format Guide and Test Procedure for Single-Axis Interferometric Fiber Optic Gyros*, IEEE STD 952-1997, Inst. Of Electrical and Electronics Engineers, New York, 1998

[IRAF 1996]          IRAF project: Software manual of Image Reduction and Analysis
                     Facility (IRAF), National Optical Astronomy Observatories, Tucson,
                     USA, 1996

[Kärcher 2000a]      H.J. Kärcher: Airborne Environment – a Challenge for Telescope
                     Design, *Airborne Telescope Systems*, R. Melugin; H.-P. Röser (Eds.),
                     Proc. SPIE **4014**, pp. 278-284, 2000

[Kärcher 2000b]      H.J. Kärcher: Pointing Subsystem Description and Pointing Budget,
                     SOF-SPE-MG-5000.0.01, Issue 3, 2000

[Kaluza 2001]        T. Kaluza: SOFIA Coordinate Systems, Interface control document
                     global_05, 96145030-000, Raytheon for USRA, 2001

[Karttunen 2003]     H. Karttunen: *Fundamental Astronomy*, Springer-Verlag, Berlin, 2003

[Kovalevsky 2002]    J. Kovalevsky: *Modern Astronomy*, Springer-Verlag, Berlin, 2002

[Krabbe 1999]        A. Krabbe, H.-P. Röser: SOFIA Astronomy and Technology in the 21st
                     Century, *Reviews in Modern Astronomy*, R.E. Schielicke (Ed.), **12**,
                     Astronomische Gesellschaft, Hamburg, 1999

[Krabbe 2002]        A. Krabbe: Becoming reality: the SOFIA telescope, *Airborne
                     Telescope Systems*, R. Melugin; H.-P. Röser (Eds.), Proceedings SPIE
                     **4857**, pp. 62-72, 2002

[Lattner 2000]       K. Lattner: Tracker Subsystem Description, SOF-SPE-KT-5100.0.03,
                     Issue 4, 2000

[Levin 2002]         T. Levin: Test Report of Imager Tests at DLR, SOF-TRP-KT-
                     5100.0.04, Issue 1, 2002

[Levin 2008]         T. Levin: Specification of Centroiding Upgrade for Early Science,
                     SOF-SPE-KT-5310.0.03, Issue 1, 2008

[Lawrence 1999]      A. Lawrence: *Modern Inertial Technology*. Springer-Verlag, New
                     York, 1999

[Lefevre 1993]       H. Lefèvre: *The Fiber-Optic Gyroscope.* Artech House, Boston, MA,
                     1993

[Ly 2003a]           L. Ly: Test Report FOG180, 3454-SX-GF-01-002. Ixsea Oceano,
                     Marly-Le-Roi, France, 2003

[Ly 2003b]           L. Ly: Test Report FOG180, 3454-SX-GF-01-003. Ixsea Oceano,
                     Marly-Le-Roi, France, 2003

[Machak 1992]        D. Machak, *Guideline cavity envelope for aft configuration*, Systems engineering report, NASA-TM-110691, NASA Ames Research Center, Moffett Field, USA, 1992

[Massey 1992]        P. Massey, L. Davis: A User's Guide to Stellar CCD Photometry with IRAF, IRAF Manual, 1992

[MATLAB 2005]        The technical language of computing. Program documentation, The Mathworks, 2005

[Meyer 2003]         A.  Meyer: Star Availability for SOFIA Ramp Tests, SSMOC-SCOP-TN-0001-030724, Rev. 1, 2003

[Meyer 2005]         A. Meyer: TA Imager Alignment Evaluations, SSMOC-TA-REP-5010-050701, Rev. 1, 2005

[Moik 2000]          R. Moik: Servo System Design Description. SOF-SPE-MG-5200.0.01, Issue 5, 2000

[NASA SPO 2000]      SOFIA Telescope Assembly Requirements. Specification SOF-1011, Revision 7, 2000

[NCDC 2004]          Local Climatological Data, National Climatic Data Center, NOAA, www.ncdc.noaa.gov, 2004

[Ng 1993]            L. Ng: On The Application of Allan Variance Method for Ring Laser Gyro Performance Characterization. UCRL-ID-115695, Lawrence Livermore National Laboratory, 1993

[Ng 1996]            L. Ng: Characterization of Ring Laser Gyro Performance Using the Allan Variance Method. *J. Guidance,* Vol.20. No.1, Engineering Notes, 1996

[Perryman 1997]      M.A.C. Perryman et al.: The Hipparcos Catalogue, Astronomy and Astrophysics, **323**, L49-L52, 1997

[Robbins 2003]       J. Robbins: Telescope Assembly/Mission Contols and Communications Systems (MCCS) Functional Interface, SE03-047, Rev. A, 2003

[Rodloff 1999]       R. Rodloff: Physical Background and Technical Realization. *Optical Gyros and their Application*, RTO AG-339, NATO Research and Technology Organization, 1999

[Rousseau 2000]      J.-M. Rousseau: Non-linear curve fitting, ECAM, 2000

[Schmolke 2001a]     J. Schmolke: Detailed Algorithms for the TRC Software Design, Technical note, SOF-KT-TN-038, Issue 2, 2001

[Schmolke 2001b]     J. Schmolke: Tracker-TASCU Interface, SOF-ICD-KT-010, Issue 4, 2001

[Sedlak 2004]        J. Sedlak, J. Hashmall: Automated Sensor Calibration: Progress and Plans, AIAA 2004-4854, AIAA/AAS Astrodynamics Specialist Conference and Exhibit, 2004

[Seidel 2004]        C. Seidel: Optimierungsstrategien für faseroptische Rotationssensoren: Einfluss der spektralen Eigenschaften der Lichtquelle. Ph.D. dissertation, Fakultät für Elektrotechnik und Informationstechnik, Universität Fridericiana Karlsruhe, 2004

[Sergeant 2008a]     T. Sergeant: Test Report FOG180, 3454-SX-GF-01-001, Marly-Le-Roi, France, 2008

[Sergeant 2008b]     T. Sergeant: Test Report FOG180, 3454-SX-GF-01-002, Marly-Le-Roi, France, 2008

[Sergeant 2008c]     T. Sergeant: Test Report FOG180, 3454-SX-GF-01-003, Marly-Le-Roi, France, 2008

[SIMBAD 2001]        SIMBAD, Astronomical Database, CDS, Strasbourg, France, 2001

[Stone 1989]         R. Stone: A comparison of digital centroiding algorithms, Astronomical Journal **97** (4), pp. 1227-1237, 1989

[Stone 1996]         R. Stone: An Accurate Method for Computing Atmospheric Refraction, Astronomical Society of the Pacific **108**, pp.1051-1058, 1996

[Süß 2002]           M. Süß, K. Wandner, H.J. Kärcher, P. Eisenträger, U. Schönhoff: Airborne Pointing and Pointing Improvement Strategy for SOFIA, *Airborne Telescope Systems*, R. Melugin; H.-P. Röser (Eds.), Proc. SPIE **4857**, pp. 372-381, 2002

[Süß 2004a]          M. Süß: SOFIA: Implementation of quasistatic FBC, Technical note, 2004

[Süß 2004b]          M. Süß: SOFIA: Implementation of the imager displacement values, Technical note, 2004

[Sust 2002a]         E. Sust, U. Weis, E. Bremers, W. Schubbach: Manufacturing and integration of the SOFIA suspension assembly, *Airborne Telescope Systems*, R. Melugin; H.-P. Röser (Eds.), Proc. SPIE **4857**, pp. 300-311, 2002

[Sust 2002b]         E. Sust: SUA III Test Report, SOF-REP-MG-3300.0.02, Issue 3, 2002

[Titterton 2004]    D.H. Titterton, J.L. Weston: *Strapdown Inertial Navigation Technology.* 2$^{nd}$ ed., Progress in Astronautics and Aeronautics Series, Vol. **207**, AIAA, Reston, VA, 2004

[Titz 1998]    *SOFIA: Astronomie und Technologie im 21. Jahrhundert*, ed. R.Titz, H.-P-Röser, Berlin, 1998

[Vaseghi 1996]    S. Vaseghi: *Digital Signal Processing and Noise Reduction.* 2$^{nd}$ ed., Wiley & Sons, Chichester, UK, 2000

[Wandner 1999]    K. Wandner, T. Gaiffe, Y. Cottreau, N. Faussot, P. Simonpietri, H. Lefevre: Low Noise Fiber Optic Gyroscopes for the SOFIA Project. *Symposium Gyro Technology*, Stuttgart, Germany, 1999

[Wandner 2000]    K. Wandner, H.J. Kärcher: Pointing control system of SOFIA, *Airborne Telescope Systems*, R. Melugin; H.-P. Röser (Eds.), Proc. SPIE **4014**, pp. 360-369, 2000

[Webb 2004]    G.L. Webb, J. Davidson: Integrated SOFIA Command Language (SCL) User Manual, USRA-DAL-1172-01, Rev. B, 2004

[Weis 2000]    U. Weis, R. Sust, R. Kaindl, M. Erhard: TA Structure and Mechanics, SOFIA System CDR, 2000

[Wertz 1978]    J.R. Wertz: *Spacecraft Attitude Determination and Control*, Kluwer Academic Publishers, Dordrecht, Netherlands, 1978

[Wolf 2008]    J Wolf, H.-P. Röser, S. Tietz, M Wiedemann, E. Pfüller, D. Lilienthal: Improved Sensitivity of the SOFIA Target Acquisition and Tracking Cameras and a High Speed Diagnostic Camera for Telescope Movements in Flight, *Airborne Instruments,* I .S. McLean, M. M. Casali, 7014-36, 2008

[Zago 1998]    L. Zago, P. Genequand, J. Moerschell: Extremely compact secondary mirror unit for the SOFIA telescope capable of 6-degree-of-freedom alignment plus chopping, *Advanced Technology Optical/IR Telescopes*, Proc. SPIE **3352**, pp. 666-674, 1998

**List of Publications**

F. Harms, M. Auweter-Kurtz, G. Herdrich: Characterization of an inductively heated plasma source by variation of the operating frequency to simulate atmospheric reentry maneuvers, DGLR-2003-110, DGLR Deutscher Luft- und Raumfahrtkongress, October 2003, Munich, Germany

P. Waddell, M. R. Haas, E. W. Dunham, E. Bremers, F. Harms, P. J. Keas, K. Lattner, D. Lillienthal, A. W. Meyer, J. Wolf: SOFIA Telescope Functional Integration and Performance Test Activities, 205th Meeting of the American Astronomical Society, Vol. 36, No. 5, January 2005, San Diego, CA., USA

F. Harms, P. Waddell, M. Süß, H.-P. Röser: On sky testing and preliminary sensor alignment for the SOFIA telescope, Astronomical Telescopes and Instrumentation, Proceedings SPIE Vol. 6267, May 2006, Orlando, FL., USA

Jenniskens P., Kontinos D., Jordan D., Wright M., Olejniczak J., Raiche G., Wercinski P., Desai P.N., Taylor M.J., Stenbaek-Nielsen H.C., McHarg M.G., Abe S., Rairden R.L., Albers J., Winter M., Harms F., Wolf J., ReVelle D.O., Gural P., Dantowitz R., Rietmeijer F., Hladiuk D., Hildebrand A.R.: Preparing for the meteoric return of Stardust, Workshop on Dust in Planetary Systems, ESA SP-643 pp. 7-10, A.L. Graps (ed.), 2007

F. Harms, J. Wolf, G. Raiche, P. Jenniskens: CCD Imaging and slit less Spectroscopy of the Stardust Entry Radiation, 46th AIAA Aerospace Sciences Meeting and Exhibit, AIAA-2008-1214, January 2008, Reno, NV., USA

# Curriculum Vitae

| | |
|---|---|
| Name | Franziska Harms |
| Day of birth | October 8th, 1977 in Stuttgart, Germany |
| Nationality | German |
| Marital status | Not married |

| | |
|---|---|
| 10/2006-present | Research Engineer, Deutsches SOFIA Institut, Universität Stuttgart, Germany at NASA Ames Research Center, Moffett Field, CA, USA |
| 10/2003-present | PhD candidate, Institute of Space Systems, Universität Stuttgart, Germany, in cooperation with Universities Space Research Association (USRA) at NASA Ames Research Center, Moffett Field, CA, USA |
| 10/1996-10/2002 | Aerospace Engineering (Dipl.-Ing.), Universität Stuttgart, Germany Specializations: Space Systems, Flight Mechanics and Control |
| 04/2002-10/2002 | Diploma thesis at Institute of Space Systems, Universität Stuttgart, Germany: "Charakterisierung eines induktiv beheizten Plasma-generators zur Simulation von atmosphärischen Eintrittsmanövern von Raumflugkörpern unter Variation der Betriebsfrequenz" |
| 06/2001-12/2001 | Preliminary thesis at Department for Control & Simulation, TU Delft and Fokker Space (today: Dutch Space), Leiden, The Netherlands: „Modelling and Simulation of Formation Flying Satellites" |
| 10/1999-01/2001 | Research assistant, Institut für Raumfahrtsysteme, Universität Stuttgart |
| 11/1998-04/1999 | Internship at MAN Spatial Guyane, Kourou, French Guiana |
| 10/1997-09/1998 | Research assistant, Institut für Raumfahrtsysteme, Universität Stuttgart |
| 02/1997-04/1997 | Industrial internship at GEZE GmbH, Leonberg and Metallwerke Kamm GmbH, Renningen, Germany |
| 09/1996 | Internship at Daimler-Benz Aerospace AG, Munich, Germany |
| 1987-1996 | Eberhard-Ludwigs-Gymnasium in Stuttgart, German Abitur |

## Awards

| | |
|---|---|
| 2007-2009 | Invitation to participate as junior scientist at board member meetings of the Werner-von-Siemens-Ring foundation |
| 2007 | NASA Group Achievement Award for Airborne Observation of Stardust Entry |
| 2006 | NASA Engineering and Safety Center Group Achievement Award for Stardust Hypervelocity Observing Campaign Team |
| 2006 | Amelia Earhart Fellowship, ZONTA International |
| 2004, 2005 | Gottlieb Daimler-and Karl Benz-Foundation, Fellowship Program |
| 2003 | Award of the German Aerospace Association (DGLR e.V.) for the diploma thesis for junior scientists: ZARM-Award |